Dissertation
submitted to the
Combined Faculties for the Natural Sciences and for Mathematics
of the Ruperto-Carola University of Heidelberg, Germany
for the degree of
Doctor of Natural Sciences

presented by

M.Sc. Gustavo Quintas Glasner de Medeiros
born in: Rio de Janeiro, RJ, Brazil

Oral Examination: 16 of September 2016

Deep tissue light-sheet microscopy

Referees:

Dr. Stefano de Renzis

Prof. Dr. Michael Knop

Abstract

Light-sheet fluorescence microscopy, also recognised as selective plane illumination microscopy, or SPIM, has paved a new road towards imaging of entire specimens for long periods of time, *in vivo*. Nevertheless, as in any other microscopy technique, light-sheet fluorescence microscopy also heavily depends on the scattering and absorption properties of the imaged sample in order to generate 3D datasets with high signal to noise even at larger tissue depths. This thesis focuses on the development and implementation of new strategies and methods which target the minimization of scattering and absorption effects stemming from living specimens. Combined, the three methods provide the ability to perform gentle, high contrast deep tissue imaging and photomanipulation. Additionally, it allows easier handling and fusion of 3D multiview light-sheet images.

Zusammenfassung

Lichtblattmikroskopie, auch bekannt als Lichtscheibenfluoreszenzmikroskopie (SPIM) hat neue Möglichkeiten für die *in toto* Langzeitbeobachtung von lebenden Organismen eröffnet. Dennoch hängt die Lichtblattmikroskopie - wie alle Mikroskopiertechniken - stark von den Lichtstreuungs- und Absorptionseigenschaften des Präparates ab. Die vorliegende Arbeit widmet sich der Entwicklung und Umsetzung neuer Ansätze, die Streuung und Absorptionseffekte in Lebendpräparaten minimieren. Zusammen ermöglichen die drei hier beschriebenen Methoden eine sanfte, kontrastreiche Bildgebung und Photomanipulation bis tief ins Gewebe. Darüber hinaus erleichtern die hier entwickelten Techniken die Handhabung und die Verschmelzung von dreidimensionalen, aus mehreren Ansichten bestehenden Lichtscheibenfluoreszenzmikroskopiebildern.

ý

Contents

List of Figures

List of Tables

List of Abbreviations

2D	two dimensional
3D	three dimensional
AEL	after egg laying
Ca	calcium
CBB	cell biology and biophysics
CCD	charged-coupled device
cryo-EM	electron microscopy performed at cryogenic temperatures
Cy3	cyanine dye 3
Cy5	cyanine dye 5
dpf	days post fertilization
DSLM	digitally scanned light-sheet microscopy
eCSD	electronic confocal slit detection
EGFP	enhanced green fluorescent protein
EMBL	european molecular biology laboratory
EM	electron microscopy
FM7	balancer used in the X chromosome of *Drosophila*
FOV	field-of-view
GAP43	growth associated protein 43
GCaMP6s	protein used as a calcium indicator
GFP	green fluorescent protein
H2Av	histone protein
HO,HO1	heme oxygenase (1)
mCherry	monomeric Cherry fluorescent protein

mc	mitotic cycle
mIFP	monomeric infrared fluorescent protein
MuVi-SPIM	multiview selective plane illumination microscope
NA	numerical aperture
NPC	nuclear pore complex
NUP	nucleoporin
PET	polyethylene terepththalate
PMT	photomultiplier tube
PSF	point spread function
pu.1	transcription factor protein
RNA	ribonuclei acid
RFP	red fluorescent protein
sCMOS	scientifc complementary metal-oxide-semiconductor
sfGFP	superfolding green fluorescent protein
SPIM	selective plane illumination microscopy
tdiRFP	tandem infrared fluorescent protein
UV	ultraviolet spectrum
WFD	widefield detection

Introduction

Nature is all around us. It comprises from the yet unknown subparticles to the yet unknown farthest stars. It also comprises us. And yet, from all possible life on this planet, we have been the only species which has tried to understand nature's facets, to study it in detail, giving names to the physical laws we discovered, and discussing with ourselves about the missing links.

Since the very early ages, the observation and study of nature has depended mostly on our sight. What our eyes could not see was considered untrue, or even impossible until proven otherwise[1]. Soon we realized, however, that there is much more to the world than our naked eyes can see, motivating the creation and development of ever more complex devices which could aid our vision. From the first known single *Nimrud* lenses dating back to 700 BC to the Very Large Telescope and the Large Hadron Collider, philosophy and science has for more than 3000 years seeked to see the unseen.

The study of optics (from the ancient greek *optike*, meaning 'eye, vision' [2]), has also allowed us to look at ourselves and better understand how life works. The "artificial organs" used by Robert Hooke let him draw insects and plants [3] with unprecedented detail; in fact, the developments of improved optical microscopy apparatuses have made it the most popular tool in life sciences throughout the last century. Further on, the discovery and research of novel ways to illuminate and detect light from biological tissues permitted structures of interest to be better distinguished from their vicinity. In this aspect, the discovery of photoluminescence, in particular of fluorescence, combined with optical microscopy techniques, has created a new road towards medical and especially biological research.

[1] One famous example during the Inquisition period being Galileo Galilei's findings about the position of the Earth in our solar system, first published in his *"Dialogue concerning the two chief world systems, Ptolemaic and Copernican"*, in 1632, shortly afterwads being sent to Rome for trial [1].

This thesis is divided into four parts, with Chapter 1 devoted on bringing the current perspectives on the various challenges and methods in modern fluorescence microscopy for imaging of live specimens into the scene, with particular emphasis on light-sheet microscopy techniques and scattering and absorption effects in tissues. The other three chapters present three different projects which have a common goal: the minimization of scattering and absorption effects for performing deep tissue imaging and photomanipulation of live samples, with easier 3D data handling and processing. Although not all of the here presented results are strictly for multiview light-sheet microscopy, the entire work discussed in Chapters 2, 3 and 4 has been performed through implementation of the necessary modifications on our multiview light-sheet microscope - MuVi-SPIM [4].

In Chapter 2, we present a way to optimize detection of images in multiview light-sheet microscopes through utilization of electronic confocal slit detection. This is an important first step, since scattered light is always going to play a certain role in image acquisition, irrespective of the wavelength of light present for illumination or during fluorescence emission. We present the main gains in confocal multiview light-sheet microscopy, which go far beyond the image contrast improvement, and discuss its usability in biological systems where too strong scattering effects prevail.

Chapter 3 deals with presentation and discussion of preliminary work which lays ground towards *in vivo* and *in toto* imaging of embryonic development using infrared fluorophores. The development of a novel *Drosophila elanogaster* line which expresses a histone marker attached to a phytochrome-based fluorophore takes advantage of the fact that infrared emission allows live imaging at lower scattering levels, permitting light to penetrate deeper into the tissue with lower phototoxicity. With this fly line we were able to record the first long-term full embryonic development in the infrared spectral region. For a clear comparison, we present the new line along with two other fluorescence microscopy standards, and qualitatively discuss its caveats and benefits.

Finally, Chapter 4 presents the development and introduction of a new optical path into multiview light-sheet setups which allows laser-tissue manipulations with infrared femtosecond laser pulses. Apart from the presentation of hardware and software requirements, several examples will be motivated and given, providing part of the whole array of possible experiments which can be performed with the new system.

Chapter 1

Challenges in fluorescence microscopy of live specimens

Fluorescence microscopy has completely reinvented optical microscopy over the past decades. On the one hand, the introduction and continuous development of ever more precise labelling techniques, especially in the context of fluorescent proteins [5–9] for *in vivo* imaging has allowed the scientific community to learn more about the dynamics of very specific proteins through endogenous expression in many different model organisms. This alone already marked important steps towards the understanding of the natural mechanisms that make life alive. Along with the research and development of more flexible and yet powerful imaging techniques [10–12], fluorescence microscopy has anebaled the creation of entirely new research fields, from supperresolution microscopy to light-sheet based fluorescence microscopy, becoming the paragon of excellence in the life sciences and in biological research [13].

As life is about movement in 3D space, the ideal way to record living biology would probably be through the continuous generationg of movies of the whole specimen, in a way that all possible molecules can be clearly distinguished inside the entire volume and without harming the specimen's natural development. This is, however, obviously not possible, as nature itself tries to hide under the combination of various known photochemical effects. The diffractive nature of light, the efficiency and photostability of fluorescent markers and the sensitivity of live samples towards light and chemicals, along with their very opacity levels impose fluorescence microscopy to find new imaging strategies and adapt. As shown in Figure 1.1, so far the only solution has been to tune important imaging parameters such as imaging speeds,

spatial resolution, and photodamage levels to best cope with the biological sample.

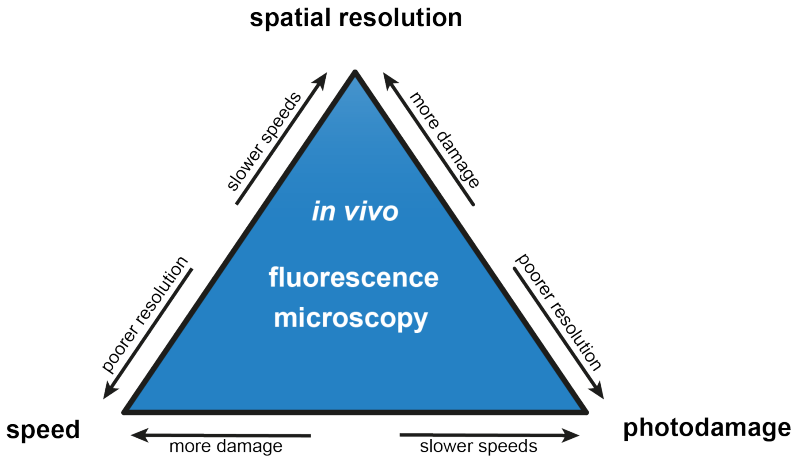

Figure 1.1: Trade-offs for *in vivo* fluorescence microscopy. The ideal microscopy: possibility to be perform fast imaging, with high spatial resolution and low photobleaching and phototoxicity. However, the combined effect of the diffractive nature of light, the efficiency and photostability of fluorescent markers and the very sensitivity of live samples towards high light intensities create strong constraints which imposes fluorescence microscopy techniques to adapt towards specific imaging needs. Adapted from talks by E. Betzig.

This first chapter is devoted to presenting and discussing some of the most important aspects of fluorescence microscopy. Its main focus lies on the main challenges faced by modern fluorescence imaging methods dedicated for live samples, with particular emphasis in light-sheet imaging and scattering of biological samples.

1.1 Fluorophores and labelling

First coined in 1852 by George Gabriel Stokes [14], the term fluorescence is known today as one form of *photoluminescence*, and is produced by certain chemicals called *fluorophores*. It relies on the effect of emitted optical radiation (light) during the relaxation of a molecule from an excited state (of higher energy) to its ground state of lower energy accompanied by the emission of a photon of a certain wavelength. The molecule can be excite e.g. through the absorption of a photon of typically shorter energy. The spectral difference between absorbed and emitted photons is denominated the Stokes shift, and is vital for fluorescence imaging: it allows the spectral discrimination between illumination and emission light, which can in practice be achieved through utilization of appropriate spectral filters during light detection. Very few molecules fluoresce naturally, reason why fluorescence microscopy, combined with specific labelling [15], allows the acquisition of signal coming from

specific proteins, cells or tissues. This is usually achieved either through introduction of fluorophores from an external source (staining), or through genetic enconding into the specimen's genome, being an important tool for *in vivo* imaging of biological dynamics as they happen in the most natural way.

When a fluorophore absorbs a photon, it takes up all of its energy E. The energy of a photon is directly proportional to its frequency ν and inversely proportional to its wavelength in vacuum (λ_0), and can be calculated through Planck's relation:

$$E = h \cdot \nu = \frac{h \cdot c_0}{\lambda_0}, \tag{1.1}$$

with h the Planck's constant and c_0 the speed of light in vacuum.

Depending on the amount of energy gained, the fluorophore will reach a specifc excited quantum state. If the energy is low, this is typically translated into higher molecular vibrational states. However, if the photon's energy is high enough to overcome the energy gap between the ground and the first excited electronic states, one of the fluorophore's electrons may receive enough kinetic energy to jump into the corresponding orbital. Such processes and their outcomes can be schematically drawn with the help of Jablonski diagrams[1], which can be represented as in Figure 1.2.

There are many ways through which the excited electron can distribute its energy. After photon absorption (a process which typically takes on the order of 10^{-15} seconds), the electron may jump from its ground state S_0 to a particular vibrational excited state, e.g. S_1^*. From there, one possible scenario is that through internal conversion or vibrational states the electron reaches the lowest excited level (S_1). If there is no spin-flip, the electron may lose energy in form of fluorescence thus producing a photon with longer wavelength), and further relax through to its ground state. Another possibility is that the electron suffers a radiationless transition to a triplet state T_1^*. As this process requires the electron to suffer a spin-flip, it is less probable to occur. Still, from the lowest triplet level the electron leave the dark state through photon emission in a process called *phosphorescence*, a process which can take from µs to seconds. This is because during the time that the electron is in the triplet state, it can still absorb another photon, moving it to higher vibrational triplet states, and further delaying its radiative relaxation into the electronic ground singlet state. In practice, this means that the electron in the triplet state will miss

[1] The first work showing such a quantum level scheme was published by A. Jablonski in 1935 [16], focusing "On the mechanisms of photoluminescence from phsphorous dyes".

many fluorescence cycles until emitting a photon. Depending on the microscope setup used, this waiting time might be too long, and the phosphorescent photon will never be detected.

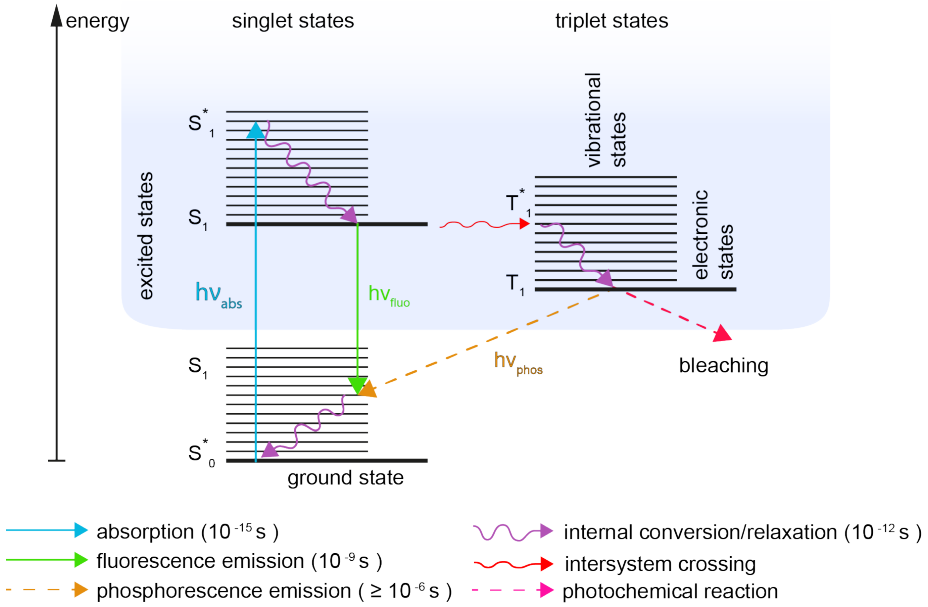

Figure 1.2: The Jablonski diagram. There are many ways which the excited electron can distribute its energy. After photon absorption (a process which typically takes on the order of 10^{-15} seconds), the electron may jump from its ground state S_0 to a particular vibrational excited state, e.g. S_1^*. From there, one possible scenario is that through internal conversion or vibrational states the electron reaches the lowest excited level (S_1). If there is no spin-flip, the electron may lose energy in form of fluorescence thus producing a photon with longer wavelength), and further relax through to its ground state. Another possibility is that the electron suffers a radiationless transition to a triplet state T_1^*. As this process requires the electron to suffer a spin-flip, it is less probable to occur. Still, from the lowest triplet level the electron leave the dark state through photon emission in a process called *phosphorescence*, a process which can take from µs to seconds. This is because during the time that the electron is in the triplet state, it can still absorb another photon, moving it to higher vibrational triplet states, and further delaying its radiative relaxation into the electronic ground singlet state. In practice, this means that the electron in the triplet state will miss many fluorescence cycles until emitting a photon. Depending on the microscope setup used, this waiting time might be too long, and the phosphorescent photon will never be detected.

Yet another possibility is that the electron, while locked on the triplet state, allows the molecule to interact chemically with others generating unnatural processes which can be toxic to the living sample (this is therefore called induced phototoxicity). It can also damage the fluorophore irreversibly in a process termed *photobleaching*, which is one of the biggest concerns when new fluorophores are being developed. Normally fluorophores with high photostability suffer less from photobleaching effects.

The Jablonski diagram can also visually present the nature of the Stokes shift: since non-radiative energy transfer occurs through relaxation via vibrational states or internal conversion, the emitted photon has to have less energy (i.e. longer wavelengths) than the absorbed photon. Radiative emission

through fluorescence is favoured if the energy gap between the electronic ground and excited states is wide enough to offer little probability that the electron further relaxes through non-radiate internal conversion processes. This could occur if for instance there would be a certain degree of overlap between higher vibrational states from S_0^* and S_1, and is particularly important since internal conversion can take place at much faster rates than fluorescence emission (around a 1000 times faster). Thus, fluorescence is most probably for molecules with large separation between energy bands.[2]

There are many different types of fluorescent probes today including photoswitchable proteins, quantum dots, synthetic dyes and fluorescent proteins. In fact, the so far most complete compendium on fluorescent probes provides information on more than 3000 different fluorophores which aim at answering a wide range of biological questions [17]. Most of these can however be categorized as either synthetic dyes or fluorescent proteins.

1.1.1 Synthetic fluorescent dyes

Fluorescent dyes are synthetic fluorophores which need to be provided to the biological sample exogenously. They have been in use for more than a century, with the first ever synthetic dye, the aniline purple or mauve, being discovered by accident in 1856 by William Henry Perkin [18]. Another example is methylene blue, which has been first discovered in 1891 and used in the treatment of malaria, as in this period it was believed that drugs and dyes work similarly, through preferentially staining pathogens and harming them [19]. Since then, methylene blue has found numerous other applications. For example, in biology it is widely used in the staining of the hybridization probes used in northern blotting. Northern blotting is an experimental procedure in which a voltage difference is applied to a gel containing pockets filled with RNA samples. Since RNA is negatively charged, the different strands get distributed by size due to their different retardation forces (such as friction). the size distribution of the RNA of interest can be observed through the labelling and addition of a hybridization probe into the gel, i.e. another RNA strand which has a complementary sequence to the RNA of interest [20]. Methylene blue is also used in medicince for staining various different tissues during surgery, endoscopy, and in the recognition of blood cells in histological sec-

[2] However, another non-radiative relaxation process can happen if the excited molecule collides with another one, transferring its electron energy non-radiatively. This process is called *quenching*, and is naturally reversible, unlike photobleaching.

tions. Other well-known dyes are fluorescein (with emission in the green) [21], eosin Y (yellow) and eosin B (blue) [22].

Synthetic dyes are also widely used for performing antibody staining in cells and tissues (also known as immunostaining). When mammals are injected with a protein of interest, their immune system responds by producing the necessary antibodies against it. By isolating the antibodies and fusing them with synthetic dyes it is possible then to label the protein of interest in other biological systems. This work was first introduced in 1940 [23], and in 1984 the Nobel Prize in Medicine was awarded to Georges Köhler, César Milstein and Niels Kaj Jerne for their contribution to the development of monoclonal antibodies [24].

New fluorescent dyes with higher quantum yield have been developed in the last years, aiming at providing brighter signal in a variety of colors (e.g. the cyanine dyes Cy3-Cy5 and the Alexa Fluor family). Still, one of the main drawbacks is the inability to have them produced endogenously by living cells and organisms. This is where fluorescent proteins show their potential.

1.1.2 Fluorescent proteins

Fluorescent proteins can be found in nature, and are responsible for the wonderful color palette of fluorescent marine organisms such as the anemone hermit crab, sea turtles, eels, sharks, and are also found in ants and wasps.[3] The first ever isolation of a blue-light-bioluminescent, calcium-induced protein took place in 1961 [25], during studies with the jellyfish *Aequorea victorea*: the protein was then called *aequorin*. However, during the isolation procedure, a bi-product was found: this was another protein which produced bright green fluorescence under the excitation of ultraviolet light. At that time no real attention to it was given, and it was called *green fluorescent protein* (GFP). Many years passed until GFP was first purified, cloned and first utilized as a fluorescent marker [5, 8, 9], opening a new era on molecular probes for microscopy. Since then, the green fluorescent protein has been engineered into mutants of different emission spectra and different folding proterties [26–28], ultimately leading the Nobel Prize for chemistry in 2008 to Osamu Shimomura, Martin Chalfie and Roger Y. Tsien "for discovery and development of the green fluorescent protein, GFP." [29]. Furthermore, the discovery and isolation of new fluorescent proteins from other species (such as from marine species of the

[3] For the interested reader, there are beautiful example images of fluorescent marine life which can be found in the expeditions from David Gruber, from National Geographic.

genus *Discosoma* (corals), and bacteria of the genus *Deinococcus*) have further expanded the color palette, also opening new approaches towards multicolor imaging [6, 7, 30–32]. Figure 1.3 depicts excitation and emission spectra of a few widely used fluorescent proteins for labelling.

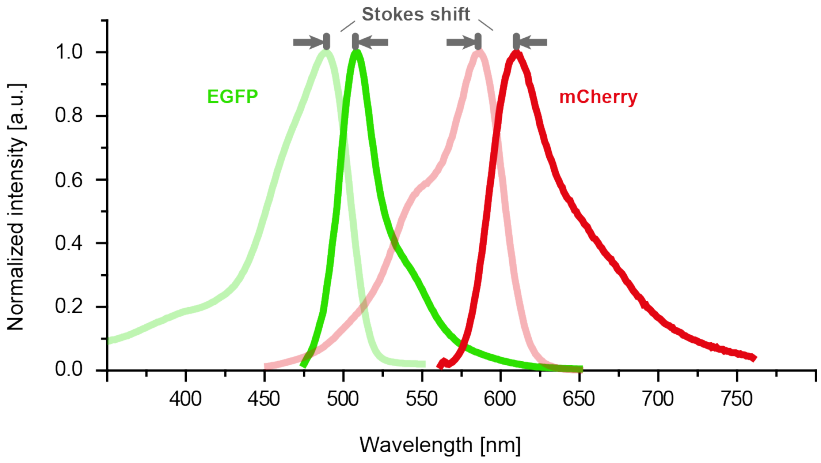

Figure 1.3: Excitation and emission spectra of EGFP and mCherry. Normalized curves for excitation and emission spectra of EGFP and monomeric Cherry (mCherry) are shown in color code. The corresponding Stokes shift for EGFP and mCherry lies at 19 nm and 13 nm, respectively, and the spectral distance distnce is of around 100 nm, making these two fluorescent proteins optimal for dual color imaging. Data from [33].

Maybe one of the most important properties of fluorescent proteins is their ability to have their corresponding cloned genomic sequence, along with the sequence of the selected protein of interest, inserted into the genome of a living animal. With this, the selected protein, along with its fluorescent label, can be endogenously produced, providing information on the protein's dynamics, production rates, spatial and temporal localization, and more. This has paved a new road towards *in vivo* imaging, allowing the observation of cell division, morphogenesis, etc, revealing nature's machinery with much improved contrast and selectability.

New fluorescent proteins which emit fluorescence in the infrared region have accelerated the pursuit towards deep tissue single photon imaging of live samples, as scattering is reduced towards longer wavelengths (*cf*. Section 1.5.2). Although promising, most of these fluorophores display very long maturation rates and low photostability, which limit their labelling kinetics and long-term imaging capabilities [7, 34]. This topic will be further covered in Chapter 3.

1.2 Widefield fluorescence microscopy

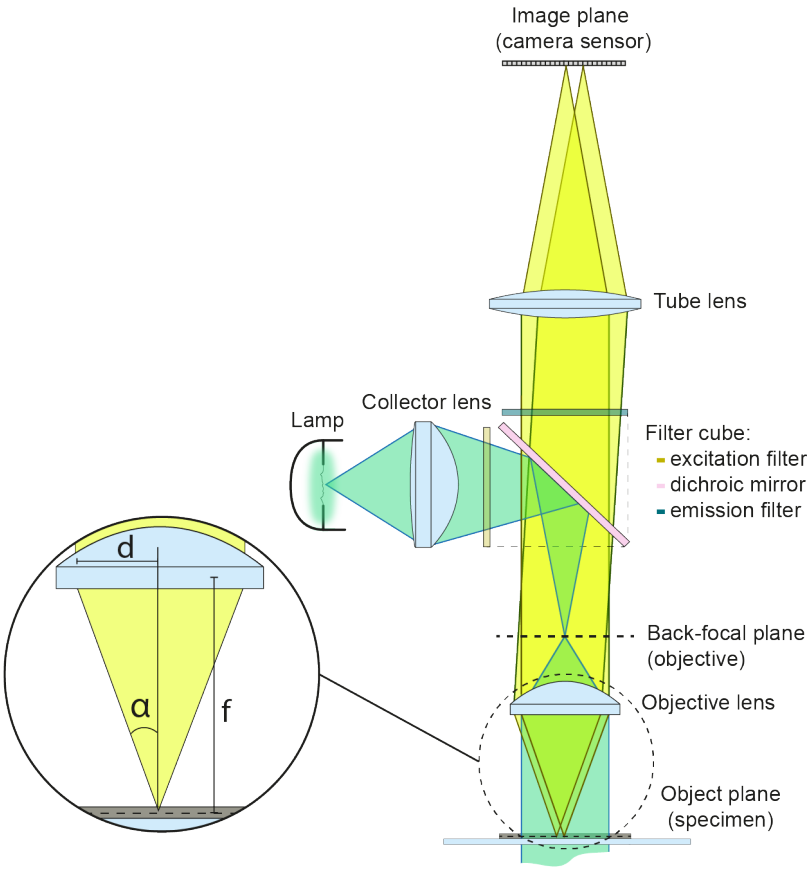

Figure 1.4: The widefield epifluorescence microscope. In a widefield epifluorescence microscope, light from a lamp is collected by a collector lens, spectrally shaped by an excitation filter, relfected by a dichoir filter focused at the back focal plane of the objective lens, further illuminating the entire object plane (and the specimen) at once. Fluorescence is collected by the objective lens, spectrally shaped by the dichroic and emission filters, and further focused onto a camera sensor through a tube lens.

The *widefield microscope*, equipped with spectral filters for excitation and emission light, is the simplest fluorescence microscope. When it uses the same objective for illumination and detection of fluorescence, it can also be referred to as an *epifluorescence* microscope. The schematics of such a microscope setup are shown in Figure 1.4. A specimen labelled with fluorophores is placed below the objective, usually on top of a coverslip. Wavelengths for illumination and detection are selected through a *filter cube*, which houses the excitation and emission filters, as well as a dichroic filter. The latter is used in such a way that its transition wavelength reflects most of the excitation wavlelengths, while allowing most of the emission wavelengths to pass through. Light is generally produced by a lamp (e.g. a mercury lamp), and part of it is focused

with the help of a collector lens through the filter cube to the back focal plane of the objective. After the objective, parallel rays illuminate a large area of the specimen at once. Part of the isotropically emitted fluorescence signal is then collected by the same objective lens, and focused onto a camera sensor through the filter cube with a tube lens.

Since photons are emitted in all directions, only the ones within a certain angle range will be able to be redirected by the objective lens on the detection path and onto the camera sensor; photons with higher angles will be lost. This opening angle is therefore an important optical property of the system, and together with the refractive index n of the objective's immersion medium, defines the objective's *numerical aperture* (note that we consider only half of the total opening angle).

$$NA = n \cdot \sin \alpha. \tag{1.2}$$

For very small values of α, $\sin \alpha \approx \tan \alpha$ and the numerical aperture can be crudely approximated by the ratio between the objective lens's radius and its focal length:

$$NA \approx n \frac{d}{f}, \quad \text{when} \quad \alpha \ll 1. \tag{1.3}$$

The overall magnification M of the widefield detection is equal to the ratio of the focal lengths of the tube lens over the objective lens. This is an important measure for knowing the size of the maximum area that the camera sensor can detect: it is simply the size of the camera sensor divided by the magnification. Considering the area of the sensor to be A:

$$FOV = \frac{A}{M}. \tag{1.4}$$

In widefield microscopy the entire detectable field-of-view (FOV) is illuminated at once, which means that this technique can generate images at high speeds. If the sample is moved up or down in a stepwise fashion, with each step leading to the specimen's exposure to light and the acquisition of an image, a 3D stack of images can be acquired.

1.2.1 Diffractive nature of light

Before we continue, it is necessary to discuss an important aspect about light, which generates spatial constraints in optical imaging. Let us consider that a point source (e.g. an infinitesimally small single emitting fluorophore) is emitting light in all directions, and we would like to produce an image of this

single emitter utilizing a lens. The lens cannot collect light from all directions, as it is finite in size. Therefore, only part of the emitted light can be redirected through refraction, while at the circular aperture of the lens, light diffracts, forming a particular 3D intensity function, called the *point spread function* [35]. Neglecting the effects of polarization, the scalar theory of diffraction defines the intensity PSF as:

$$H(u,v) = C_0 \left| \int_0^1 J_0(vr) e^{i \cdot ur^2} r dr \right|^2 . \tag{1.5}$$

with C_0 a normalization constant and J_0 the zero order Bessel function of the first kind. u and v are called *optical coordinates* and are normalized variables which relate to the spatial coordinates through [36]:

$$v = \frac{2\pi n \Delta r}{\lambda_0} \sin\alpha, \quad u = \frac{8\pi n \Delta z}{\lambda_0} \sin^2 \frac{\alpha}{2}. \tag{1.6}$$

Here we used $r = \sqrt{x^2 + y^2}$ as *lateral coordiantes* and z as the *optical axis*. n denotes the refractive index, λ is the wavelength of light and α is half of the opening angles as defined in Equation 1.2.

The PSF can also be interpreted as the probability density that a photon originating from a certain point P arrives with coordiantes (u, v) near a certain point Q. Since image formation is space invariant (meaning that object and image plane can be interchanged), $H(u, v)$ can be seen as the probability that a photon emitted at a point near Q reaches a point P. For this case, the focal plane is where $u = 0$, leading to:

$$H(0,v) = C_0 \left| \int_0^1 J_0(vr) r dr \right|^2 = \left[2 \frac{J_1(v)}{v} \right]^2 , \tag{1.7}$$

with J_1 the first order Bessel function of the first kind. $H(0, v)$ is a two-dimensional lateral distribution which features a maximum peak at the center and concentric rings of maxima and minima. It is famously known as the *Airy pattern*. The first minimum lies when $v = 3.83$, yielding the radius of the central disk, also called the *Airy disk*. Plugging it into Equation 1.6:

$$\delta_{xy} = \frac{3.83}{2\pi} \frac{\lambda_0}{n \cdot \sin\alpha} \approx 0.61 \frac{\lambda_0}{NA} \tag{1.8}$$

Analogously, considering $v = 0$ allows us to calculate the distribution along the optical axis:

$$H(u,0) = C_0 \left[\frac{\sin \frac{u}{4}}{\frac{u}{4}} \right]^2 . \tag{1.9}$$

Also here the distribution function displays maxima and minima, with the first minimum at $u = 4\pi$, yielding:

$$\delta_z = \frac{2n\lambda_0}{NA^2}. \tag{1.10}$$

If we consider now the effect of multiple point sources, the final image obtained is the combined effect of the total intensity distribution with the actual fluorophore distribution which make the object. In mathematical terms this can be translated to a *convolution* operation between the object O and the PSF function H, yielding an image I:

$$I(u, v) = O(u, v) \star H(u, v). \tag{1.11}$$

The results here presented show that the intensity distribution of an infinitesimal point emitter is spatially limited by the diffractive nature of light itself. In a way, the PSF acts on the image formation of a distribution of point sources the same way that a large painter's brush affects the painting of much finer strokes: the brush imposes a spatial limit to the image, just as diffraction does any imaging system. Furthermore, together with Equations 1.8 and 1.10, it is possible to relate the spatial dimensions of the Airy disk with physical quantities such as the wavelength of light, the refractive index and half of the maximum opening angle of the optical system. With this in mind, it is possible to define the minimum size of features which can be distinguished in traditional optical microscopy, i.e. the resolving power of the microscope.

1.2.2 Resolution and optical sectioning in widefield microscopy

The *resolving power*, or optical *resolution* of a microscope setup is a measure of the shortest distance between two adjacent points with which they can still be resolved, i.e. detected as separate entities by the microscope. They cannot be infinitesimally close, since the overlapping Airy functions will come so close that both maxima become indistinguishable. The definition proposed by Lord Rayleigh in 1902 states that two emitters can be discerned in the image space if the minimum distance between them corresponds to when the maximum intensity of one falls into the first minimum of the second [37], which corresponds to Equations 1.10 and 1.8. In this definition, the values of δ_{xy} and δ_z provide the resolving power in all three dimensions. However, it has been noted that this definition only holds for fairly small numerical apertures, deviating towards higher values for high NA lenses. A way to correct for this is through redefinition of the two variables [38]:

$$\delta_{xy} = \frac{\lambda_0}{n\sqrt{3 - 2\cos\alpha - \cos 2\alpha}} \tag{1.12}$$

$$\delta_z = \frac{\lambda_0}{n(1 - \cos\alpha)}. \tag{1.13}$$

Typically in any optical system, light originating from outside the focal plane (depicted in Figure 1.4 as the object plane) either contributes to image background or produces a blurred artifact which lowers the ability to distinguish features in the focal plane. This is also due to the fact that light inside tissues typically scatters, an effect which adds up with tissue length (more on scattering is discussed in Sections 1.5.3, 1.5 and in Chapter 2). In the epifluorescent widefield microscope, however, illumination does not discriminate the focal plane from the rest of the sample, as it is performed with a quasi parallel beam of light, thus illuminating the whole volume it encompasses. This means that fluorohores within a large volume of the sample can be excited and fluoresce, including in out-of-focus areas. Since all the light detected by the PSF of the objective lens will contribute to the formation of the image, out-of-focus signal will lead to loss of contrast and increase in noise levels, decreasing the overall image contrast [39].

The effect of loss of image quality due to out-of-focus light detection mentioned above is mainly due to the microscope's poor *optical sectioning* capabilities, i.e. the ability of a microscope to single out features in the focal volume and filter out the background signal [40]. The optical sectioning capabilities of a microscope can be improved through e.g. the implementation of extra parts which can effectively block out-of-focus and scattered light, as in the case of confocal microscopes. Other approaches utilize decoupled illumination and detection directions in order to make better usage of illumination light, illuminating fluorophores only in a thin volume around the focal plane: this is the trick behind light-sheet fluorescence microscopy.

1.3 Confocal fluorescence microscopy

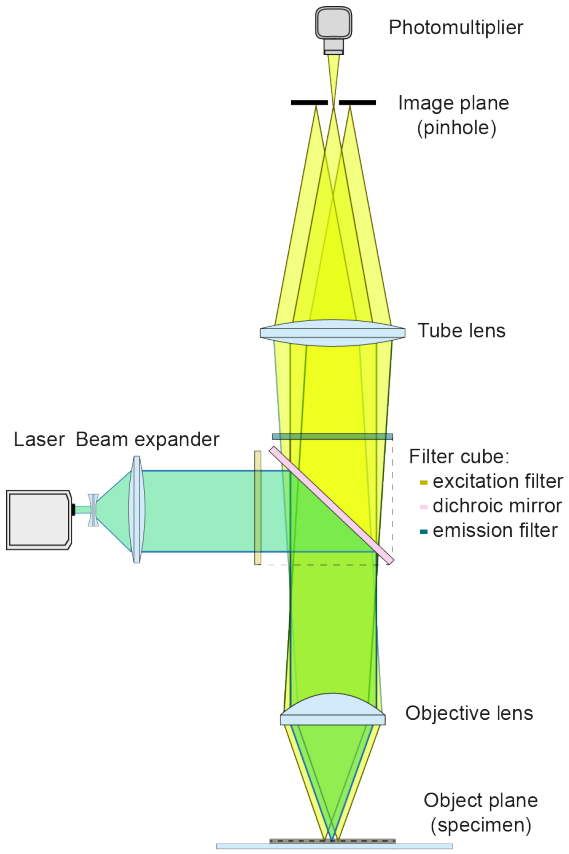

Figure 1.5: The confocal epifluorescence microscope. In a confocal epifluorescence microscope, light from a laser source is expanded and redirected to the objective lens through a dichroic filter. The objective focuses the illumination beam in a very small volume inside the specimen, in the object plane. The creation of an image is done either through movement of the specimen laterally with the help of motorized stages, or with the aid of motorized mirrors which scan the focused illumination beam throughout the FOV. The introduction of a physical pinhole on the image plane of the detection path hinders the acquisition of signal from out-of-focus and scattered light, allowing only in-focus light to be detected by the photomultiplier tube.

The main idea behind the *confocal microscope* is the discrimination of out-of-focus light through the utilization of a physical pinhole, located at the image plane of the detection path. The first publication dates back to 1961 with the filed patent from Marvin Minsky [10]. Now, it has become the main microscopy technique used in biology [41]. The main parts which compose a confocal microscope in its simplest form (also as described in the patent) are presented in Figure 1.5. Illumination light is typically from a laser source with fixed wavelength λ_0 (widefield microscopes with laser excitation also do exist). The laser beam is first expanded before being reflected by the dichroic

filter and redirected to the objective lens. This time, the objective lens focuses the laser beam into a small volume, which can be calculated by Equations 1.10 and 1.8, and depends on the numerical aperture of the objective: typically the laser beam is expanded in order to fully cover the back aperture of the objective, and thus the full NA is used for focusing. Unlike with the widefield microscope, however, only detected light situated at a conjugate focal volume to the location of the illumination PSF is going to be detected, as a physical pinhole located at the image plane of the detection path prevents any out-of-focus light to be detected by a photomultiplier tube (PMT). The full image can be constructed by moving the specimen with a motorized xy-stage, of by translating the illumination beam through the field of view: this requires a 2D set of motorized mirrors which can change the angle of the illumination beam at the back-focal plane of the objective (not shown in the figure).

This system is very effective in minimizing scattered and out-of-focus light detection, and improves image contrast as well as resolution. In fact, the probability that emitted fluorescence is detected at a certain point in space is dependent not only on the probability that a fluorophore is excited at this location, but also on the probability that the emitted photon will be detected by the PMT. This in turn means that the effective PSF of the system H_{eff} is the product from the illumination and the detection PSF, H_{ill}, H_{det}, respectively:

$$H_{eff} = H_{ill} \cdot H_{det}. \tag{1.14}$$

Furthermore, assuming that the Stokes shift between excitation and emission wavelengths is small (less than 10% of the detection wavelength) and that the lateral and axial PSF profiles can be approximated by Gaussian functions, and using Equations 1.12 and 1.13, it is possible to calculate the increase in resolution of a confocal microscope to be of 0.71 [42].

The increase in resolution and image contrast comes nonetheless at a price: the raster-scan of the focal spot throughout the entire FOV takes time, as it needs to compromise between illumination light dosage and enough detected photons for good image quality. In general, the illumination focused beam typically spends a µs in each position of the image. Considering each image to need 1024x1024=1048576 positions for acquisition, this would mean that roughly one second is needed in total. This clearly scales with the amount of plnes needed for creating a stack of images, and in the case of say 50 planes, almost an entire minute needs to be spent until a new acquisition can take place for the following timepoint. Moreover, even though the out-of-focus and highly scattered emitted photons are not detected, each illumination position

still excites fluorophores residing above and below the focal plane within the vicinity of the focal volume: this can lead to phototoxic effects in the specimen, especially considering the long exposure times needed for an entire stack. In order to address some of these concerns faster illumination and detection with spinning disks allow the excitation and detection through multiple pinholes. Nonetheless, this increases the total out-of-focus light detection, thus bringing down contrast and resolution.

1.4 Light sheet based fluorescence microscopy

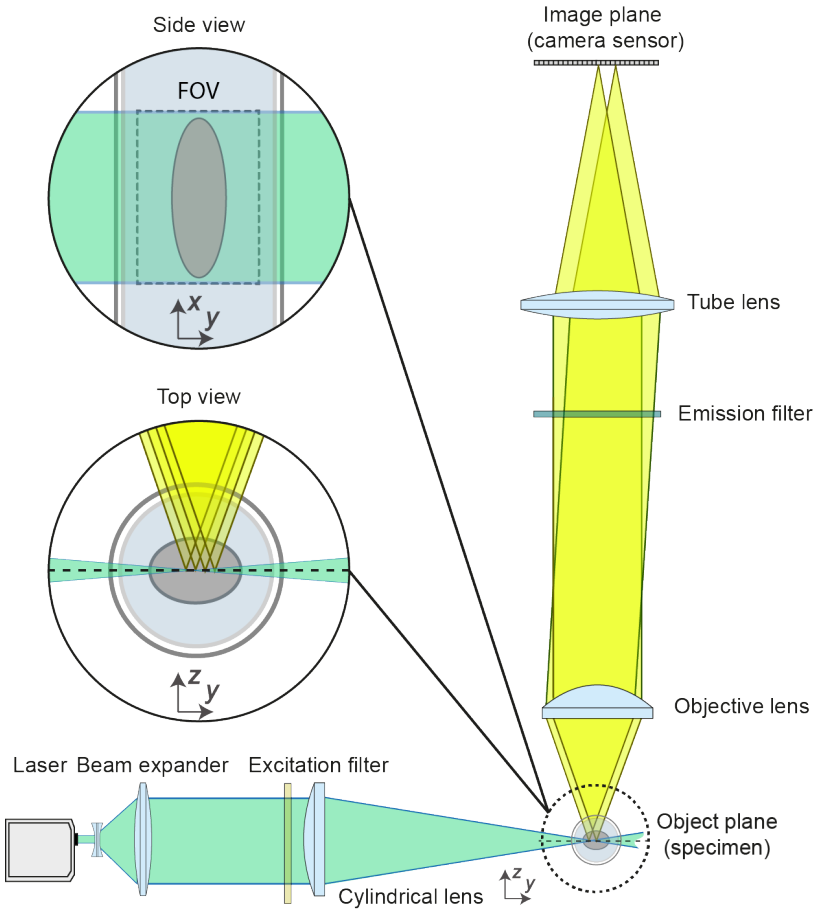

Figure 1.6: The light-sheet based fluorescence microsope. Schematics of a typical light-sheet fluorescence microscope design. Two objectives for illumination of the sample and fluorescence detection are orthogonally placed to each other, with the sample located at the focal plane of the detection objective. the sample is usually embedded in a gel, and is able to freely move in space with the help of motorized stages, not shown here for simplicity. Light is generated by a laser source, expanded and directed to a cylindrical lens, which shapes the illumination light in order to create a sheet of light, which is further directed by the illumination objective for optical section of the sample. As the whole FOV is illuminated, emitted fluorescent signal is collected by the detection objective, and acquired by the camera through usual widefield detection optics. The two inserts on the left depict the region marked with a dashed ring, seen through two directions. The sample is shown as a gray ellipsoid, and can be embedded in a cylindrical gel.

Differently from epifluorescent microscopes, the main idea behind light sheet fluorescence microscopy is to generate a thin optical sectioning by illuminating the sample from the side. In general, this requires two objective lenses which are placed at a right angle from each other, one being used for illumination and the other for detecting fluorescence. A laser source is ultimately focused through the illumination objective onto the sample in such a way that a thin sheet of light is created and sections the sample from the side. The light-sheet lies orthogonal to the detection axis, and overlaps with the focal plane of the detection objective lens, which is then able to collect fluorescence emitted mainly from within the thin part of the sample illuminated by the illumination plane. Detection follows according a usual widefield detection approach, with a detection objective, an emission filter, a tube lens and a camera sensor, usually a charged-coupled device or a scientific complementary metal-oxide-semiconductor (CCD or sCMOS, respectively). The specimen is usually embedded in a gel, and attached to a set of motorized stages which allow the sample to be moved in all directions. A stack of images is typically acquired with the movement of the sample in a stepwise fashion through the illumination plane. Representative schematics following some of the first light-sheet microscope designs are shown in Figure 1.6, with the two inserts depicting the lateral and top views of the object plane.

The first development of a light-sheet based microscope was published in 1902 with the work from Henry Siedentopf and Richard Zsigmondy [43]. Their work focused on the creation of a high intensity sheet of non-coherent light in order to visualize dispersed sub-micrometer colloidal particles immersed in a solution, and their microscope was called the *ultramicroscope*. Although usable for other applications, they focused their work on counting and determining the size of minute gold particles usually used for the production of cranberry glass, which had a large market during that time[4]. In 1925, the Nobel Prize in Chemistry was awarded to Zsigmondy in recognition to his advances on colloid research, as well as for the invention of the ultramicroscope.

It took several years and the invention of fluorescence microscopy and lasers until light-sheet methods were rediscovered in 1993 with a technique named *orthogonal-plane fluorescence optical sectioning* (OPFOS) [45]. It was based on the ultramicroscope from Zsigmondy, and allowed the first anatomical 3D

[4]Interestingly, the reddish color of cranberry glass is mainly a consequence of the enhanced absorption and scattering properties of the colloid due to the oscillation of the tiny gold particles when under influence of an external electromagnetic field. For gold, absorption is enhanced around 520 nm.[44]

reconstruction of a fully cleared and stained guinea pig cochlea [46]. Still, during almost an entire decade, none of the published works seemed to be of real interest to the scientific community. Until 2004, when another more versatile version of light-sheet microscope was developed under the name of *single plane illumination microscopy*, or SPIM [11], and soon after the technique reached a broader part of the scientific community, leading to many further advances and imaging methods.

Today, SPIM has become a highly flexible imaging technique which can be fully adapted to the sample of interest [47], being able to cover a wide spatiotemporal range. It is now commonly used with water dipping objectives, as they not only allow the specimen to be embedded in a medium best suited for its survival, but also prevent strong focus shift due to refractive index mismatch between the objective and the specimen. Moreover, the flexibility in creating new microscope designs has allowed light-sheet microscopy to be built around the sample [48]. This is especially important considering that one of the main difficulties in imaging full living tissues maintaining them in the best mounting conditions possible, which cares for high survival rates and prevents them from moving outside of the FOV. Furthermore, its remarkable optical sectioning capabilities allow illumination only around the close vicinity of the object plane, leaving the specimen free of unnecessary light dosage. A dramatic reduction in phototoxicity and photobleaching is a result, laying the foundation for unprecedented long-term imaging of various different specimens. In zebrafish imaging, it has been used for recording early developmental stages and monitoring the functioning of specific organs, including the heart and the brain [49–54]. For *Drosophila* embryos, recordings of more than 20 hours encompassing most of the embryonic development have been acquired with subcellular resolution [4, 55]. Even in light-sensitive samples such as mouse embryos, recordings which span more than 3 days of embryonic development have been possible, generating complete lineage trees and cell fate maps [56], and other works have shed light on their vasculature and neuroanatomy [57, 58]. Light-sheet microscopes with an upright geometry of illumination and detection lenses have also been used for single cell imaging and diffusion measurements [59], and for specific studies in the nematode worm [60]. When combined with superresolution techniques, unsurpassed optical sectioning can be achieved for imaging viruses and cell structures [61]; when utilized with lattice-like illumination methods, fast imaging of subcellular processes can be performed live [62]. Multiple illumination and detection arms can reduce image artifacts by light absorption and scattering, and speed up acquisition rates [53, 63–65]. In addition, this method is particu-

larly powerful when fast recording of entire specimens is needed, as it allows the acquisition of images through different views simultaneously, allowing individual nuclei inside the specimen to be tracked with high precision [4, 55]. This SPIM imaging technique is also the one used for all recordings presented in this thesis, and is based on the MuVi-SPIM microscope setup [4].

1.4.1 Light-sheet designs

At the heart of light-sheet based fluorescence microscopy lies the method for creating the illuminating sheet of light, which follow one of two main approaches. The first method utilizes a cylindrical lens behind the illumination objective. The lens focuses the expanded beam in one direction, leaving its perpendicular direction unchanged. The asymmetrical beam is focused on the back focal plane of the illumination objective, which produces and inverted light sheet, illuminating the entire FOV at once [11, 66]. This is a simple way to produce a light-sheet, which requires the placement of a fixed cylindrical lens and does not need any moving parts or extra electronics.

The second approach relies on the translation of a focused beam throughout the entire FOV during each image acquisition, creating a so-called *virtual light-sheet*. In order to achieve this, a scan mirror is located at an image plane of the back focal plane of the illumination objective. The image plane is created with the addition of two lenses behind the illumination objective, which not only serve as relay optics, but may also expand the beam up to a certain fraction of the diameter of the objective's back aperture. The laser beam is reflected by the scan mirror and enters the illumination objective through the two relay lenses. If the scan mirror changes angles during the acquisition of an image, the focused beam is translated in the FOV, thus being able to scan the entire area. Light-sheet microscopes using this type of illumination are usually called *digitally scanned light-sheet microscopes*, or DSLM [67].

Each illumination method has its positive and negative aspects. Cylindrical lens based light-sheets can produce images at very fast rates shadowing artefacts can limit image quality. However, this can be partially overcome with the creation of light-sheets from different angles throughout the acquisition of each image, thus minimizing the length of the shadows [63]. Furthermore, the utilization of tightly focused light sheets which can be axially swept has been shown to increase optical sectioning capabilites [68].

In DSLM methods, different beam intensity profiles can be chosen for illumination. Although gaussian intensity profiles are of the most common type, being also used in practically all laser sources utilized in fluorescence micros-

copy, other types based on Bessel or Airy functions like profiles have been proposed and are currently used for various applications [62,69–72]. The main interesting feature about Bessel and Airy intensity profiles is that they produced much longer focal regions than gaussian beams, albeit at the cost of being flanked by sidelobes of lower intensity. Additionally, DSLM has so far been the only illumination technique capable of producing light-sheets for two-photon excitation of fluorophores [69, 73–75]. Although theoretically possible, light-sheet creation with cylindrical lenses would require very large laser powers, as the intensity needs to be distributed along the entire volume at once. DSLM also allows the discrimination of scattered light with the introduction of confocal detection into the system via the utilization of a slit-shaped mask, either physically or electronically [76, 77]. This has the great advantage of increasing contrast in the acquired images without the need for post processing, and further eases the acquisition of 3D stacks through multiview approaches [78]. More on multiview light-sheet microscopy is presented in Section 1.4.3; an extensive discussion on novel data fusion methods for multiview light-sheet microscopy with electronic confocal detection is the topic of Chapter 2.

1.4.2 Resolution and spatial constraints in light-sheet microscopy

In light-sheet microscopy, the PSF of illumination and detection are distinct, and thus the effective PSF of the microscope is the product of both. As has been pointed out in Figure 1.6, the detection path of a light-sheet microscope is completely analogous to that of a widefield epifluorescence imaging device. This in turn means that the lateral resolution is basically defined by the lateral dimensions of the detection objective's PSF: considering the fact that water-dipping objectives are used, and using Equation 1.8 with 520 nm fluorescence wavelength, typical single emitter spot sizes lie in the range between 240 and 1000 nm [79]. If the illuminating light-sheet is thicker than the axial PSF of the detection objective, then the latter will define the axial resolution. Moreover, fluorophores excited above and below the detection PSF will most likely contribute to blurr and background noise. Therefore, optimal optical sectioning greatly depends on the shape of the generated light-sheet. Ideally, the entire FOV should be illuminated by an infinitesimally thin and uniform sheet of light. Even though techniques which aim at generating thinner light sheets with the help of either different illumination beam intensity profiles [62, 69–72] or by utilizing superresolution methods for the spatially confined off-switching of fluorophores [61,80] exist, we will focus on defining the math-

ematical grounds for calculating light-sheet dimension for gaussian beams, and kindly refer the reader to the aforementioned publications for further information on the other techniques.

Since we are considering a very thin sheet of light, the angles associated should be small and therefore the paraxial approximation is valid. This means that the electromagnetic wave have nearly parallel wavefront normals. With this approximation a general wave equation can be approximated by the paraxial Helmholtz equation [81]. We will consider light to be propagating in the y direction, as this corresponds to the overall definition of coordiantes presented in Section 1.4.3:

$$\nabla_T^2 U(x,y,z) - i2k\frac{\partial U(x,y,z)}{\partial y} = 0. \tag{1.15}$$

Here, $\nabla_T^2 = \partial^2/\partial x^2 + \partial^2/\partial z^2$ is the transverse part of the Laplace operator, and $U(x,y,z)$ is the complex amplitude of a paraxial wave with an associated wave vector $k = 2\pi/\lambda_0$. Possible eigenfunctions include a Gaussian beam, both in radially symmetric and in elliptical form. Considering the latter:

$$U(x,y,z) = A_0 \cdot \sqrt{\frac{\bar{\omega}_x}{\omega_x(y)}}\sqrt{\frac{\bar{\omega}_z}{\omega_z(y)}} \cdot e^{-\left(\frac{x^2}{\omega_x^2(y)} + \frac{z^2}{\omega_z^2(y)} + i\varphi(x,y,z)\right)}, \tag{1.16}$$

with A_0 and $\varphi(x,y,z)$ the amplitude and phase of the wave profile. $\bar{\omega}_x$ and $\bar{\omega}_z$ correspond to the transversal radii at the thinnest position of the gaussian profile. They are commonly denoted as the beam waist, in this case along the x and the z directions. $\omega_x(y)$ and $\omega_z(y)$ are hyperbolic functions which describe the shape of the beam along its propagation direction y:

$$\omega_x(y) = \bar{\omega}_x\sqrt{1 + \left(\frac{y}{\bar{y}_x}\right)} \tag{1.17}$$

$$\omega_z(y) = \bar{\omega}_z\sqrt{1 + \left(\frac{y}{\bar{y}_z}\right)} \tag{1.18}$$

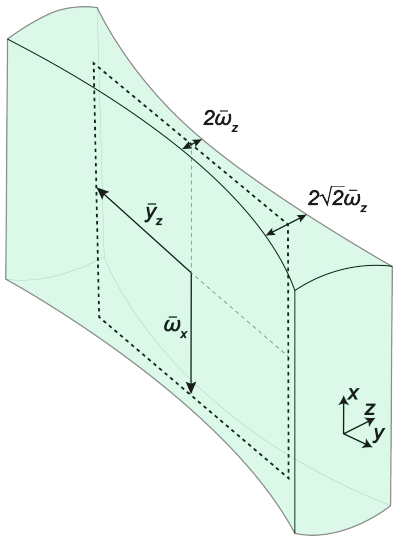

Figure 1.7: Resolution aspects in light-sheet microscopy. Schematics of a light-sheet volume in green, with the dashed square depicting a possible field of view of detection.$\bar{y}_z$ is the extent of the Rayleigh range along the axial direction, i.e. the distance to which the beam waist in $\bar{\omega}_z$ is increased by a factor $\sqrt{2}$; $\bar{\omega}_x$, the extended beam waist in x direction. Together with $\bar{\omega}_z$, these values delimit the illumination volume where the light-sheet is thinnest, in this case slightly smaller laterally than the FOV.

It is common to define a specific distance $\bar{y}_x$ and $\bar{y}_z$ to the beam waist, related to its increase by a factor $\sqrt{2}$. This is denominated the Rayleigh range, and relates to the beam waists $\bar{\omega}_x$ and $\bar{\omega}_z$ through:

$$\bar{y}_x = \frac{\pi n \bar{\omega}_x^2}{\lambda} \tag{1.19}$$

$$\bar{y}_z = \frac{\pi n \bar{\omega}_z^2}{\lambda} \tag{1.20}$$

Elliptical Gaussian beams are widely used in light-sheet microscopy, in particular with the usage of cylindrical lenses, and is depicted in Figure 1.7. Their intensity is equal to $U(x,y,z) \cdot U^*(x,y,z)$, yielding:

$$I(x,y,z) = |A_0|^2 \cdot \frac{\bar{\omega}_x}{\omega_x(y)} \cdot \frac{\bar{\omega}_z}{\omega_z(y)} \cdot e^{-2\left(\frac{x^2}{\omega_x(y)} \cdot \frac{z^2}{\omega_z(y)}\right)}. \tag{1.21}$$

If the microscope has a scanned beam illumination unit, the solution to be considered is that of a radially symmetric beam. In this case, all dependencies in x and z direction vanish, simplifying the equations above via:

$$\bar{y}_x = \bar{y}_z = \bar{y}$$
$$\bar{\omega}_x = \bar{\omega}_z = \bar{\omega}$$
$$\omega_x(y) = \omega_z(y) = \omega(y).$$

1.4.3 Multiview light-sheet microscopy

Multiview light-sheet microscopy aims at providing an *in toto* view of the specimen by imaging it from different angles. The main motivation behind is the fact that photons entering or leaving a tissue suffer a certain amount of scattering events which increase with tissue depth [82]. Therefore, the best way to reach the far side of a highly scattering specimen is simply by imaging it from the other side, generating to data from a so-called different *view* of the embryo. Typically more than just two views are necessary for having a high quality 3D representation of the entire sample [4, 53, 65, 83], and in fact the ideal 3D volume being would only be acquired if recordings from all possible angles could be combined [42].

Multiview recordings with light-sheet microscopy can be achieved via different approaches, depending on which kind of light-sheet microscope is utilized. For a microscope setup with only one illumination or one detection objective, far regions of the sample where scattering heavily contributes in loss of contrast will always be present in the final recorded volume. The only way to replace this far-side blur is through acquisition of image stacks in complementary volumes after a corresponding sample rotation, which allows the creation of a single 3D dataset where only high-contrast parts of each volume are merged together into one high quality dataset. For this approach to be successful, however, all different views need to be brought to the same coordinate system through registration with fiducial markers and/or image based algorithms[4, 42, 55, 84]. After this is performed, a weight functions need to be applied to each view so that only high contrast regions are taken into account for the creation of the final 3D dataset - a process called *fusion*. Furthermore, the amount of time required to acquire all the multiview datasets needed for the full 3D representation of the specimen at a certain point in its developmental stage scales with the amount of rotations needed: too many rotations will invariably lead to image artefacts as the specimen develops during acquisition, also increasing the chance of phototoxicity and fluorophore photobleaching. Another possibility is to make usage of light-sheet setups with two opposing illumination and one or two detection objective lenses [4, 53, 55, 63, 64], which

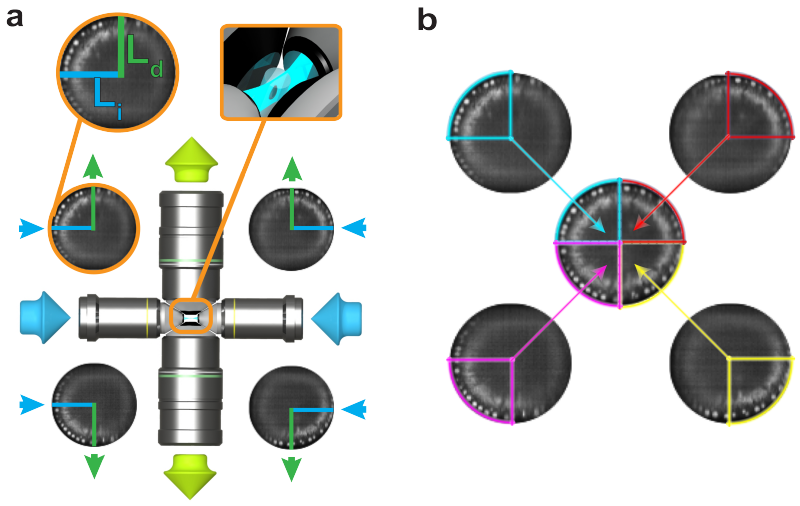

Figure 1.8: Multiview light-sheet imaging with sequential illumination.(a) Multiview light-sheet setups with four lenses illuminate the sample in a sequential manner, obtaining four different stacks. For each of them, the optical path of illumination (L_i) and detection L_d can be related to the transport mean free path and provide insight on scattering contributions. **(b)** All four stacks need to be fused together so that only the subvolumes which have minimal overall illumination and emission scattering contributions (colored areas) are combined into a full 3D dataset (center).

aim at yielding an *in toto* view of the sample by sequentially illuminating from two opposing directions while imaging the sample from opposite directions, either through rotation or directly with two opposing cameras, as can be seen in Figure 1.8a,b. Opposing camera detection is especially desirable considering that it can be fast enough to follow fast biological processes without the need for physically rotating the sample many times in space.

However, also with the utilization of two illumination and two detection objectives all four views need to be registered and computationally fused into a single 3D dataset.

However effective, fusion algorithms are usually marker and sample dependent, as they need to take into account the scattering properties of the biological tissue. Additionally, the fusion weight functions require adaptation throughout time, as the specimen develops, changing its shape and optical properties. As will be discussed in Section 1.5, scattering and absorption properties of tissues are complex and in many aspects still little understood. This is one of the reasons why, especially for data storage intensive experiments - e.g. for the case of long timelapses and/or large stacks – light-sheet specific data post-processing poses a major computational bottleneck for a wider spread of the usage of multiview light-sheet microscopy. An extended discussion on multiview image acquisition, related to fusion algorithms and image contrast enhancement is the main topic covers later on in Chapter 2.

3D data: definitions and visualization methods

With the further establishment of 3D fluorescent imaging through the development of light-sheet, it becomes necessary to be able to present the available data in a clear and congruent way. This is not only important from a general scientific perspective, but its necessity also becomes more apparent when only part of the 3D data is shown through sections which can have virtually any orientation.

In order to facilitate the reader in understanding the orientations used throughout this work to display 3D data, we define a coordinate system as exemplified in Figure 1.9. The figure shows the cartoon of a fruit fly embryo depicted as an ellipsoid, along with the two planes that define the the two main sections. These will be referred to as an *in-plane* (or, depending on the case, *sagittal*) section and a *cross*-section, or as xy-plane and xz-plane sections respectively. The definition of the spatial coordinates stems from the axes considered when moving the sample in our multiview light-sheet microscope.

Sections are, nonetheless, sometimes not enough, and a larger picture of the entire 3D volume is needed. Maybe the most accepted way to show 3D datasets is to project them into 2D images using a transformation of choice. It exchanges one entire spatial dimension with another visual cue (which, for example, can be based on intensity or color coded depth discrimination), allowing the analysis to focus on simplified shapes. Another approach is to use 3D visualization software which can also explore other ways to manipulate data in space, and perform simple analysis in 3D. In this thesis, Fiji [85] and Chimera [86] have been extensively used for visualization, analysis, and preparation of data. Other analyses have been performed with the usage of Matlab®.

Other strategies for visualizing 3D data exist albeit not yet having reached the strong interest of the scientific community. Lenticular prints, for example, utilize a transparent plate made out of an array of small cylindrical lenses which can be mounted on top of an interlaced version of a 3D dataset to show it in real 3D to the observer. This is achieved as the interlaced image contains the 3D dataset viewed from different complementary perspectives, all of them placed behind each lens for the corresponding part of the image. This concept is not new, and it is continuously used to produce interesting postcards or advertisements; its usage to show scientific data is, however, still very low[5]. A

[5] One interesting side effect of utilizing such an approach to visualize scientific data is its power in making already beautiful 3D images an unique characteristic, with a strong artistic side. One example

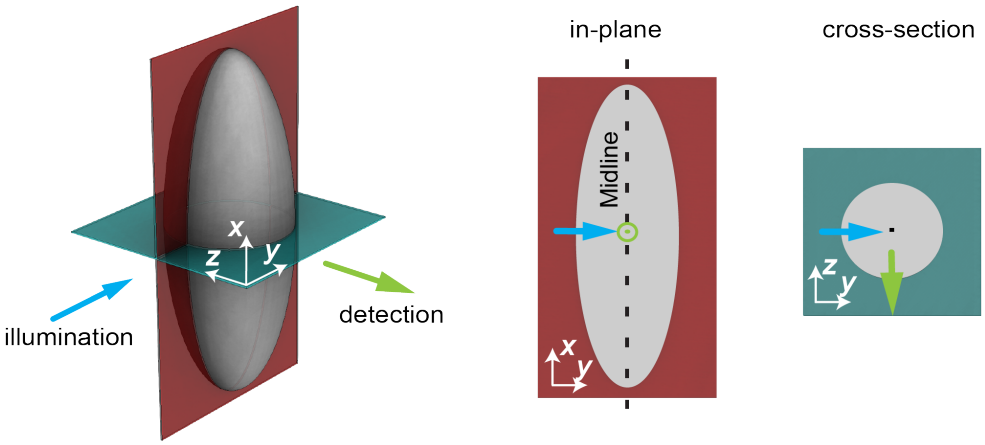

Figure 1.9: Definition of the spatial coordinate system. Depiction of a fruit fly embryo in gray, with typical light-sheet illumination and detection directions shown with blue and green arrows, respectively. Definition of axes in white allows us to define cross-sections along the long (red) and short (green) embryonic axes.

more recent technology is virtual reality. It allows the user to be immersed inside the 3D data, and visualize it from all possible angles trough utilization of special screens, goggles, etc. Groups can also share the same information with the same spatial freedom, making the understanding of e.g. cell migration or large intricate morphological events an interactive discussion. Although still in its infancy, it is a rapidly growing community and it is expected that in the near future such visualization techniques can be used routinely in labs which have to deal with large three dimensional datasets.

can be seen in [87]

1.5 Absorption and scattering effects in fluorescence microscopy

The main problems faced by fluorescence microscopy in the life sciences and in biology are the effects of absorption and scattering of illumination and emitted light. As any tissue is a composed by a multitude of different molecules and complexes, these esffects are highly tissue specific and, in the case of live specimens, continuously change over space and time. This makes the propagation of photon energy completely non-uniform throughout space, varying according to the tissue properties. The propagation of photon energy is also denoted as *radiance*[6], and can be defined by:

$$L(\mathbf{r}, \hat{\mathbf{s}}, t) = N(\mathbf{r}, \hat{\mathbf{s}}, t) \cdot h\nu c_t \qquad [\mathrm{W\,m^{-2}} \cdot \mathrm{sr}], \tag{1.22}$$

where $N(\mathbf{r}, \hat{\mathbf{s}}, t)$ [$/\mathrm{m}^3/\mathrm{sr} \perp \mathrm{s}$] is the number of photons per unit volume and unit time in the direction of the unit vector $\hat{\mathbf{s}}$ and within the solid angle dw. c_t is the speed of light in the tissue dependant on its refractive index η_t, $c_t = c/\eta_t$. The photon density [photons/m^3] is then defined as

$$N_0(\mathbf{r}, t) = \int_{4\pi} N(\mathbf{r}, \hat{\mathbf{s}})\, d\omega \tag{1.23}$$

This allows us to define the *fluence rate* [$\mathrm{W\,m^{-2}}$] related to $N_0(r)$ as

$$\Phi(\mathbf{r}, t) = N_0(r, t) \cdot h\nu c_t, \tag{1.24}$$

and through Equation 1.22 and 1.23 we arrive at:

$$\Phi(\mathbf{r}, t) = \int_{4\pi} L(\mathbf{r}, \hat{\mathbf{s}}, t) d\omega, \tag{1.25}$$

In general, a collimated laser beam with uniform incident irradiance Φ_0 [$\mathrm{W\,m^{-2}}$] will be attenuated according to Beer-Lambert's law:

$$\Phi_p(z) = \Phi_0 \cdot e^{-\mu_t z}, \tag{1.26}$$

with $\Phi_p(z)$ [$\mathrm{W\,m^{-2}}$] is defined as the primary fluence rate of the collimated beam at a certain tissue depth z. μ_t [m^{-1}] is called the *attenuation coefficient*,

[6] In the literature, the terms used for radiometric parameters such as fluence, irradiance, intensity, and energy dose are often somewhat confusing. Throughout this work, the following agreements are met: *power* and *intensity* are expressed in units of W, *energy* in units of J, the synonyms *power density*, *fluence rate* and *irradiance* in $\mathrm{W\,m^{-2}}$, and *energy dose* in units of $\mathrm{J\,cm^{-2}}$.

and relates to absorption and scattering tissue properties as:

$$\mu_t = \mu_a + \mu_s \tag{1.27}$$

Here μ_a $[m^{-1}]$ and μ_s $[m^{-1}]$ are the absorption and scattering coefficients. The optical albedo is a helpful dimensionless number which relates de degree of scattering in respect to the attenuation coefficient:

$$\alpha = \frac{\mu_s}{\mu_t} \tag{1.28}$$

The penetration depth l_t is defined as the mean free path for an absorption or scattering even t where $\Phi_p(l_t) = \Phi_0 \cdot e^{-1}$, i.e. where there is a reduction to 37% of transmitted light:

$$l_t = \frac{1}{\mu_t}. \tag{1.29}$$

l_t does not assume multiple scattering events; this will be discussed in Section 1.5.2. Measurements of μ_s rely on transmission of a collimated beam through a certain tissue thickness d such that $\mu_s = -ln(T_c)/d$. However, this is a non-trivial task, as the mean free path inside tissues can easily be of the order of 100µm or less in order to avoid multiple scattering [88, 89]. Not only such thin slices are difficult to handle, but most importantly at this thickness the heterogeneity of tissues becomes apparent, and the measurements themselves can only provide limited information.

Our goal in the next subsections is to present some of the most important considerations on absorption and scattering effects which relate to μ_a and μ_s used in Equation 1.26. On the absorption, we will briefly discuss general characteristics of the absorption coefficient in tissues, showing examples on its strong wavelength dependance. On scattering, we intend to present the transport mean free path, μ_t' by motivating our way towards the transport radiative equation and briefly mentioning the diffusion approximation. We will end with a discussion on properties of the transport scattering coefficient.

1.5.1 Absorption of light inside tissues

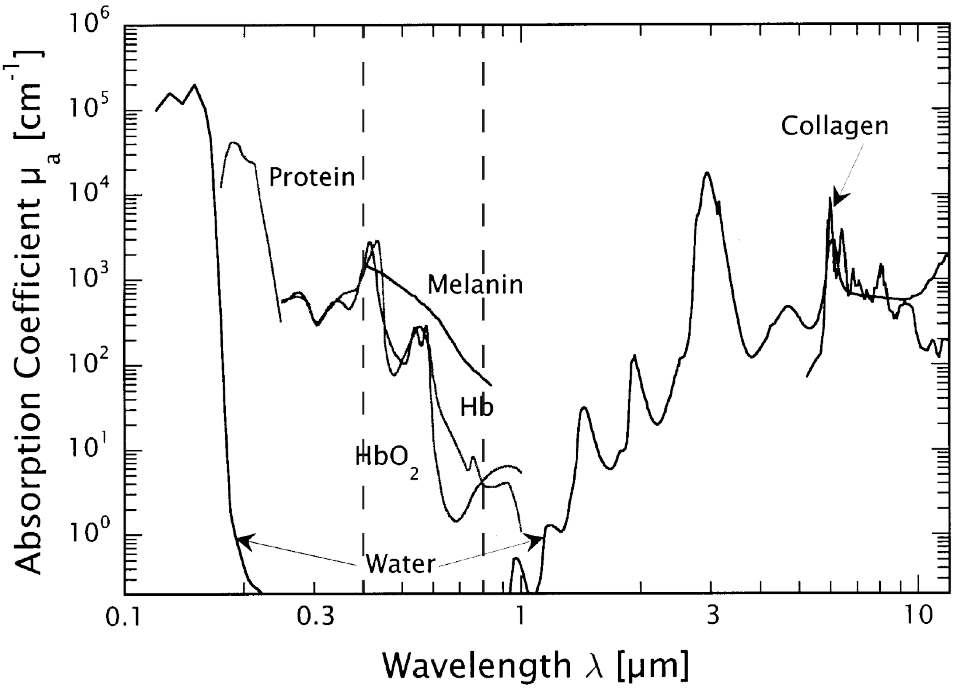

Figure 1.10: Optical absorption coefficient of principal tissue chromophores in the 0.1 − 12 µm spectral region. The visible region around 400 − 800 nm is shown between dashed lines. Modified from [90].

If scattering can be neglected, Equation 1.26 depends mainly on μ_a, and light distribution inside the tissue follows an exponential attenuation. In electromagnetic theory, μ_a is function of the wavelength, as can be seen if we consider the incident electric field to be a planar wave with frequency ω and amplitude E_0 propagating in the z direction:

$$\boldsymbol{E} = \boldsymbol{E_0} \cdot e^{i[kz-\omega t]}. \tag{1.30}$$

Using the dependance of the wavenumber on the real and imaginary parts of the tissue's refractive index, $k = \omega n(1 + i\kappa)/c$, we can separate the exponent into real and imaginary parts:

$$\boldsymbol{E} = \boldsymbol{E_0} \cdot e^{-n\kappa\frac{\omega}{c}z} e^{i\left[n\frac{\omega}{c}z-\omega t\right]}. \tag{1.31}$$

and since $\Phi \propto |E|^2$, we arrive at

$$\Phi(z) = \Phi_0 \cdot e^{\frac{2\omega}{c}n\kappa z}. \tag{1.32}$$

Taking into account that $\omega = 2\pi c/\lambda_0$ comparing to Equation 1.26, we have:

$$\mu_a = \frac{4\pi\kappa}{\lambda} \tag{1.33}$$

which relates the absorption coefficient μ_a with the extinction coefficient κ and the wavelength in the medium [35].

Although Equation 1.33 provides a good approximation for dielectrics, this result does not completely hold for tissues, where the different molecular symmetries allow for absorption peaks throughout the spectrum. This is represented in Figure 1.10. Above the wavelength of 1.4 µm and below 200 nm, light absorption by water molecules play a significant role; in fact, proteins and other molecules already start showing strong absorption below 400 nm. Other works have measured or modelled light absorption through specific molecules or tissues with different content distribution [82, 91–93] .

1.5.2 Propagation of scattered light

Biological tissues are highly inhomogeneous, and scattering effects cannot be neglected. Measurements performed in human skin show that the scattering have much stronger effects than absorption, as exemplified in Figure 1.11 - a definition on μ_s' will be presented further in this section.

In fact, considering usual sizes of embryos alone, which average between 100 µm - 500 µm thickness, photons coming from a collimated light source will invariably undergo multiple scattering events before reaching the far side of the tissue. Scattering is considered here to be an elastic process: incident photons are absorbed and re-emitted negligible loss in energy, though with a possible change in propagation direction. These events can contribute to various different effects, including the increase of the fluence rate just below the tissue surface to values above that of the incident irradiance, as well as the extent of the fluence rate beyond the lateral dimensions of the collimated beam diameter. A description of light propagation with multiple

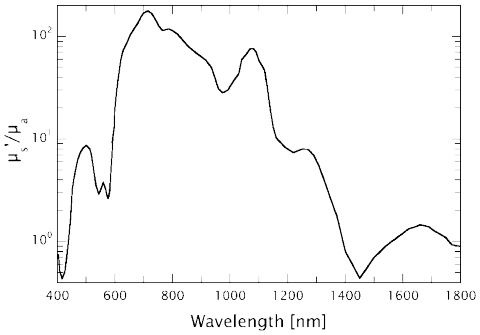

Figure 1.11: Ratio of reduced scattering to the absorption coefficients of human skin. For spectral regions below 450 nm and above 1800 nm optical absorption, from hemoglobin and proteins in the ultraviolet and water in the mid- and far-infrared dominates the optical properties. In between it is possible to characterize the tissue - in spatial regions far away from single scattering events - with mainly diffusive character [82, 93, 94]. Unmodified from [94], which was modified from original [95].

scattering events utilizing Maxwell's equations is not valid anymore. An approach widely used is the implementation of transport theory describing the transfer of radiative energy throughout a turbid medium[82, 93, 96]. It takes into account several efects. First, it considers that the radiance $L(\mathbf{r}, \hat{\mathbf{s}}, t)$ should decrease, due to scattering and absorption, with each infinitesimal length ds inside the tissue:

$$dL(\mathbf{r}, \hat{\mathbf{s}}, t) = -ds(\mu_a + \mu_s)L(\mathbf{r}, \hat{\mathbf{s}}, t) \tag{1.34}$$

Additionally, $L(\mathbf{r}, \hat{\mathbf{s}}, t)$ should increase due to scattered light which promotes radiance from all other directions $\hat{s}'$ into $\hat{s}$ at a certain position $\mathbf{r}$ in space:

$$dL(\mathbf{r}, \hat{\mathbf{s}}, t) = ds \int_{4\pi} \mu_s P(\hat{\mathbf{s}}', \hat{\mathbf{s}}) L(\mathbf{r}, \hat{\mathbf{s}}', t) d\Omega' \quad , \tag{1.35}$$

with $d\Omega = \sin\theta d\theta d\phi$ the elementary solid angle. $P(\hat{\mathbf{s}}', \hat{\mathbf{s}})$ is the phase function. It describes the probability of a photon travelling from direction $\hat{\mathbf{s}}$ undergoing a single scattering event leading to a change in direction within the solid angle $d\Omega'$ around $\hat{\mathbf{s}}'$. Since it is a probability density function, the evaluation of $P(\hat{\mathbf{s}}', \hat{\mathbf{s}})$ over all angles should be unity:

$$\int_{4\pi} P(\hat{\mathbf{s}}', \hat{\mathbf{s}}) d\Omega' = 1 \quad , \tag{1.36}$$

and here we assume $P(\hat{\mathbf{s}}', \hat{\mathbf{s}})$ to be already normalized.

Oftentimes $P(\hat{\mathbf{s}}', \hat{\mathbf{s}})$ depends only on the angle θ between scattered and incident directions, so $P(\hat{\mathbf{s}}', \hat{\mathbf{s}}) = P(\hat{\mathbf{s}}' \cdot \hat{\mathbf{s}})$, with $\hat{\mathbf{s}}' \cdot \hat{\mathbf{s}} = \cos\theta$. It is then possible to define a scattering anisotropy function g which represents the expectation value of the cosine of scattering angle θ.

$$g = \frac{\int_{4\pi} P(\hat{\mathbf{s}}', \hat{\mathbf{s}})(\hat{\mathbf{s}}' \cdot \hat{\mathbf{s}}) d\Omega'}{\int_{4\pi} P(\hat{\mathbf{s}}', \hat{\mathbf{s}}) d\Omega'} = \int_{4\pi} P(\hat{\mathbf{s}}' \cdot \hat{\mathbf{s}})(\hat{\mathbf{s}}' \cdot \hat{\mathbf{s}}) d\Omega' = \langle \cos\theta \rangle. \tag{1.37}$$

Photon scattering in tissues is generally highly anisotropic, with $0.7 < g < 1$ [82, 88, 92, 97]. There are many different scattering phase functions $P(\theta)$; the most used is the Henyey-Greenstein phase function which can be written as [82]:

$$P(\cos\theta) = \frac{1 - g^2}{(1 + g^2 - 2g\cos\theta)^{3/2}} \quad \text{with} \quad \frac{1}{4\pi} \int_{4\pi} P(\cos\theta) d\Omega = 1. \tag{1.38}$$

Finally it is also necessary to consider a *source term* $S(\mathbf{r}, \hat{\mathbf{s}}, t)$ [$\mathrm{W\,m^{-3}\cdot\,sr}$]

which encompasses all energy produced by any source within the volume and solid angle elements per unit time. Joining all these parts together we arrive at the *radiative transport equation*, also known as Boltzmann equation[82, 93]:

$$\frac{\partial L(\mathbf{r},\hat{\mathbf{s}},t)}{\partial t} + \hat{\mathbf{s}}\cdot\nabla L(\mathbf{r},\hat{\mathbf{s}},t) = -\mu_t L(\mathbf{r},\hat{\mathbf{s}},t) + \\ + \mu_s \int_{4\pi} P(\hat{\mathbf{s}}'\cdot\hat{\mathbf{s}}) L(\mathbf{r},\hat{\mathbf{s}}',t) d\Omega' + S(\mathbf{r},\hat{\mathbf{s}},t) \tag{1.39}$$

Solving Equation 1.39 for $L(\mathbf{r},\hat{\mathbf{s}}',t)$ is not enough, as the calculation of the fluence rate through integration of the radiance - Equation 1.25 - is still necessary in order to be compared with experimental data. Additionally, radiance inside a turbid medium can be divided into a coherent and a diffusive term according to $L(\mathbf{r},\hat{\mathbf{s}},t) = L_c(\mathbf{r},\hat{\mathbf{s}},t) + L_d(\mathbf{r},\hat{\mathbf{s}},t)$. Although for the first term single scattering predominates and the coherent radiance is mainly affected by attenuation due to absorption and scattering of the direct beam, following Beer-Lambert's law, the diffusive part requires additional approximations and statistical approaches to best characterize the change in direction due to multiple scattering. These need to be chosen according to information known or expected from the tissue, such as its albedo, and are usualy calculated with help of Monte Carlo simulations. The most usual approximation relies on diffusion theory, which assumes that the radiance has a high albedo (i.e. $\mu_a \ll \mu_s$, which, for most of the visible spectrum seems true according to Figure 1.11), and that the scattering medium is nearly isotropic after sufficient scattering events. It ultimately leads to the diffusion equation, which can be used to solve for the fluence rate instead of the radiance[7]. It also directly depends on the anisotropy factor g by defining the *transport* (or reduced) *scattering coefficient* μ_s':

$$\mu_s' = (1-g)\mu_s \quad , \tag{1.40}$$

which leads to the *transport* (or reduced) *interaction coefficient* μ_t':

$$\mu_t' = \mu_a + \mu_s'. \tag{1.41}$$

The reciprocal of μ_t' is denominated the *transport mean free path* l_t'

[7] For more detailed information on its derivation through the diffusion approximation can be found in [82, 92, 93].

$$l_t' = \frac{1}{\mu_t'}. \tag{1.42}$$

l_t' relates to l_t from Equation 1.29, and considers the case of multiple scattering through the anisotropy factor g and μ_s'. Measurements of transmission and reflection of light through tissue have shown that μ_s' has a strong tendency towards forward scattering, with g values typically above 0.7[88, 97].

Single scattering events can be modelled in order to predict μ_s' values in regions close to the tissue boundaries, i.e. where $L_c(\mathbf{r}, \hat{\mathbf{s}}, t)$ is the main scattering effect. Utilizing solutions from electromagnetic theory, it is possible to approximate μ_s' via a distribution of spherical scatterers with different sizes in the tissue, as a function of the desired wavelength and scattering power. Since we are considering the whole process to e elastic, it can be initially divided into two categories, depending on the ratio between the size of the scatterer and the wavelength of light. This ratio can be defined as $(2\pi r)/\lambda$, with r an approximate scatterer radius. When $r \ll \lambda$, Rayleigh-like scattering is the predominant effect, with a particularly strong λ^{-4} wavelength dependency. For larger particles, when $r \geq \lambda$, an approximation with a variable scattering power b_L for large scatterers can be performed, yielding[89]:

$$\mu_s'(\lambda) \approx a' \left(f_R \left(\frac{\lambda}{\lambda_0} \right)^{-4} + (1 - f_R) \left(\frac{\lambda}{\lambda_0} \right)^{-b_L} \right). \tag{1.43}$$

Here a' [m^{-1}] is a common scaling factor, corresponding to $\mu_s'(\lambda = \lambda_0)$, f_R accounts for probability of isotropic Rayleigh-like scattering, and $(1 - f_R)$ is the fraction which corresponds to larger particle scattering; b_L is the fitting variable which is denominated the *scattering power* of the particle distribution with sizes comparable or larger than λ, and scatter light with a strong forward anisotropy.[8] Equation 1.43 has been shown to work quite well with measure data of μ_s' from several different tissue samples, such as brain, skin, bone, fibrous tissues and fatty tissues[89][9]. Additionally, it provides a clear monotonically decreasing function for μ_s' in function of λ, which has also been observed, especially in the spectral region between 400 nm and 1300 nm. This is an interesting which also greatly motivates the usage of light with longer wavelengths

[8] In fact, $(1 - f_R)(\lambda/\lambda_0)^{-b_L}$ is commonly denominated as *Mie scattering* component. This can be confusing, as Mie theory actually provides exact solutions to Maxwell's equations for the case of a plane monochromatic wave scattered by a homogeneous sphere of radius r with an isotropic refractive index n_r. Rayleigh scattering is just a special case when $\bar{r} << 1$, $\bar{r}$ being a normalized radius.

[9] It is unfortunately outside the scope of this thesis to go deeper into other approximations utilizing electromagnetic theory. More about this and other approaches can be found in the literature[82, 93, 96, 98].

in illumination and fluorescence emission. Many synthetic dyes have already been created to work in the far-red and infrared parts of the spectrum (e.g. Alexa 647-790, Cy5.5, sytox Red), and novel infrared fluorescent proteins are opening the road towards endogenous infrared labelling of proteins [7]. More on this topic is devoted in Chapter 3.

In summary, a collimated light beam traversing through tissue undergoes multiple scattering events, which gradual cumulative effects that shifts its collimated ballistic behaviour into a diffusive scattered distribution ultimately ending with no directional information[88]. The transport mean free path l_t', characterizes a length scale in which the original directionality is still preferential due to high values of the anisotropy factor g. The transport scattering coefficient μ_s' can also be modelled in terms of the distribution of scatterers, in which the monotonically decrease in scattering as a function of wavelength becomes apparent. Generally speaking, transport theory provides an heuristic model based on statistical approximation of photon transport in multiple scattering medium. It considers scattering to be elastic, scatterers to be non-interfering - thus neglecting effects of diffraction and refraction - and usually does not consider the polarization of laser sources. Even so, it provides a basic understanding on the role of scattering and its effects on photon propagation inside turbid media.

Since tissues are comprised of a complex distribution of structures with variable sizes, more accurate measurements on their optical properties must take into account the level of detail needed for a determined dataset: so far it seems unlikely that one single model can fit so many different degrees of freedom in a reliable way. This way lengthy calculations with minimal macroscopic effect can be avoided, thereby creating model tissues that best represent the portion of the real tissue which will most influence the dimensions considered.

1.5.3 Scattering in light-sheet microscopy

The optical geometric arrangement in light-sheet microscopy allows scattering to be observed with an analogous consideration as given for the calculation of the effective PSF in Section 1.4.2. Since illumination light comes from the side, scattering from incoming and emitted light can be seen as two components of a general scattering distribution inside the tissue, as represented in Figure 1.12a. Planes imaged just inside the tissue will present higher contribution of illumination scattering, since there is very little tissue depth which needs to be covered by emitted photons. At greater depths this scene changes,

up to the point where emission scattering prevails over illumination. For highly scattering, cylindrically symmetrical specimen, this means that only a small part of the entire specimen can be acquired with high contrast. This is one of the main reasons which motivate the acquisition of data in a multiview fashion, with acquisition of images from multiple different angles. This approach is discussed in Section 1.4.3. Figure 1.12b a real case scenario, with the overlay of an unscattered beam in white with the same parked beam entering a *Drosophila* emrbyo from the side.

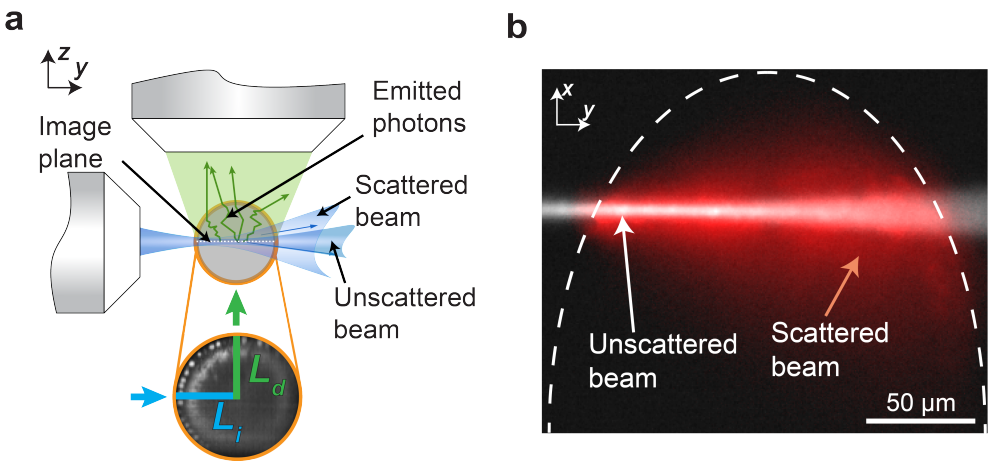

Figure 1.12: Scattering contributions in light-sheet microscopy. (a) Schematics of a illuination and detection objectives of a two-lens light-sheet microscope, viewed from the top. The sample in gray scatters light in both illumination and detection directions, with typical illumination and emission scattering paths lengths described as L_i and L_d respectively. **(b)** Example of the combined effect of illumination and emission scattering with image recorded 65 µm inside a drosophila embryo. the unperturbed beam (in white) is manually overlayed with the scattered one (red) for comparison. dashed lines represent the outline to the anterior pole of the embryo utilized. Emission scattering cannot be directly assessed through this image.

Apart from two-photon light-sheet imaging [69, 74, 99, 100], where two-photon processes need illumination wavelengths to be much longer than the emitted light, emission scattering has usually lower values than illumination, due to its greater effective penetration depth.

One way to prevent the *detection* of scattered photons is through the implementation of a confocal system into the optical path. This has been proposed in several strategies, all of them utilizing the shape of a slit in order to mostly discriminate scattering coming from the direction perpendicular to the illumination's optical axis on the FOV [72, 76, 77]. The development of on-chip confocal slit detection for multiview light-sheet imaging is the main topic of discussion from Chapter 2.

Yet another way to minimize scattering is by the shifting the distribution of emitted photons towards a more ballistic behaviour. For this case, fluorescent proteins that shine in the infrared spectrum are one option of choice. This is

the exact method behind the results presented in Chapter 3.

1.6 Tissue manipulation with light

Microscopy can also be seen in the context of not only being about the acquisition of images of usually minute samples, but also encompassing the observation of recorded cell, tissue, organ, or whole animal response to certain pre-defined perturbations. These are valuable sources of information which work in complementarity to the sole observation of natural behaviour. These perturbations can be of different form, genetic, chemical of physical. Tools for genetic manipulation (such as the phiC31 integrase or the CRISPR/Cas systems [101,102]) and chemical perturbations with drugs and/or other compounds, allied with modern imaging techniques (Light or electron microsopy, x-ray crystallography, etc) may provide important information on the related biological processes involved in the experiment. However, these biologica responses are usually bound to a typical timescale of seconds to many hours. Additionally, genetic or chemical manipulations may often suffer from unspecific effects, many times affecting other biological properties which can change the system of study in various ways.

Physical manipulations through application of pressure, temperature variations, and locally exerted forces through pulling, pushing or suction can be performed in much faster timescales if needed, usually providing quasi-immediate readout. In particular, photomanipulation of tissues allow highly non-invasive perturbations with strong localized spatiotemporal precision[10]. It allows the infliction of photoinduced damage through e.g. chemical, thermal or ablative processes, exertion of forces though optical tweezes, etc. These effects are commonly used for molecular and organismal studies, being important tools for the perturbation of tissues in a range of time (typically ps - s) and spatial scales (nm-mm).

Photoinduced mechanisms in tissues

We will subdivide possible laser-tissue interactions into four different subcategories: photochemistry, photothermal damage, photoablation, as well as plasma-induced ablation and photodisruption. This seemingly rigid classifi-

[10] Optogenetics is maybe the only type of perturbation which couples the precise and fast control of light-mediated molecular switching with a subsequent biological cascade of events, as it indirectly probes the sample by triggering molecular conformational changes of proteins which then lead to the desired effect through natural biochemical pathways [103, 104].

cation should not be taken so strict: as will be further discussed below (as well as throughout the examples presented in Chapter 4), different photoinduced mechanisms may occur using same interaction parameters, as a consequence of tissue properties dependence - molecular distribution and tissue depth, for example. These can be dynamically varying in space and time, and usually cannot be controlled via external means. Figure 1.13 presents an almost linear dependency between the power density and the time of interaction, with all interaction mechanisms lying whithin the range of $0.1 - 100\,\mathrm{J\,cm^{-2}}$, demarked through lines of constant fluence. This implies that the *specific energy dose* required to achieve a laser-induced biological transformation is *nearly constant*, and that the time of interaction needed to deliver a certain known amount of energy is the main relevant parameter. For pulsed lasers sources, this corresponds to the pulse width, and for cw lasers the total exposure time [92, 95].

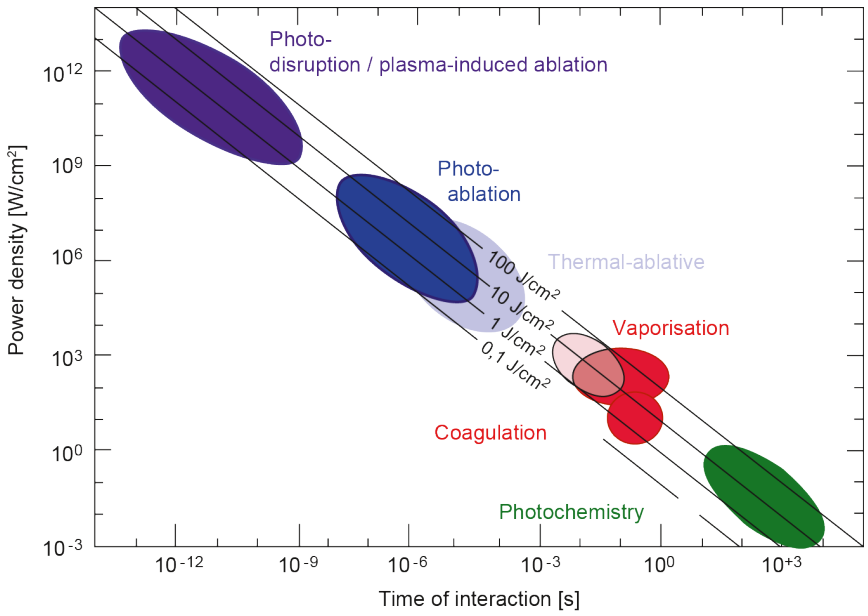

Figure 1.13: Laser-tissue interaction mechanisms. This graph shows a collection of different interaction types, which basically lie whithin the 10-1000 $\mathrm{J\,cm^{-2}}$ fluence band. The strong correlation between intensity and time demonstrates that the energy dose required to achieve a biological transformation in a laser-induced way is almost constant: the time necessary to deliver this amount of energy is the important variable which distinguish the different interactions. Modified from [94], with original from [95].

Photochemistry

Photochemical reactions can be easily found in nature, maybe the most famous example being photosynthesis. It relies on the observation that at low power densities and long exposure times - usually smaller than $1\mathrm{W\,cm^{-2}}$ and exposure times from seconds up to continuous wave - light can act as a catal-

izer, inducing chemical effects and reaction whithin tissues. This effect is also known as *biostimulation*, and can lead e.g. to increased cell proliferation and tissue oxygenation [92, 94].

Photothermal damage

Photothermal effects encompass a large group of interaction types, all of them dependant on the amount of heat which is created through the absorption of irradiated photons. Through careful control of exposure time and laser powers it is possible to tune the peak level of temperature rise achieved, and inflict the different types of induced damage. Among them are coagulation, carbonization, cauterization, vaporisation and melting. Thermal reactions are mostly dependant on the chosen irradiation wavelength and the absorption coefficient μ_a of the tissue. Unlike photochemical reactions, these processes are rather unspecific, leading to the spread of irradiated energy through thermal diffusion. In order to have confined interaction volumes, pulsed lasers with short pulse lengths and small repetitions rates[11], along with exposure times shorter than the thermal diffusion time are necessary[12]. Heat diffusion is characterized by a time dependant *thermal penetration depth*:

$$z_{th}(t) = \sqrt{4\kappa t} \quad \text{with} \quad \kappa = \frac{k}{\rho c_p}. \tag{1.44}$$

Here κ [$\mathrm{m^2\,s^{-1}}$] the *thermal diffusivity*, dependant on the ratio between the thermal conductivity k [$\mathrm{W\,m^{-1}\cdot K}$], and density ρ [$\mathrm{kg\,m^{-3}}$] times the specific heat capacity c_p [$\mathrm{J\,kg^{-1}\cdot K}$] of the tissue. z_{th} corresponds to the distance from the source at which the temperature has dropped to $1/e \approx 0.37$ of its maximum. Disregarding scattering effects, and taking into account Beer-Lambert's exponential decay with the penetration depth dependant on the absorption coefficient $z = 1/\mu_a$, and plugging this into Equation 1.44, it is possible to define the *thermal diffusion time*:

$$\tau_{th} = \frac{1}{4\kappa\mu_a^2}. \tag{1.45}$$

Usually thermal effects can be clearly seen for laser intensities above 10 $\mathrm{J\,cm^{-2}}$. Illumination can be either of continuous wave or with pulsed lasers keeping interaction time $\geq$ 1ms. Of all existing thermal interactions possible,

[11] High repetition rates may lead to accumulation of thermal efects, as thermal diffusion is not fast enough to compensate the incoming temperature increase from the following pulse.

[12] Derivation on the heat diffusion equation, along with its solutions, can be found in [92].

especial focus will be given to *tissue cauterization* in Section 4.4.

Photoablation

Removal of tissue without thermal damage is called photoablation. It was initially called *ablative photodecomposition* during studies at IBM in New York, during 1982, where highly energetic 193 nm laser radiation was used to etch parts of PET (polyethylene terepththalate) films [105][13]. The process of ejection of material through photoablation requires high laser irradiances - $10^7 - 10^8\,\mathrm{J\,cm^{-2}}$ - with typically nanosecond pulse lengths: photoablated regions generally show boundaries related to the spatial intensity profile of the beam, with depth of ejected material related to the energy of the pulse. During interaction, tissue is removed in a clean way, with no thermal effects in the vicinity of the affected region. This is mainly due to the dissociation of covalent bonds in the affected volume, which requires photons with very high energy. This is the main reason why UV radiation is preferred. It can be created either directly with e.g. excimer lasers($126\,\mathrm{nm} \geq \lambda \leq 351\,\mathrm{nm}$) or with infrared wavelengths through the generation of higher harmonics induced with nonlinear crystals [92].

The main model of photoablative processes is called the "blow-off" model, and is based on Equation 1.26. It further considers that photoablation will only take place as long as the fluence inside the tissue is larger than certain threshold fluence Φ_thr. A relation to the *etch depth* can then be written as:

$$\delta_{etch} = \frac{1}{\mu_a} \ln\left(\frac{\Phi_0}{\Phi_{thr}}\right) , \tag{1.46}$$

Φ_0 is the incident irradiance. During irradiation, the tissue expands, with dissociated molecules repulsing their partners and creating a somewhat gaseous product. The way this effect is pronounced, as well as the importance of mechanical stress during bond dissociation will be highly dependant on tissue composition, through the distribution of in the volume μ_a. Higher water content may, for example lead to larger plumes and more pronounced effects[14].

[13] The term "ablation" is actually defined in *Merriam Webster* as "surgical removal" or "loss of a part through vaporisation or melting".

[14] [92] provides more general information on photoablative effects. Further discussion on plumes, photoablation models and bubble formation, as well as a nice comparison between UV and IR wavelengths for photoablation can be found in [90].

Plasma-induced ablation, photodisruption

For very short pulses with a certain fixed fluence, the corresponding power densities can be so large that the main interaction process is not maintained by linear absorption. In fact, the very high energies delivered in focal volumes with µm to sub-µm scales can be so extreme as to generate electric breakdown of the material resulting in the formation of a microplasma, an ionized volume with very large free electron density. In order to free electrons from their covalent bonds, each pulse must be able to generate electric fields with values comparable to the average atomic or intramolecular Coulomb fields($10^6 - 10^7\,\mathrm{V\,cm^{-1}}$) [95]. There are different ways to generate optical breakdown, and a dependence on the field strengths, temporal pulse widths, and pulse repetition rates has been shown to influence the mechanisms behind free electron generation and plasma creation [106]. As an example, let us consider mode-locked laser which creates 800 nm, 150 fs pulses with a fluence of about $1\,\mathrm{W\,cm^{-2}}$ at the focal spot. The generated power density is in the order of $\sim 10^{12}\,\mathrm{J\,cm^{-2}}$, which creates very high electric fields:

$$E = \left(\frac{2\Phi_0}{c\epsilon_0}\right)^{1/2} \sim 10^{6}\,\mathrm{V\,cm^{-1}}. \tag{1.47}$$

Treating water as an amorphous semiconductor as proposed in [107], and taking into account the energy required for a transition from the molecular $1b^1$ orbital into the conduction band, a bandgap of $\Delta = 6.5$ eV should be considered. The interaction with strong oscillating fields nearby can influence the bandgap values, since the electron starts oscillating and so the ionization energy needs to be adapted[106]. Nonetheless, as a first approximation, we will restrict ourselves to the bandgap energy given above. Considering our example, each photon has an energy of about $hc/\lambda = 1.55$ eV. For fs pulses[15], one way to overcome the necessary energy gap would be if an electron could receive the energy of a minimum of 5 photons almost simultaneously. This is a nonlinear effect called *multiphoton ionization*, and it depends on the probability of such short interactions to happen coherently. Since the probability is directly dependant on the irradiance, it scales non-linearly with Φ_0^k, being k the number of absorbed photons [109].[16]

[15] Longer pulses (in the range) can promote ionization through *thermionic emission*, i.e. release of electrons due to thermal ionization [92, 95]. On the other hand, very short fs pulses irradiances of the order of $10^{13}\,\mathrm{W\,cm^{-2}}$ *tunneling ionization* may take place, since the very high electric fields can massively distort the potential barriers holding electrons in their orbits, allowing them to escape [106, 108].

[16] For a more in depth explanation, with corrections for the bandgap energy, together with comparisons of experimental data to simulations, the reader is welcome to look into [106, 109] and references therein.

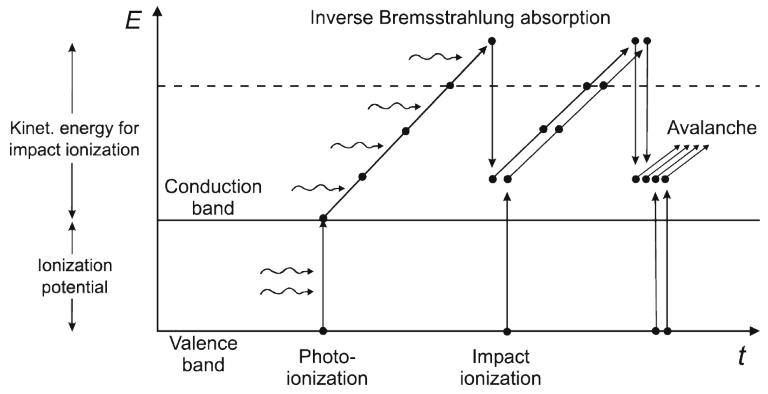

Figure 1.14: Schematics of the different mechanisms behind plasma formation. Plasma formation occurs at an interplay between photoionization, inverse Bremsstrahlung absorption, and impact ionization. After the first seed electrons are created, inverse Bremsstrahlung and impact ionization unleash an avalanche effect promoting a rapid growth in number of free electrons, and the creation of a plasma. Modified from [106].

After the first electrons are freed from their bonds, they may gain kinetic energy through absorption of further photons, thereby increasing their velocity. These rapid electrons may then collide with other bound electrons, freeing them from their bonds and allowing them to accelerate as well, a process which repeats itself in an avalanche effect also known as *inverse Bremsstrahlung*[17].

An interesting characteristic about optical breakdown is the increase in the absorption coefficient of the induced plasma, which allows the utilization of infrared lasers even in weakly absorbing samples. It is possible to model the plasma absorption coefficient $\mu_{a,pl}$ via estimation of the interaction of the motion of plasma electrons (mass m_e, charge e, density N and a mean collision rate ν_{ei}) and the inflicted electric field (oscillating with angular frequency ω) inside a tissue with refractive index n. Calculating the complex part of the samples' dielectric constant [92], yields the absorption coefficient:

$$\mu_{a,pl} = \frac{\nu_{ei}}{nc} \frac{\omega_{pl}^2}{\omega^2 - \nu_{ei}^2} \quad \text{with} \quad \omega_{pl} = \frac{Ne^2}{\epsilon_0 m_e}. \tag{1.48}$$

Equation 1.48 shows that the absorption coefficient is enhanced for longer wavelengths (i.e. smaller ω). Typically, the plasma should increase as long as inelastic collisions and free electron diffusion out of the focal volume can be overcome through rapid recurring sequence of inverse Bremsstrahlung absorption events. The plasma oscillations have highest amplitude when the

[17] Every change in velocity from a charged particle is bound to absorption or emission of energy. If an electron decelerates, for example, it emits a photon whose wavelength matches the corresponding lost kinetic energy. This radiation emission is known as Bremsstrahlung. The opposite - or *inverse* - refers then to the absorption of photons to promote a charged particle's acceleration.

plasma density-dependent eigenfrequency is in resonance with the field imposed in the sample, i.e. when $\omega_{pl} = \omega$:

$$N_{crit} = \frac{\epsilon_0 m_e}{e^2}\omega^2 \tag{1.49}$$

which, for 800 nm $\sim$ 10^{15} Hz, leads to maximum electron densities of up to a few 10^{20} cm^{-3}. After resonance, the plasma oscillation is decelerated due to the phase shift to the external field.

After optical breakdown onsets, the overall volume of free electron density broadens since incoming photons start being absorbed upstream of the laser focus, thus limiting the increase of energy density around the beam waist, an effect called *plasma shielding*. In fact, at large irradiances, optical breakdown starts even before the fs pulse reaches the focal beam waist, with both the its irradiance and propagation influenced by the generated plasma. This is also a shielding effect at the focal region, enlarging the overall breakdown region, albeit limiting the free electron density reached inside the breakdown volume [106]. This is an important effect, which allow the creation of highly localized plasma regions.

Although it is known that the plasma created by very short pulses should reach its so-called *permanent state* in about 100 ps or less, due to shielding effects [95], the same cannot be said about thermal increase. As discussed, thermal diffusion times are proportional to $1/\mu_a^2$. Since the absorption coefficient μ_a increases due to plasma creation is it expected that thermal diffusion times should decrease during plasma creation. However, in between pulses, the excess of heat must also diffuse through the tissue in order to dissipate, this time with longer diffusion times due to the lack of optical breakdown. The much longer expected times make it more probable that the next incoming pulse should already encounter a tissue volume at higher overall temperature than the previous one, meaning that an accumulative process occurs[18].

[18] For more information, please refer to [110] and references therein.

Chapter 2

Confocal multiview light-sheet microscopy

The behaviour of a collimated beam entering any tissue can be regarded as a photon distribution with two main components which originate from the ballistic and the scattered regimes. As discussed in Section 1.5, scattering inside tissues is characterized mainly by multiple scattering events in the forward direction [82, 88, 97]. It is expected, as light enters further into the tissue, that less photons will contribute to the ballistic regime, thus shifting the overall distribution towards diffusive scattering. Heuristic models based on transport theory lead to the definition of a transport mean free path length scale (Equation 1.42), which characterizes the strength of scattering effects as light propagates through a certain tissue depth L. The differentiated geometry of light-sheet microscopy setups in comparison to traditional widefield or confocal microscopes is not immune to this effect, as the different illumination and emission paths typically scatter along the tissue (*cf*. Section 1.5.3).

There are two main working directions towards increase in image quality for 3D datasets acquired with light-sheet microscopy. On the one hand, multiview imaging schemes aim at delivering an *in toto* 3D dataset of the sample. They traditionally rely on weighted fusion of the different views for the creation of the full 3D dataset where only the best quality parts of individual views are combined [4, 53, 55, 63]. Although effective, weighted fusion relies heavily on sample characteristics such as shape and scattering strength, and ultimately leads to blind loss of information from opposing side of detection (*cf*. Section 1.4.3). Still around similar proposal, multiview deconvolution-fusion algorithms not only fuse multiview datasets into one, but can also further improve contrast in multiview datasets through deconvolution calculations for each iterative step [111–113]. On the other hand, different ways to cre-

ate a confocal detection approach in single-view light-sheet setups decrease the amount of scattered light detection and lead to contrast enhancement of recorded images. These approaches attempt to reject only the part of the image which adds to blur and have no direct information [71,76,77,114]. Both these approaches led to important contributions in the field of light-sheet imaging. Nonetheless, a combination of both in order to facilitate the way 3D light-sheet imaging is performed, has so far not been demonstrated, and this is the main focus of the next sections.

In this chapter we briefly describe which are the main confocal methods that aim at the reduction of scattered light detection in light-sheet microscopes, and present our solution based on the combination of multiview imaging with electronic confocal slit detection. Confocal multiview light-sheet microscopy provides a new way of imaging which can increase acquisition speeds, minimize amount of recorded data and eliminate the need for specimen-specific fusion algorithms through the successful development and application of electronic confocal detection with multiview light-sheet imaging.

Confocal slit detection in two-lens light-sheet setups

There have been various different approaches towards the assessment and implementation of various confocal detection strategies in light-sheet microscopy. However, the great majority rely on scanned-beam illumination strategies[1] [67], reason why this will be from now on the primary illumination approach considered. Differently from traditional laser scanned confocal microscopy, where a pinhole placed in front of the camera promotes scattered light rejection, light sheet imaging requires a different geometry due to the decoupled illumination and detection optical paths. It imposes that the confocal mask should not block the illumination beam along its axis, otherwise the very fundamental idea of perpendicular illumination would be sabotaged. To this end a slit, instead of a circular mask, is be best suited.

The first approach towards light-sheet confocal detection aimed at the reduction of emitted light from fluorophores excited by the side lobes of Bessel beams [71] [2]. This solution relied on a parked illumination Bessel beam, and first required the sample to move up or down in a stepwise fashion, each step recording an image of the beams position [3]. Afterwards, a mask had to be

[1] So far only one work has tackled confocal detection with cylindrical lens illumination techniques. It relies on following an axially swept light-sheet, leading to increased overall resolution [68].

[2] More information on Bessel beams can be found in Section 1.4.1.

[3] "parked" means that while an image is taken the beam remains static at a certain position.

imposed to each image, the sum of all of them yielding the final image. This entire procedure was too slow for fast developmental processes, and needed many sample rotations for an *in toto* dataset, since only one illumination and one detection objectives were used. The proposition of mechanical masks followed suit [76], with the introduction of extra relay optics after the tube lens so that a physical mask could be placed. An additional pair of galvanometric mirrors also needed to be added so that through a descanning movement the mask could remain fixed in place. Although functional, this approach requires extra space for additional hardware in the detection path, being also rather inflexible to changes in mask sizes. A less hardware expensive solution was then put forth later on with the implementation of a mask on-chip for one illumination and one detection light-sheet systems [77,114]. These works focused mainly on the assessment of scattered light reduction, without any development towards multiview light-sheet setups. A schematic representation of an on-chip confocal detection can be seen in Figure 2.1.

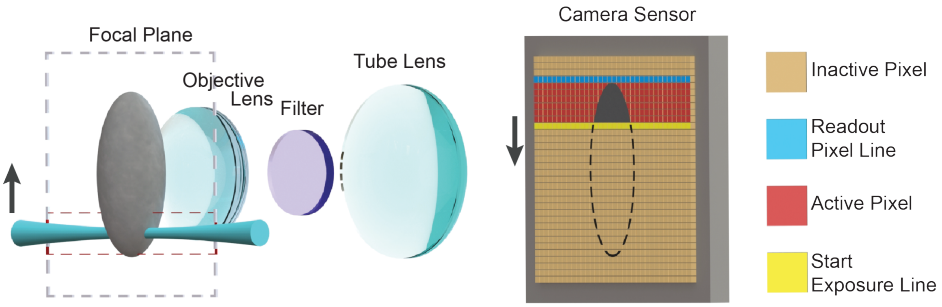

Figure 2.1: On-chip confocal detection. From left to right: Scanning beam movement is performed through voltage-controlled galvanometric mirrors which steer the beam over the focal plane. At the same time, a slit (with size equal to the number of active pixel lines, shown in red) moves synchronously with the image of the beam on the sensor (which is inverted due to the objective and tube lens needed for focusing the image on the camera). On the sensor, each pixel line at some point in time becomes active (yellow), acquires data (red) for the amount of time proportional to the slit width and the activation front velocity, and is read out (blue), becoming then inactive. More information on calibration and slit properties calculations in Section 2.1.

2.1 Electronic confocal slit detection for multiview setups

Exactly how can a confocal slit detection help multiview light-sheet image acquisition? One way to approach this question is by remembering that scattered contributions inside tissues typically increase with tissue depth. However, since most of the scattered light can be rejected through an electronic

mask similar to the one described above [77,114], the detected intensity should drop with the increase in tissue depth. Nonetheless, light propagating from the opposite direction - either through a second illumination path or a second camera - should then be able to compensate for any excessive loss of information. Schematics on scattering effects and dual camera confocal detection is shown in Figure 2.2.

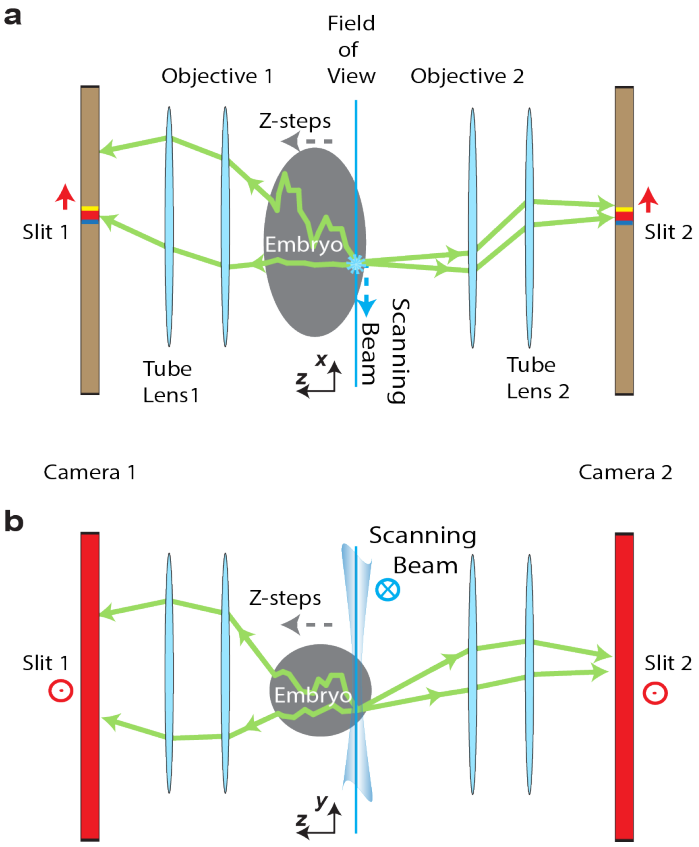

Figure 2.2: Effective scattering reduction with eCSD. All photons that are highly scattered along the x-component are completely discarded by the confocal slit, whereas the widefield detection detects these as increase in noise, leading to blurred images. Effects of scattering only in yz plane are captured by both confocal and widefield detection modi. Depending on the slit size, scattered photons with minor components in x direction might also be detected by both detection schemes.

It is important to reinforce the note that with this configuration the electronic confocal slit detection is effective only in the perpendicular direction to the illumination axis of each image. All scattered photons which arrive at the detector within a certain acceptance angle determined by the slit width will contribute to image degradation preferentially in the horizontal direction, as

exemplified in Figure 2.2.[4]

In order to test this working hypothesis, we first decided to record a full image 60 µm inside a *Drosophila melanogaster* embryo at stage 14, which expressed His2av-mCherry, a nuclear fluorescent marker. The image was acquired in a "synthetic" way: instead of recording entire images through a fast scan of each illumination beam [67], as is the normal illumination procedure in scanned beam light-sheet microscopy, the final image is constructed via a composition of parked beam images, a procedure analogous to a previous publication [71]. The main difference to the previous work is that instead of moving the sample we moved the beam and parked it in a different position for each step. 2200 evenly spaced parked beam images were acquired for each illumination arm separately, which allows us to slightly oversample the camera sensor - 2048 pixel lines. This is important, as later on both illumination beams need to be aligned on top of each other. After acquisitions for each illumination direction have been performed, we treated them in four different ways in order to generate the final image:

(i) Sequential widefield images (sigmoidal fused). The parked-beam images are added separately for each illumination direction. A sigmoidal weighting function is applied to each of the two images before summing both of them.

(ii) Simultaneous widefield images (direct sum). All images from both illumination directions are added to yield a single image.

(iii) Sequential eCSD images (sigmoidal fused). A confocal slit mask centered at the beam position with a fixed slit size is applied to each parked beam image before adding all images from the same illumination direction. The resulting two images are then combined by the same sigmoidal weighting function as in (i).

(iv) Simultaneous eCSD images (direct sum). As in (iii) the non-linear slit mask is applied to each beam position. Then all images of both illumination directions are added.

[4] More information on effects arising from confocal detection is provided in Appendix C

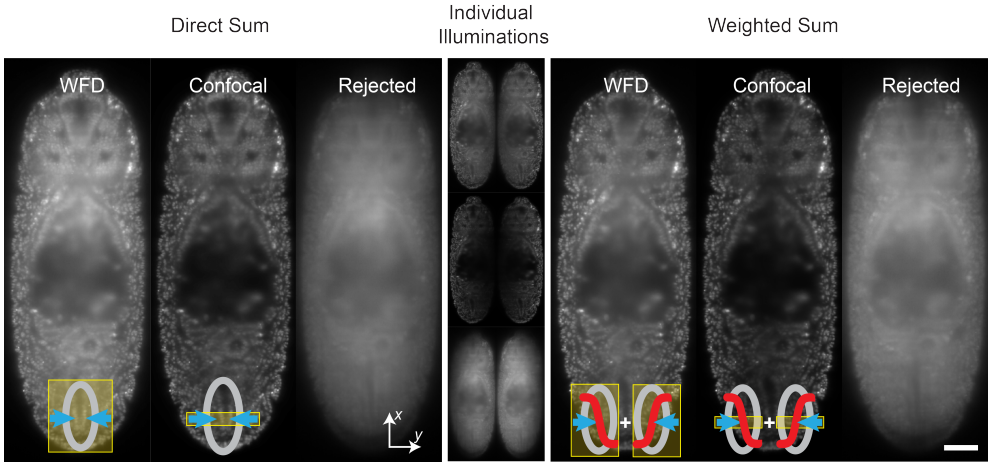

Figure 2.3: Synthetic slit mask comparisons. Computational analysis of parked beam images acquired 65 µm deep inside a *Drosophila melanogaster* embryo during dorsal closure. Accumulated parked beam positions from the two illumination directions were computationally combined either by direct addition (left, denoted direct sum) or by sigmoidal fusion (right, weighted sum). The individual side illumination is shown in between. Both direct and weighted sum fusion methods display computed widefield images (left), confocal images (middle), and the rejected (scattered) light (right). Direct and sigmoidal fusion yield similar image quality with confocal slit detection while direct fusion degrades the image under widefield detection. Scale bar: 50 µm.

Qualitative results can be seen in Figure 2.3. For the case of widefield images, calculated as in (ii), weighted sum through sigmoidal fusion of both illumination directions yields better image quality than simple image addition (i). Following the discussion above, this should be expected [63], reason why it has so far been the usual mode for dual illumination imaging. Additionally, images processed with the confocal mask show a strong decrease in signal on the far side from each illumination direction, also following our predictions. It is interesting to note that the decrease in signal resembles a "natural" weight function, and therefore it is unwise to fuse both images with sigmoidal fusion, as another decaying function will contribute to increased loss in signal in the center of the sample. This is why images directly summed (iv) with the confocal mask show a smoother intensity profile than the weighted fusion calculation (iii) and, at the same time, higher image quality than their widefield counterpart (ii). Moreover, our computational analysis allowed us to calculate the amount of light which is being rejected by the confocal mask. This could be done by subtracting the widefield form the masked images, the result images showing almost no structures, and mostly blur.

Additionally, the creation of the synthetic slit mask allowed us to define a metric analogous to the Airy units used in traditional confocal microscopy. Named *Beam-Slit unit*, it is defined as a dimensionless number which relates the slit size needed to encompass the image of the illumination beam at a cer-

tain distance from its focus, measured in pixels. Throughout the presented work, we have chosen the slit size to be 1.5 Beam-Slit units, and a brief discussion on the concept is presented in Appendix A. Comparative data on different slit sizes and their effect on image contrast is shown in Figure 2.8.

Dual camera electronic slit calibration and synchronization

Encouraged by the results presented with our synthetic slit experiment, we engaged in a collaboration with Hamamatsu Photonics Germany and Hamamatsu Photonics Japan in order to modify the latest generation of sCMOS sensor present in their cameras (Flash 4), so that a flexible electronic mask could be implemented on the sensor. Due to our collaboration with Hamamatsu Photonics now all the new Flash 4 cameras (called Flash 4 V2) have the possibility to acquire images in confocal slit modus called *light-sheet mode*, and are commercially available, having already proven its usability in scientific work from the light-sheet community [65, 115](Other camera manufacturers have recently released cameras with similar features (Andor Technology, Belfast, PCO Imaging)).

Modular control software

In comparison with the original MuVi-SPIM setup [4], in order to enable eCSD detection the only necessary change was to exchange cameras: everything else followed as a direct software upgrade. This could only be possible due to the implementation of a versatile modular control software, which allows us to add and remove devices around a common main framework. More information can be found in the methods section (Section 2.4).

Camera detection modes

The camera sensor is composed of two halves, and the exposure of the camera starts by triggering both of them simultaneously. During the normal mode of image acquisition, two activation fronts - also called rolling shutters - are created, propagating on each sensor half from the center outwards to the outer edges. This is known as the *widefield detection* (WFD). In *electronic confocal slit detection* (eCSD) the activation direction of the upper sensor half is inverted and the lower sensor starts its regular activation pattern directly after the upper sensor is fully activated. A comparison between the different modes of detection can be found in Figure 2.4.

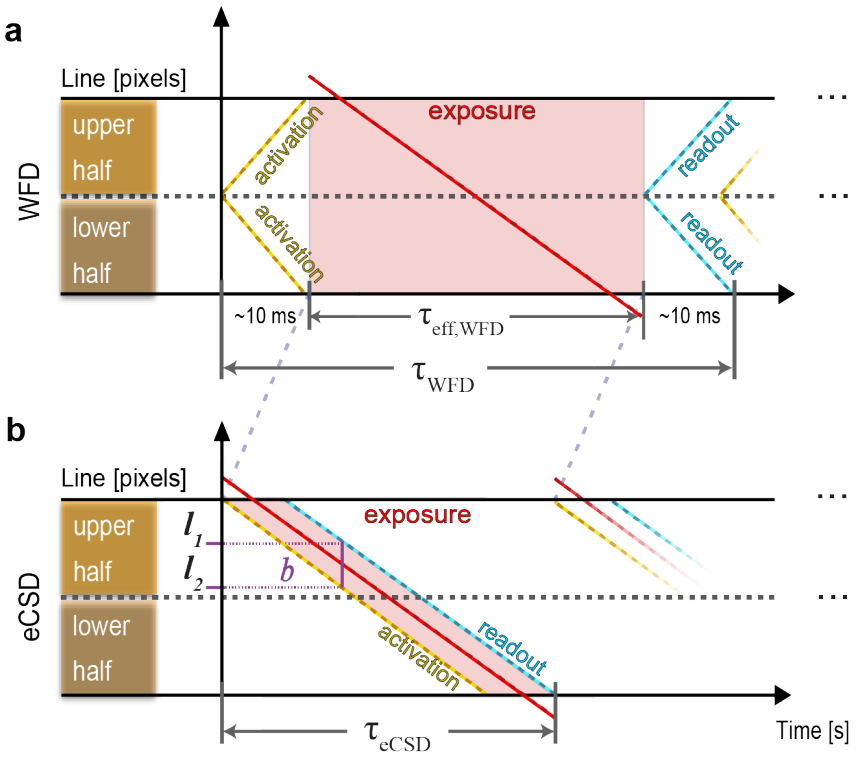

Figure 2.4: Modification of the sCMOS sensor for electronic confocal slit detection. a) In traditional widefield detection, activation of the pixels lines (yellow line) occur from the center outwards in a rolling shutter mode which needs 10 ms in total. The effective exposure time is the same for all lines (red box) as the illumination beam scans through the field of view (red line), and the readout of the pixel values (blue line) follows the activation pattern after an exposure time delay. Thus, the total time needed for WFD image acquisition is $\tau_{eff,WFD} + 20\,ms$. The movement of the illumination beam, in red, starts a beam radius above and below the sensor in order to have even illumination at the edges of the image. **b**) In eCSD, at any time point t during the exposure only a fraction of all sensor lines between l_1 and l_2 are active (illustrated by the purple line), and this is the characteristic electronic slit size b: the line at l_2 just starts the exposure at time t, while the line l_1 finished accumulating photons and is read out. The image exposure is showed as a red box lying whithin the activation and detection lines, and the laser beam movement is in the center throughout the whole scan.

The velocity of the activation front v_{act} in $[pixels \cdot s^{-1}]$ can be set in multiples of the minimal activation time of roughly 10 µs. This is a very important degree of freedom, as it allows to tune the velocity of the electronic slit to the the moving image of the scanning beam. It can *e.g.* be helpful for low light imaging situations where longer exposure times are needed without harming the biological specimen with too much laser power. It is also vital for proper calibration of eCSD for two opposing cameras, as will be discussed below. Each pixel line becomes active for a certain line-exposure τ_{line} [s] after which a direct read-out is performed: accumulated charges of the previously activated lines are discarded as a new line-exposure starts. τ_{line} can be specified freely, and its product with v_{act} provides the size of the confocal slit b [pixels]:

$$b = \tau_{line} \cdot v_{act} \tag{2.1}$$

Figure 2.4 presents two different detection modes, WFD and eCSD. In Figure 2.4a, the WFD timings needed for complete activation or readout of both sensor halves depend on the maximum rolling shutter speeds. Since each pixel line has a minimum dwell time of roughly 10 µs, around 10 ms are needed for each sensor half with 1024 pixels. For eCSD this means a minimum total exposure time t_{eCSD} of 20 ms (Figure 2.4b) which could only be compared to a widefield effective exposure $t_{eff,WFD}$ in the order of µs (note that $t_{eff,eCSD} \approx t_{eCSD}$, with $t_{eff,eCSD}$ the effective sample exposure time, more clearly depicted in Figure 2.5). This would require unusual amounts of laser power so that enough emitted photons could be detected with WFD on this time interval, leading to high photobleaching and phototoxicity effects, and being on the wrong direction of what light-sheet microscopy stands for[5]. As will be presented in Section 2.2, imaging with simultaneous illumination and eCSD is a factor two faster than WFD when $t_{eff,WFD} + 20\,ms \geq t_{eff,eCSD}$.

Calibration

Scanning of each illumination beam is governed by the actuation of one galvanometric mirror through pre-calculated voltage values. Voltage values determination is done with our modular microscope control software. Generally speaking, the input is a three-stage curve which provides the acceleration, linear speed and deceleration kinematics. The combined acceleration/deceleration phases usually take 10% of the total actuation time; during the time of the linear regime lies the exposure time for image acquisition, with the illumination laser on. In other words, the illumination beam needs to sweep over the field of view during the linear regime, in order to avoid any motion artifacts as shown in Figure 2.5.

Whereas calibration of one camera in respect to one illumination beam can be performed rather directly [77], the addition of another illumination and detection directions generates complications, as even the slightest differences in general optical alignment will generate different scan velocities for each illumination beam on each camera sensor. The only way to overcome this is by

[5] A third mode of operation, called *global reset*, has recently become available and allows the entire sensor to be activated almost simultaneously, thereby decreasing the overall exposure time needed for WFD imaging. However, the readout of pixels still happens in the same way as discussed in the text, needing $10\,ms$ to be completed.

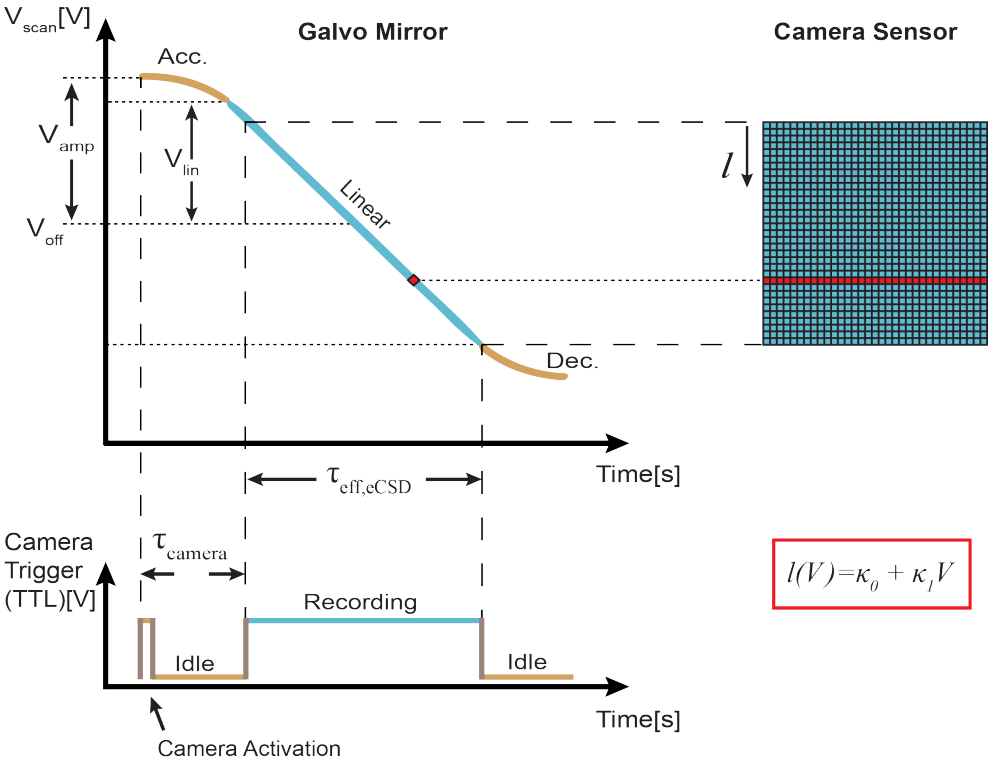

Figure 2.5: Implementation of the electronic confocal slit detection for light-sheet setups. Control scheme of the galvanometric mirror and mapping to camera coordinates. In between a brief acceleration (Acc.) and deceleration (Dec.) phases (yellow lines), the galvanometric mirror performs a linear scan of the illumination beam over the image (cyan line). The time needed for acceleration/deceleration and linear movement are not to scale. At the same the mirror has started moving, the camera is triggered active and awaits to start recording in idle state. Acquisition starts after the time delay τ_{camera}, which is needed so that the beam can be centered in the middle of the confocal slit. After the scan has finished, the galvanometric mirror decelerates and is rotated back to its initial position during the readout time of the camera (not shown) to prepare for the next image.

allowing the activation fronts from each camera to have an adjustable speed, as mentioned in the Section 2.1 above. If this is possible, then the calibration procedure allows us to find the necessary relations which will generate the mapping M_b of different voltages into different pixel line positions on the sensor.

$$M_b : (V_{amp}, V_{off}, \tau_{eCSD}) \longrightarrow (\tau_{line}, v_{act}, \tau_{camera}) \tag{2.2}$$

Here, V_{amp} and V_{off} are the amplitude and offset of the mirror motion in Volts, τ_{eCSD} [s] is the exposure time input for image acquisition. For the camera, τ_{line}, v_{act} are the line exposure and velocity of the activation front, as defined in Section 2.1, and τ_{camera} is a camera delay associated with the galvanometric mirrors' movement, so that the confocal slit only starts its virtual movement when the illumination beam has reached the first pixel line of the sensor. All three variables need to be carefully adjusted, as even the slightest

mismatch between both cameras field of views means a different absolute arrival time for the illumination beams. It is important to note that the mapping M_b depends on the definition of a slit size b as this is the only direct available parameter for the user.

Calibration procedure follows a stepwise protocol:

1. The sample chamber is filled with a fluorescent dye solution to visualize the illumination beam.

2. Only one illumination beam is used to calibrate one camera first.

3. The beam is parked at different positions on the sensor (at least two) by applying fixed voltages V - with $V_{amp} = 0$, and $V_{off} = V$ - to the scan-control electronics. Each time, the exact center position (line index) of the beam on the camera sensor l_i is determined automatically by processing the fluorescent image.

4. A regression method is used to relate scan-voltages to line coordinates on the sensor. Generally, first order regression (linear) has proven to be sufficient, yielding $l = \kappa_0 + \kappa_1 \cdot V$. The fitting parameters κ_0 [pixels] and κ_1 [pixelsV^{-1}] represent the center pixel line position of the illumination beam and the first order parameter fit. They reflect optical properties of the detection (magnification of the illumination and detection objective lens) and stay fixed, as long the optical setup remains unchanged.

5. κ_0 and κ_1 together with the slit size b completely determine the mapping M_b for the used detection arm.

6. This procedure is repeated for the second detection arm yielding specific fitting parameters κ_0' and κ_1' that determine the mapping M_b' for the second camera.

7. Finally, the other illumination beam is calibrated to overlap with the first illumination beam through adjustment of amplitude and offset settings.

More detailed calculations with an example of source code which can calculate the necessary parameters - $\tau_{line}, v_{act}, \tau_{camera}$ - is given in Appendix B. Although manual calibration was performed throughout this work, an automatization of this procedure is straightforward and is part of future updates on the software.

2.2 Streamlined data acquisition: direct fusion methods

Below we present the main results from the successful development and implementation of eCSD mode in MuVi-SPIM. The shift on effectively acquired photons towards the ballistic regime allows us to have a so-called *direct fusion*, which means summing different datasets directly, avoiding any specimen-specific fusion algorithms. In order to better assess image quality, evaluation of contrast increase in the considered images has been performed. Considering that there is no generally accepted solution for image contrast quantification, we have performed calculations on all relevant images utilizing three different methods: Michelson contrast (MC), standard deviation of energy-normalized histograms (σ_{En}) and the Local Band-Limited Contrast (from now on denominated BLC , with bands defined analogous to *useful contrast* measures [67,74,116]).

2.2.1 Simultaneous dual illumination

As motivated by our synthetic slit experiment, eCSD should allow simultaneous dual illumination. The natural decrease in signal from the lesser amount of ballistic photons coming from deeper areas of the tissue represents a natural weighting function which would otherwise need to be calculated and applied as a post-processing step. To finally test this after our implementation of eCSD on both detection cameras, we have imaged a single plane 50 µm deep inside a *Drosophila melanogaster* embryo expressing His2Av-RFP1 with widefield and eCSD detection.

In Figure 2.6, intensity line profiles along tissue depth for both illumination directions are shown as different profiles depending on the detection mode, with scattered photons contributing to an almost uniform intensity throughout the entire embryo. Contrast evaluation, normalized to the highest value, following the three different computed measure ($Michelson$, σ_{En} and BLC), yield similar results as observed by the naked eye, as can be seen in Figure 2.7. Although eCSD with weighted fused images has the highest contrast values for all measures, it is important to reinforce the effects introduced deeper inside the tissue through the implementation of an extra decaying function on top of eCSD detection itself. Furthermore, eCSD with direct fusion still yields higher contrast images than any WFD fusion method, allowing twice as fast image acquisition through dual simultaneous illumination.

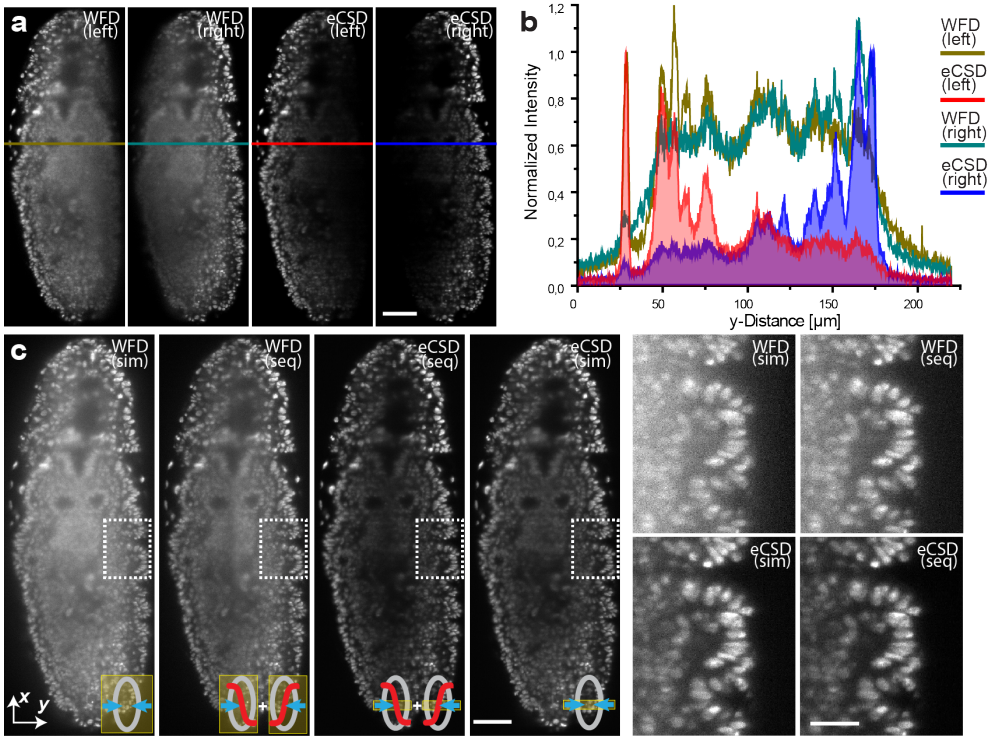

Figure 2.6: Simultaneous dual-sided illumination in confocal slit detection mode. (a) Left- and right-sided illuminations of a single (sagittal) plane 50 µm inside the *Drosophila* embryo expressing His2Av-RFP1 is shown for widefield and eCSD detection. The decrease in image quality away from the illumination side is clearly visible in widefield detection, while eCSD removes these blurred regions. **(b)** Intensity profiles across the embryo for indicated regions in (a). Intensity values close to and away from the illumination side are of equal magnitude for widefield detection (brown and green lines) preventing a direct fusion (addition) of images. eCSD profiles decay away from the illumination side as scattered photon are discarded. Please also note the removal of the scattered-photon haze outside the embryo. **(c)** eCSD detection with simultaneous illumination yields superior image quality compared to the established imaging procedure of acquiring two sequential widefield images followed by a sigmoidal fusion step. Simultaneous widefield and sigmoidal fused eCSD images are shown for completeness. Magnified views of all four imaging procedures are shown on the right. Scale bars: 50 µm in both (a) and (c) except inserts (30 µm). For all illumination and detection schemes optical (xy) sections 50 µm deep inside an embryo at germ band retraction stage were imaged.

All images have been acquired with a slit size of 1.5 Beam-Slit units. As mentioned in Section 2.1, slit sizes much above or below 1 Beam-Slit unit should yield lower contrast images. In order to exemplify this, we have acquired images inside a *Drosophila melanogaster* embryo with increasing slit size, and calculated the contrasts for each of them. The results can be seen in Figure 2.8.

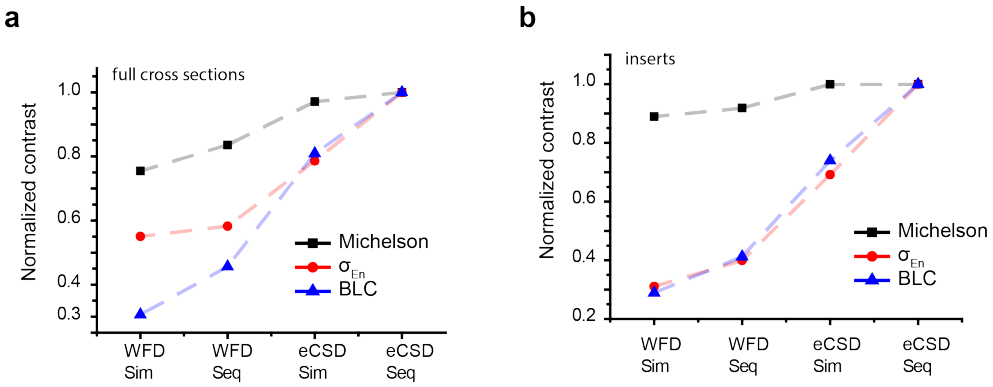

Figure 2.7: Contrast evaluations for simultaneous dual illumination with eCSD. (a) Contrast quantifications of the xy-cross section, and **(b)** of the xy-cross section shown in inserts (dashed squares) of Figure 2.6c. All dashed lines in the plot serve to guide the eye only.

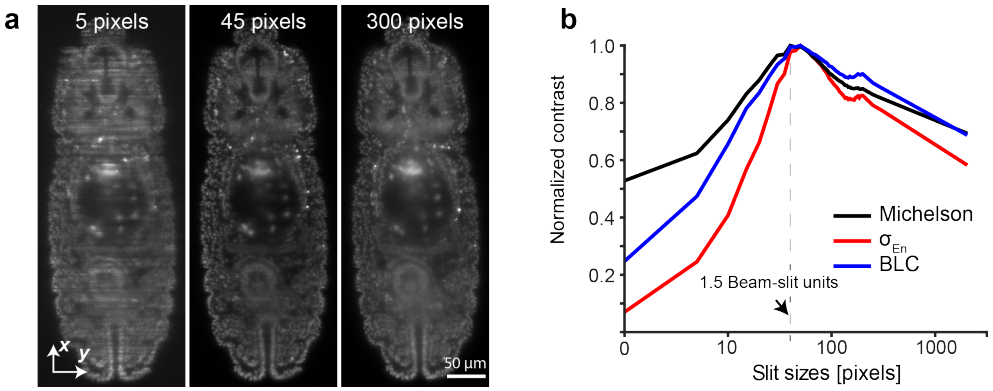

Figure 2.8: Automatic acquisition of a single plane inside a *Drosophila* embryo with 44 different slit sizes. (a) Selected representative images of the experiment. In all recordings a slit size of 1.5 Beam-Slit units was used. The total exposure time was 51 ms in all images, and they are scaled to the same maximum intensity to facilitate comparison of the dynamic range. **(b)** Contrast evaluation for all acquired images show a maximum for slit sizes around 40 pixels. This coincides with our choice of 1.5 times the Beam-Slit unit of the optical setup.

2.2.2 Direct fusion of opposing camera stacks

As discussed in Section 1.5, the optical geometric arrangement in light-sheet microscopy allows scattering to be considered as a distribution with two main contributions: illumination and emission scattering playing complementary roles on the determination of contrast for the final acquired image. Emitted photons which need to travel through more tissue will have a larger number of scattering events, thus shifting emitted photon distribution towards scattered light contributions. On the camera, this means that less photons will be acquired by the electronic slit, leading to an overall decrease in signal along the stack direction (defined as z). The main idea about multiview light-sheet microscopy, however, is that an image acquired deep inside the tissue from a particular view could be more easily accessible from the opposite view (*cf*

Section 1.4.3). This means that opposite views can complement the low intensity, deep tissue images from original views in a natural manner. As can be seen in Figure 2.9, this is the observed case.

With eCSD it is possible to directly sum opposing stacks into one full multiview dataset, without the need for any specimen specific fusion. Contrast calculations performed on zy cross-sections are presented in Figure 2.10 and show that in the case of drosophila, the utilization of 1.5 Beam-Slit units allows direct addition of opposing camera stacks to yield higher contrast values at no cost in computational power.

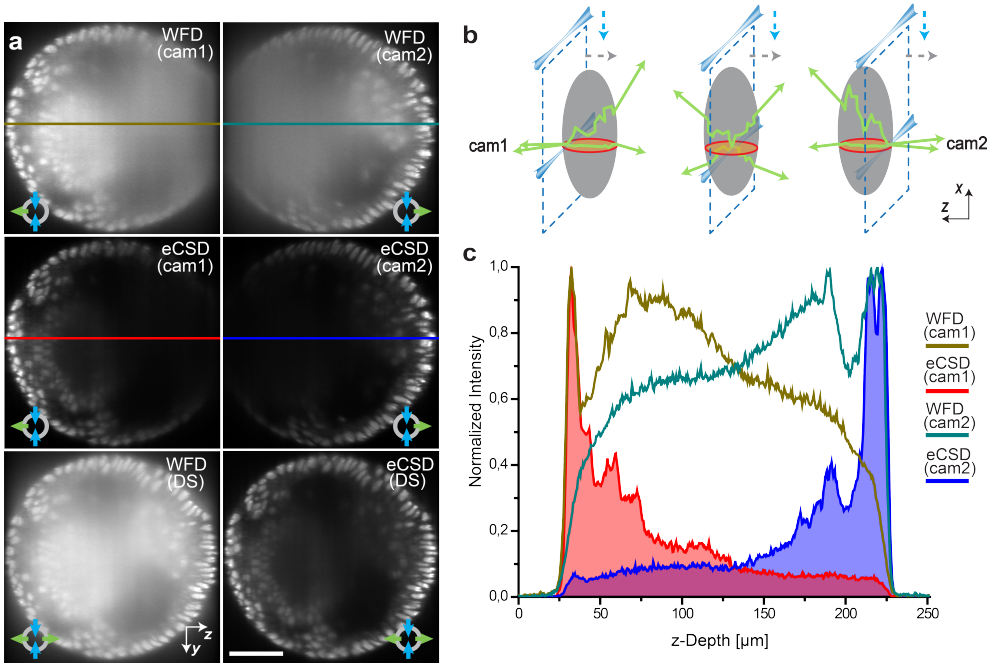

Figure 2.9: Confocal slit detection enables direct fusion of opposing views. (a) Transverse planes of 3D data stacks halfway between the anterior and posterior pole of an embryo expressing His2Av-mCherry (see red circle in (b)) are shown for widefield and eCSD detection. Top two rows show individual stacks acquired by the two opposing cameras in widefield and eCSD mode. Bottom row compares simultaneous widefield and eCSD images. Camera 1 and Camera 2 are orientated to the left and to the right, respectively. **(b)** Similar to the illumination light, also the emitted light is subject to scattering. The effect of scattering increases the deeper the image plane lies inside the embryo (dashed blue lines illustrate the light-sheet plane). The red circle indicates the transverse plane depicted in (a). **(c)** Comparison of intensity profile for widefield and eCSD 3D data stacks. Widefield detection collects a significant amount of photons from the far-side of the embryo (around 50%), which yields a structure-less blurred image (top row in (a)). Direct addition of the data thus results in a reduction of the signal-to-noise ratio (bottom row left panel in (a)). In contrast, eCSD rejects the majority of emitted photons from the far side, which enables a direct fusion (addition) of the two opposing camera stacks. All scale bars are 50 µm and all images are averages of 4 planes around the center of the embryo.

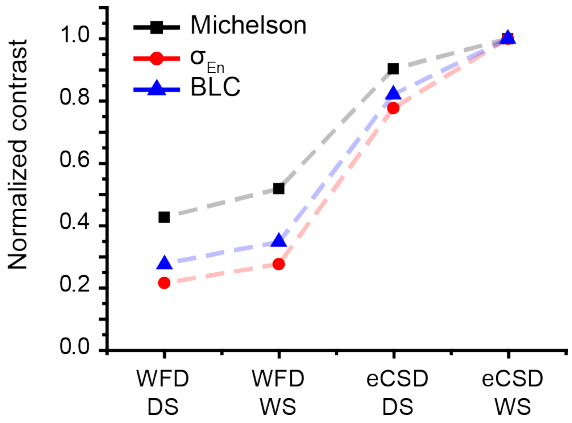

Figure 2.10: Contrast quantifications of the zy-cross section shown in WFD (direct sum) and eCSD (direct sum) subpanels of Figure 2.9a.

2.2.3 Simplified multiview-deconvolution fusion

Multiview light-sheet microscopy with eCSD has by now been shown to facilitate fusion of opposing illumination/detection in comparison to weighted fusion methods. Yet another way to fuse multiview datasets takes advantage of deconvolution steps in order to improve contrast through spatial reassignment of photon intensities [42,111,117]. Called *multiview-deconvolution fusion*, these algorithms increase data quality by taking into account the respective PSF's of all the different views obtained through multiview imaging: it relies on successive Richardson-Lucy iterations for all views in order to combine them into one ful 3D dataset. This can in turn can be quite computationally expensive. Our results with direct fusion on the other hand suggest a more streamlined pipeline for data processing: opposing cameras, dual illumination datasets acquired with eCSD are first directly fused and the resulting dataset is processed by a classical deconvolution scheme - as illustrated in Figure 2.11a. We compare in Figure 2.11 multiview-deconvolution fusion results with deconvolved direct-fused confocal 3D datasets for WFD and eCSD respectively. For further comparison, images of sigmoid-fused WFD and direct-fused eCSD are shown. As a result, eCSD images which were first direct-fused and then deconvolved present contrast values similar to their multiview-deconvolved fused counterpart, and both of the datasets show the expected higher contrast values than any of the WFD results, as seen in Figure 2.8. Overall, these results allow eCSD direct-fusion deconvolution to reduce both the memory requirements and the computational load of the Richardson-Lucy steps by a factor of four.

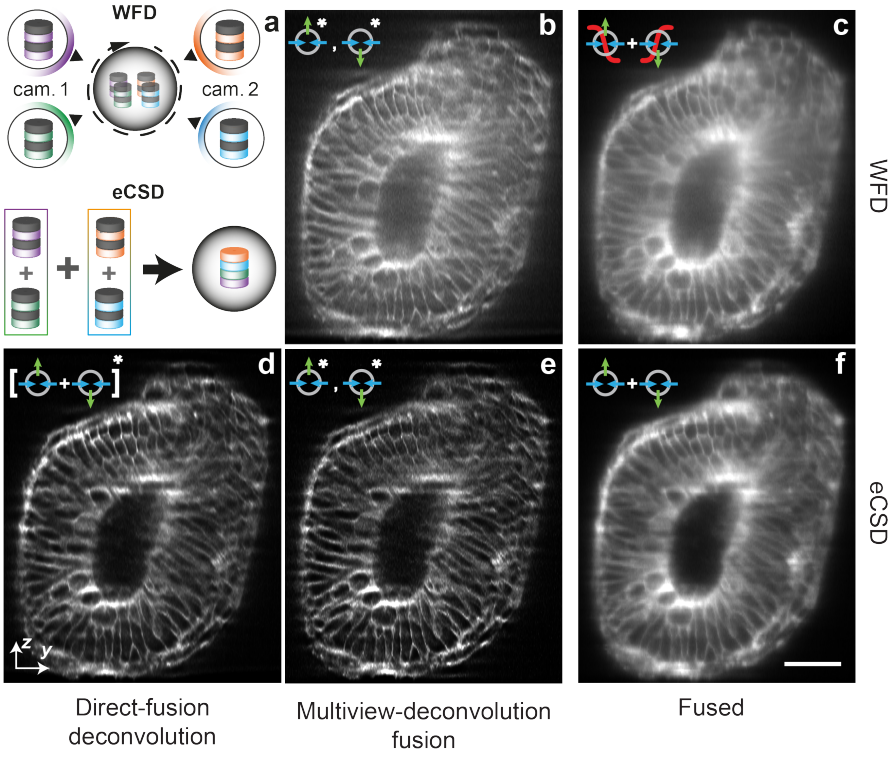

Figure 2.11: Comparison of multiview-deconvolution fusion and eCSD facilitated direct-fusion. (a) Illustration of multiview-deconvolution fusion pipeline (top) and optimized direct-fusion deconvolution data processing for eCSD datasets. In multiview-deconvolution fusion all views (in our case 4) enter the deconvolution pipeline and are iteratively combined to a single high quality dataset. In contrast the eCSD pipeline first fuses the four views to a single dataset, which is then deconvolved by a classical (single view) deconvolution scheme. **(b)** Widefield multiview-deconvolution fused dataset. **(c)** Sigmoidal-fused widefield datasets without deconvolution post-processing. **(d)** Direct-fused eCSD datasets followed by single view deconvolution. (e) Multiview-deconvolution fusion of eCSD datasets. **(f)** Direct-fused eCSD datasets without deconvolution post-processing. All subpanels display a cross section YZ-plane around 81 µm deep from the anterior side of the membrane data (mouse embryo) presented in Figure 2.14. The Fiji multiview deconvolution plugin [111] was used for dataset shown in (b,d,e). Please note that for the direct-fused dataset in (d) the Fiji plugin was used as a single view deconvolution algorithm. Additionally, Figure 2.13 shows a comparison between the multiview-deconvolution fusion and a single deconvolution commercial software. Scale bar is 50 µm.

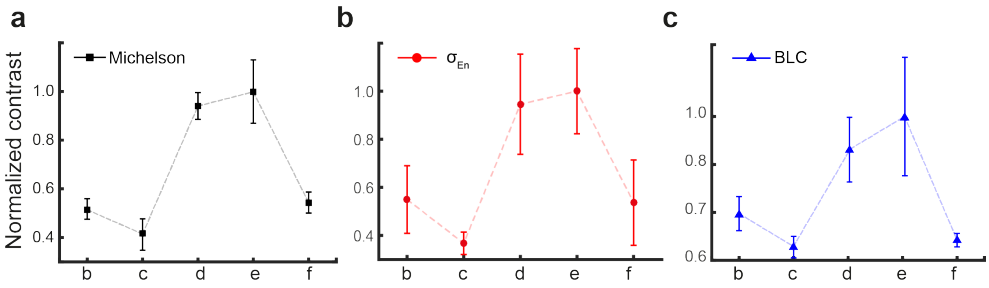

Figure 2.12: Contrast quantification of multiview fusion approaches in Figure 2.11. The graphs display image quantification of the 3D dataset shown in Figure 5 (main text) for **(a)** Michelson contrast[116], **(b)** energy-normalized histograms[67] (σ_{En}), and **(c)** the Local Band-Limited Contrast5 (BLC, with bands defined analogous to Useful Contrast measures[74]) measures. We evaluated the measures in regions for 17 consecutive planes to estimate the variability across each 3D dataset. The plots show mean values and variances of each measure for widefield (sigmoidal fusion and multiview-deconvolution fusion) and confocal images (direct-fusion with deconvolution and multiview-deconvolution fusion, direct-fusion without deconvolution). All curves were scaled taking into account the highest mean value. Multiview-deconvolution fusion and direct-fusion with deconvolution post-processing yield similar measures exceeding the image quality of widefield images.

This fact is reinforced by the data shown in Figure 2.13, which presents a comparison between multiview-deconvolution fusion and a traditional deconvolution pipeline with the same eCSD direct-fused 3D dataset:

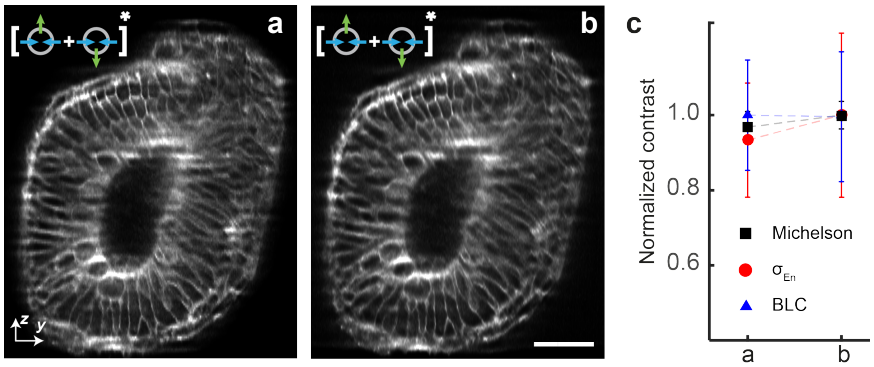

Figure 2.13: Comparison between multiview fusion deconvolution and single deconvolution post-processing.(a,b) Our direct-fusion approach is also compatible with 'normal' (single view) deconvolution methods. Here we compare direct-fused eCSD images processed after fusion with a commercial deconvolution software package (Huygens, SVI Netherlands) in (a) with Figure 2.11d repeated in (b). **(c)** The image quality quantification in reflects that both methods yield very similar results. Scale bar is 50 µm.

No relevant contrast differences are observed for either methods. This not only reinforces the simplification of this post-processing step through direct-fusion of multiview datasets but also increases the flexibility of performing deconvolution on multiview datasets, allowing parts of the microscopy community to readily use their preferred deconvolution software for multiview light-sheet datasets.

2.3 On robustness of eCSD for different specimens

Multiview light-sheet microscopy with eCSD and direct fusion shows itself to be robust for a range of different markers and samples, and has so far been the default mode of acquisition in our MuVi-SPIM for all recordings, since its first implementation. We have evaluated eCSD for multiview imaging for a multitude of different embryos and markers, including mouse, zebrafish, ascidians, plants and starfish. Representative images are shown in Figure 2.14 and Fig. 2.15. It is important to note that for all these samples a slit size value of 1.5 Beam-Slit units was adopted, suggesting that this improved acquisition method is robust enough for a wide range of imaging experiments.

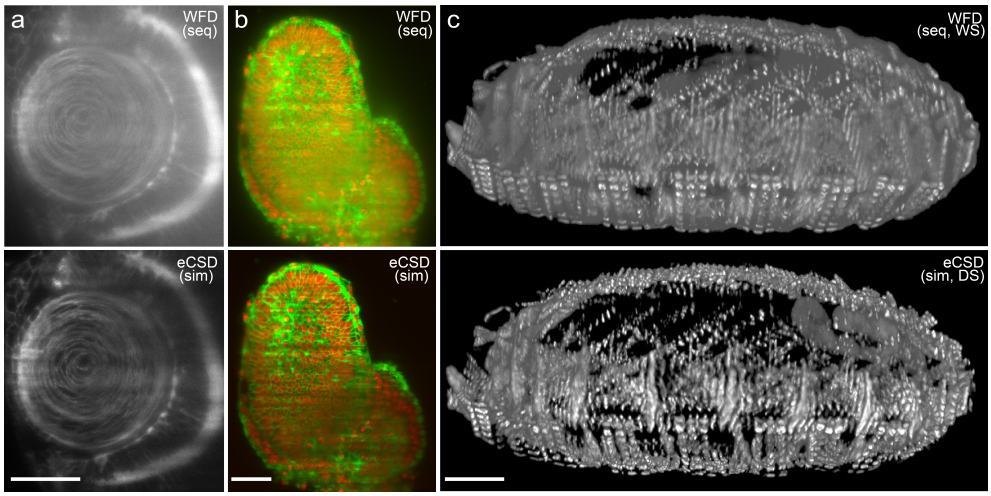

Figure 2.14: eCSD multiview light-sheet images with direct data fusion. (a-c) Examples of contrast enhancement with sequential or simultaneous illumination, direct or weighted sum by confocal versus widefield detection for different organisms and biological markers: **(a)** Zebrafish eye lens region, (Cry::CFP), **(b)** 6.5 dpf mouse embryo (R26-H2B-mCherry x mG), **(c)** 3D projections of muscle related Kettin-mCherry labeled *Drosophila* (14hrs AEL). Scale bars for all subpanels are: 30 µm in (a) and 50 µm in (b,c) and the electronic slit size was fixed to 1.5 Beam-Slit units for all eCSD images. Note that this corresponds to a slit size of 30-60 pixels on the camera sensor depending on the illumination and detection optical setup for each experiment. The illumination beam diameter was measured before the imaging to obtain the Beam-Slit size of 1 for the optical setup.

However, what does robustness really mean? It should not be mixed with the erroneous idea that eCSD should become the *only* necessary detection mode: this is not the full picture. One of the strengths of the implementation of eCSD, apart from enabling the direct fusion methods mentioned in the previous sections, is its flexibility, permitting the user to tune the degree of confocality between values of less than 1 Beam-Slit unit to full widefield detection freely, a procedure completely analogous to tuning the size of the pinhole in traditional confocal microscopy. For example, confocality in light-sheet microscopy will also depend on fluorophore intensities: very intense

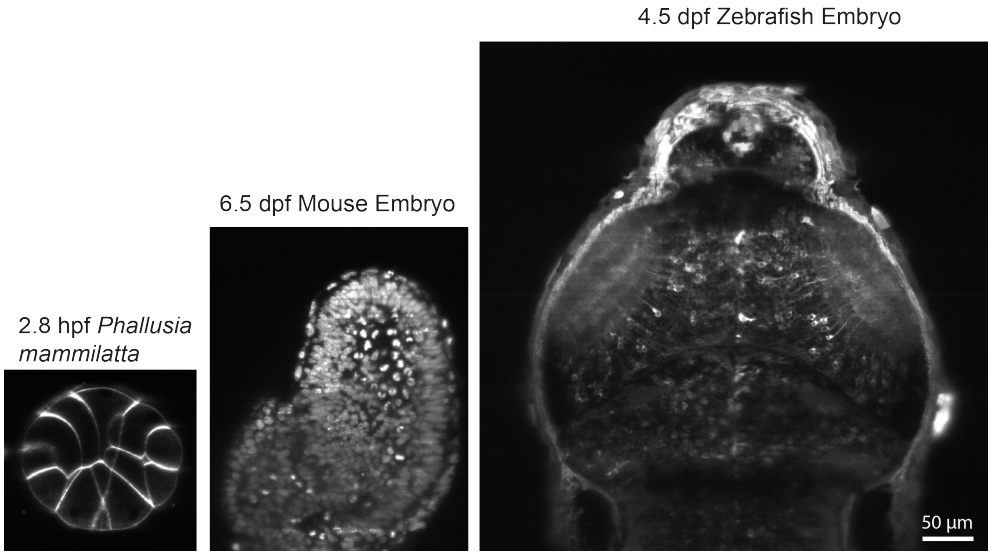

Figure 2.15: Imaging specimen of different sizes. eCSD allows imaging of different samples which can range on different sizes and here we exemplify images of Phallusia Mammilata embryo (140 µm), a mouse embryo (230 µm) and a 4,5dpf Zebrafish embryo brain (500 µm). All imaged with a fixed slit-size of 1.5 Beam-Slit units.

fluorophores will allow the usage of slit widths smaller than the chosen width of 1.5 Beam-Slit units, since more photons with ballistic behaviour can be collected. Such high emission values are however typical for experiments with fixed samples. The system is also still able to record signal even in particular situations where the distribution of scattered photons is much higher than the ballistic regime. As one extreme example, let us consider the development of *Drosophila* embryos at very early mitotic cycles (*mc*, with mc < 7), and that the positional information of the nuclei needs to be known. Since at these stages the nuclei are located at more than $35\,\mu m$ deep inside the tissue, away from the vitelline membrane, scattered light plays such a strong role that to discard it would mean to lose important information, as the signal of ballistic photons alone start to mix with the base camera noise levels. As will be shown in Section 4.2.2 of Chapter 4, for these recordings no eCSD has been used.

The main purpose of multiview confocal light-sheet microscopy is to provide a similar level of acquisition flexibility found in traditional confocal microscopy and to facilitate the way multiview light-sheet data can be recorded and processed into 3D datasets. It is created to function as an upgrade on any existing multiview light-sheet system, without interfering with any previous imaging capabilities from the microscope. We have observed that with Beam-Slit units of around 1 it is possible to not only increase recordings speed, but also to perform direct fusion methods which are less costly both on resources and processing methodology.

2.4 Materials and methods

Below we present materials and methods utilized for this chapter. It is based on the resulting article published in Nature Communications from 25 of November [78].

Light-sheet microscope setup Here we briefly summarize the key components of our confocal MuVi-SPIM setup. As described previously[4], The microscope consists of two opposing illumination and two opposing detection arms. All experiments had the following objective configuration: two Nikon 10x NA 0.3 water-dipping objective for illumination and two Nikon 25x NA 1.1 water-dipping objective lenses for detection. The main modifications compared to the previously described MuVi-SPIM setup are a 50:50 laser beam splitter (non-polarized) to direct the laser light to both illumination objectives, tube lenses (Nikon 200mm and 300mm) to yield an effective magnification of 25x or 37.5x depending on the size of the sample. Additionally, the sample fluorescence was imaged onto two custom modified Hamamatsu Flash 4 V1 cameras enabling confocal slit detection. A custom written script - which utilizes the equations shown in Appendix C - calculates necessary parameters for the slit calibration. For all sample imaging we used a theoretical Beam-Slit unit based on the $1/e^2$ size of the illumination beam.

Hardware control Electronic confocal slit detection requires precise timing and position control of cameras, lasers and galvanometric mirrors to ensure alignment of the illumination beam with the active area of the camera. As outlined above, we estimated the timing precision to be in the range of a few microseconds. For our optical setup, a galvanometric mirror amplitude of 1V is sufficient to scan across the entire field-of-view of the camera (532 µm). A minimal slit size of 4 pixels thus yields a required precision in galvanometric mirror control voltage of 1V*4/2048 = 2 mV. This can be achieved with 16 bit precision DAC. We used a custom written LabView (National Instruments) control software for synchronization of timings across all microscope devices. All trigger and analog voltage traces are calculated by a field programmable gate array (FPGA, National Instrument NI PCIe-7842R with a Virtex-5 FPGA) that ensures precise timing in the sub-µs range (40 MHz clock frequency). Following our collaboration with Hamamatsu Photonics, Japan, electronic confocal slit detection, also called ”light-sheet mode”, has been made available with version 2 (V2) release of the Hamamatsu Flash 4 camera. Other camera manufacturers have recently released cameras with similar feaures (Andor

Technology, UK and PCO Imaging, Germany).

Electronic confocal slit detection could easily be implemented in our microscope through the first implementation of a modular microscope control software, realized between 2012 and 2013, being part of this thesis, and done with the support of Bálint Bálasz and Dr. Nils Norlin. The software used LabView (National Instruments) as a programming language, and it allowed the user to flexibly choose which modules (called *devices*) the microscope has, each of which corresponding to a certain hardware part (i.e. lasers, cameras, stages...). Each device then could communicate with the main control through internet protocols using pre-defined metadata. The flexibility and applicability of this software became apparent when the software was adapted into two different light-sheet microscopes, each developed for completely different research topics: live imaging of pre-implantation mouse embryos [56], and super-resolution light-sheet microscopy with reversibly switchable proteins [61]. Further improvements of this software have been commercially developed by others (Luxendo GmbH).

Deconvolution Mutliview fusion-deconvolution was performed with the Fiji Multiview Reconstruction plugin, (Fiji version 1.50b). For Figure 2.13, deconvolution was done with Huygens Pro with an under development SPIM module, Scientific Volume Imaging B.V, version 15.05.1p1 64b. All calculations were performed with the theoretical PSF of the optical setup.

Zebrafish Embryos were collected after fertilization and incubated at 28°C. The temperature during imaging was kept constant at 23°C. Embryos were mounted in an agarose gel (Sigma-Aldrich) inside a glass micropipette (Brand 100 µL) and a short cylinder of agarose containing the sample was then pushed out and placed in the microscope.

Drosophila Embryos were collected on apple juice agar plates and then dechorionated for 1 min in a fresh 50% bleach solution. Embryos were mounted in a 0.8% GelRite gel (Sigma-Aldrich, G1910) inside a shortened glass micropipette (Brand 100 µL). A short segment of the gel cylinder containing the sample was pushed out of the micropipette and the pipette inserted into the microscope.

Mouse All animal works were performed in the animal facility at the European Molecular Biology Laboratory, according to the permission by the institutional veterinarian overseeing the operation (ARC number TH11 00 11). The

animal facility is operating according to international animal welfare rules (Federation for Laboratory Animal Science Associations guidelines and recommendations). Mouse embryos were isolated 6.5 days after plug formation by natural matings between R26-H2B-mCherry [118] and mG [119]. Embryos were dissected from the uterus and cultured in phenol red-free Dulbecco's modified Eagle's medium (Gibco, 11880-028) supplemented with 10% fetal bovine serum (PAA laboratories, A15-080), in 5% CO2 atmosphere at 37°C and within 2âĂĽh imaged after mounting them in ultra-low melt agarose (StarLab GmbH, Germany) inside a glass micropipette similarly to zebrafish embryos.

Mouse embryos were isolated 6.5 days after plug formation by natural matings between R26-H2B-mCherry21 and mG (ref. 22). Embryos were dissected from the uterus and cultured in phenol red-free Dulbecco's modified Eagle's medium (Gibco, 11880-028) supplemented with 10

Ascidians Adult *Phallusia mammillata* were acquired from the Roscoff Marine Biological Station (France). Embryo handling was done as described in Sardet et al [120]. The membranes were marked with FM464 (6 µм). The embryo was imaged in artificial seawater at a temperature of 18°C and mounted in the well of a 0.8% GelRite (Sigma-Aldrich, G1910) plug.

Chapter 3

Deep tissue imaging with infrared fluorophores

3.1 Deep tissue imaging strategies

While fluorescent labelling of proteins inside tissues has revolutionized the way microscopy records natures' machinery, the possibility to image deep inside tissues without the need to physically cut through the different layers remains a complicated challenge. There are two main different aspects which hinder deep tissue imaging: light scattering (e.g. due to the presence of proteins which locally change in refractive index) and absorption (notably due to lipids) through different tissue components. Out of the many different approaches set to overcome these challenges, tissue clearing, for example, aims at minimizing the scattering effects of proteins and lipid light absorption via chemically changing the tissues' properties. Clearing methods typically rely on lengthy protocols which can take up to several days; the result, however, is a tissue with a new average refractive index which can better match the optical demands of the embedding medium as well as the optics used for imaging, whilst maintaining a high degree of structure preservation. As a consequence, this can only be done in fixed samples, which limits the range of possible applications. Although the first approaches towards tissue clearing have been known for many years in the medical field [121, 122], the combination with fluorescence microscopy, notably light-sheet has happened only recently [123], and since then numerous other clearing methods were developed [115, 124–127].

A more gentle approach relies on multiphoton excitation microscopy: it relies on allowing a fluorescence molecule to simultaneously absorb a certain number of photons whose combined energy overcomes the molecule's

excitation energy gap. Since for each photon $E = hc/\lambda$, the excitation of typical fluorophores in the visible range requires illumination light with longer wavelengths. Considering mainly two- or three-photon absorption processes [12,128], this wavelength must be in the infrared region. This is advantageous, since – *cf*. Section 1.5 – longer wavelengths typically means less tissue absorption, and certainly less scattering, which means longer penetration depths. As the probability of multiphoton absorption is proportional to the intensity through: $P \propto I^k$, with k being the number of photons needed to be absorbed, high photon densities must be created in the region of interest. This is usually done by focusing high power pulsed infrared lasers in small volumes. On the other hand, the intensity decays from the focus with $1/r^{2k}$, meaning that the effective excitation volume is very small, and as the volume gets smaller, there is a smaller number of fluorophores which can be excited. This leads to the necessity for long exposure times, so that enough signal can be detected, which hinders fast acquisition of rapid biological events. In addition, this technique still depends on the emission of light in the visible range, which scatters at much higher rates than the illumination, and generates deep tissue images with lower quality.

Yet another way to minimize scattering effects and therefore shift the distribution of illumination/emitted photons towards the ballistic regime is to perform single photon excitation at longer wavelengths. It not only allows for faster acquisition rates in comparison to two-photon imaging, but also allows *in vivo* recordings at large tissue depths. However, excitation and emission wavelengths must be chosen wisely: while scattering typically decreases with longer wavelengths, overall tissue absorption is highly dependent on its constituents, and shows therefore a strong spectral dependence (*cf* Section 1.5.1, and exemplified in Figure 1.5.1). One possible spectral window with minimal absorption effects lies whithin the far-red to infrared spectral range of 650-900 nm [90, 95, 129]. While for microscopists less scattering and absorption effects lead to higher penetration depths and signal to noise ratios deeper inside tissues, for the living sample this in turn means lesser phototoxic effects in respect to higher light dosages over long periods of time.

This chapter is devoted to presenting and discussing preliminary results for *in vivo* and *in toto* single-photon excitation microscopy of embryos with infrared fluorophores. Although the core of the results presented can be applied with any fluorescent microscopy technique, the coupling of multiview light-sheet microscopy with infrared labelling techniques provide data also important for the evaluation of the marker throughout development, everywhere in the embryo.

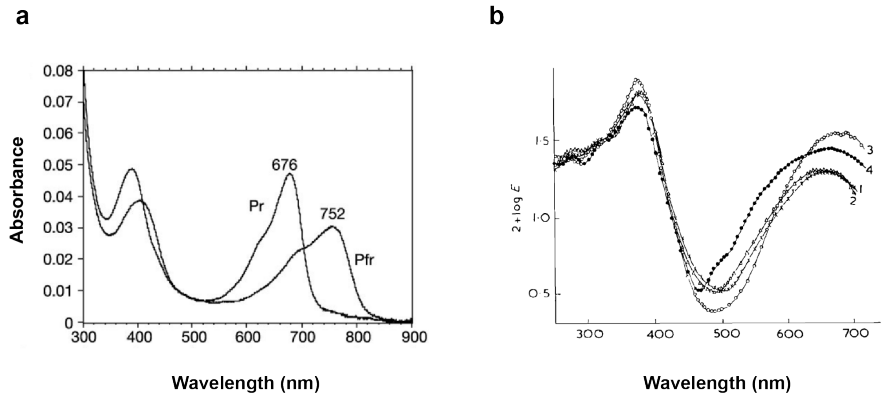

Figure 3.1: Optical absorption of phytochrome and biliverdin. (a) Absorption spectra of the two different forms of *Bradyrhizobium* bacteriophytochrome reconstituted with biliverdin, *in vitro*. Pr corresponds to the inactive and Pfr to the active forms of the molecule. **(b)** Absorption spectra in logarithmic scale of pure biliverdin in: 1)methanol ($MeOH$); 2)chloroform ($CHCL_3$), 3)methanolic chloridric acid ($MeOH + HCl$) and 4)methanolic acid after the solution had been kept for 2 hours under sunlight. Modified from [131,132], respectively.

3.2 Phytochrome-based fluorophores

Out of the many fluorophores which emit in the far red, the creation of fluorophores based on phytochromes allowed fluorescence microscopy for the first time the acquisition of images in the 700 nm spectral region of live samples, opening a new road towards single photon excitation infrared fluorescence imaging [7]. Phytochromes are composed by a protein and a bilin-based chromophore (usually biliverdin). Biliverdin is a subproduct of heme degradation path through heme oxygenase (HO1). In many insects, heme is found to be a vital nutrient for their embryonic development; however, when found in high concentrations, it can lead to cell damage through oxydative reactions [130]. Phytochromes on the other hand can be found as infrared photoreceptors common to plants, responsible e.g. for flowering (photoperiodism) and maintenance of the circadian rythm. This is achieved as the associated phytochrome undergoes a periodic shift between an active and an inactive form, which confers them a cyclic behaviour. Phytochromes can be also observed in some bacteria, performing the control of their photosynthetic system. In the active form phytochromes usually show strong absorption between 650-800 nm [131], which matches well with the absorption spectrum of pure biliverdin as can be seen in Figure 3.1. Since naturally occurring phytochromes are not bright enough to be directly used as fluorescent markers, several rounds of mutations and biochemical engineering were necessary so that the first candidates could be created.

The first important step towards the creation of versatile infrared fluorophores based on phytochromes was published in 2008 and the fluorescent protein was called IFP1.4 [7]. Although it was reported to be useful for *in vivo* imaging [7], its low binding affinity to biliverdin lead to low effective brightness which could only be overcome through addition of exogenous biliverdin in the tissue. The next generation that followed - iRFP - aimed at increasing signal to noise, photostability and brightness. iRFP also appeared to be activated through physiological levels of endogenous biliverdin, making it the first good candidate for non-invasive *in vivo* imaging [34]. Since then many other variants have been created [31], especially targeting ways to perform multicolor imaging.

Fluorescent proteins should function as a marker of the protein of interest in the least invasive way, not perturbing their natural stoichiometry, otherwise artifacts non-related with the focus of the experiment can take place. As one example, if the labelled protein is a signalling receptor, fluorophore multimerization can generate protein oligomerization leading to artifacts in signalling activity [133]. Also, normal formation of complexes with the labelled proteins can be hampered, or even induced towards unusual protein partners, which may also in turn lead to a cascade of misleading events. In order to prevent this, stable monomeric version of fluorophores are usually preferred over multimeric ones [134, 135]. In the case of infrared fluorophores, whereas IFP1.4 was found to be monomeric, iRFP was reported to be a dimer. Following this reasoning, a new improved version of the monomeric IFP1.4 was then developed, with improved brightness, and was called IFP2.0 [134]. Since biliverdin is converted from heme by HO1, the published work also incorporated the human version of this cofactor biosynthetically into cells and animals to further increase the fluorophores' brightness.

Still, the observation of dimeric clusters for both IFP1.4 and IFP2.0 under high concentrations motivated the creation of a new and more stable monomeric infrared fluorophore, called mIFP [135]. The main difference between mIFP and its monomeric counterparts is its stability at high concentrations. In comparison to iRFP, mIFP was observed to have similar brightness levels albeit with a 5 times lower photostability in HEK 293 cells [135].

Although claimed to be useful for *in vivo* applications, none of the so far described fluorophores has been shown to perform well for long term recordings of embryonic development. This is clearly the next step needed for microscopy, as infrared fluorophores have the potential to make structures located deep inside the tissue visible, while maintaining high embryo survival rates. With this in mind, the main focus of this work was to create viable

Drosophila lines with constructs based on published infrared fluorophores, and compare their expression levels with other well-known markers.

3.2.1 Infrared fluorophores tested

Our main goal was to be able to create *Drosophila melanogaster* lines which could express a particular version of previously published phytochrome-based infrared fluorophores: iRFP [34], iFP2.0 [134], mIFP [135] and tdiRFP [136] in order to select the best candidate for long-term *in vivo* imaging. Table 3.1 shows all different constructs with their known characteristics.

Up to now, the tandem version of iRFP, tdiRFP, has unfortunately so far been published only as a tool for an extra channel for multicolor imaging of chromatin dynamics: its characteristics have not been fully reported yet. However, considering its nomenclature, it can be assumed that tdiRFP is a tandem dimer. Although monomers are more suitable for quantitative imaging , having the least influence on the tagged molecules activity, our initial goal was set to be able to acquire long-term recordings of embryonic development with traditional histone labeling. Thus, protein stoichiometry was at this stage not a serious issue.

Different *Drosophila* lines with infrared fluorophores

Name	Insertion	Line characteristics	Issues
F20	integrase	; ; H2Av-mIFP/Ser	photostability; clustering
F21	integrase	; ; H2Av-mIFP-HO1	photostability; clustering
F22	integrase	; ; H2Av-IFP2.0/Ser	photostability; clustering
F23	integrase	; ; H2Av-IFP2.0-HO1	photostability; clustering
F1	integrase	; H2Av-tdiRFP/Cyo ;	photostability
F2	P-element	H2Av-tdiRFP(w^+)/FM7twiEGFP(w^{1118}) ; ;	stable
F3	integrase	; ; H2Av-tdiRFP/Ser	photostability

Table 3.1: Different types of constructs tested for infrared imaging of *Drosophila* embryos. Detailed information can be found in the text. All constructs are shown in chronological order of creation.

Table 3.1 shows two different construct versions for both improved infrared monomers, namely IFP2.0 and mIFP (either with or without the addition of human HO1), and three different insertion approaches for tdiRFP.

All integrase strategies utilized the PhiC31 integrase system, with either J27 or VK33 landing sites for insertion on the second or on the third chromosome, respectively [137, 138]. Only one transposase-dependent P-element insertion approach was performed [139,140]. All plasmid injections were performed by the EMBL injection service.

Since the excitation wavelengths for all fluorophores considered are between 680 nm and 690 nm, a 685 nm diode laser (OBIS 685 nm LX, Coherent) was mounted on the optical table and coupled to the optical path with two alignment mirrors. This way all fluorophores tested could be excited with same wavelength, within high absorption regions (> 0.8, with 1 at absorption maximum). Digital and analog inputs were connected to our microscope control hardware, so that the laser could be fully integrated into the microscope system.

The first lines created and tested were named F20-F23, and based on the two monomeric IFP2.0 and mIFP infrared fluorophores. Throughout the imaging tests for all 4 lines we have noticed either strong photobleaching effects, or intense point-like signal localization in random regions inside the embryos, most probably a sign for dimerization effects (in these cases we confirmed with either autofluorescence signal or in brightfield mode that the imaged sample was a fertilized egg, with apparent normal development). We have discarded any quenching effects, as the observed decrease in fluorescence signal was not a reversible process. Such effects make long-term recordings of live embryos an infeasible task. These negative results for the monomeric versions motivated us to go back and test the iRFP in tandem form: a tandem dimer should show very different clustering behaviour, if any. In addition, we decided to perform insertions not only following the PhiC31 integrase system, but also the transposon strategy underlying the P-element method. Although the randomness of P-element insertion may lead to disruptions on the normal pattern of endogenous genes, it also offers the possibility of having the construct inserted in a more stable region of the genome, offering high expression and low toxicity [139]. Out of all three different constructs, both integrase-based fly lines demonstrated unusual low number of offsprings, and embryos still showed very low signal, with very high photobleaching behaviour. No pre-gastrulation embryos with signal could be found as well. Only one of the possible P-element insertion lines, which originated the F2 fly line, showed promising results. All F2 embryos have so far present signal, with enough fluorescence intensity being detected even in embryos at early mitotic cycle 10, i.e. when the nuclei have just surfaced. Through balancer crosses it has

been noted that the insertion is located in the X chromosome. The flies are heterozygous viable, and further tests should confirm whether homozygous and hemizygous viability is possible.

3.2.2 Long term recordings of embryonic development with tdiRFP

With the successful creation of a fly line expressing an infrared fluorophore, the next step comprised on performing long term recordings of the embryonic development, in order to better understand its performance. These are the first recordings of most of the *Drosophila melanogaster* development in the infrared region ever taken, *in toto*, and *in vivo*. In this work we will focus on two acquired 3D movies, each with slightly different acquisition strategies: while the first utilized rather long waiting times between timepoints and slightly higher illumination laser powers, the second recording focused on reproducing usual imaging conditions established in the lab, so that the final data could be used for comparison with recordings taken with two other well-established fluorescent markers (this latter part will be discussed in the next section, Section 3.2.3.).

The following parameters were utilized initially: laser powers of 560 mW (all powers measured at the back focal plane of the objective) with timelapse recordings every 3 minutes, and 23 ms effective exposure time for each plane ($cf.$ the calibration procedure in Section 2.1). Stacks were acquired in two different views, using a sample rotation of 90°. Images were taken with simultaneous illumination and eCSD detection on both cameras, with a confocal slit size of 1.5 Beam-slit units ($cf.$ Appendix A). It draws a first glance at the embryonic development imaged with infrared wavelengths. One way to look at such long recordings is by making a kymograph of a selected lin drawn on a maximum intensity projection movie of the entire recording, as depicted in Figure 3.2a. The result is shown in Figure 3.2b, with selected developmental stages depicted in color coded lines[1]. Table 3.2 shows a summary of developmental stages during *Drosophila* embryogenseis, with corresponding selected stages highlighted. All recordings were performed in a room at 21°C, which means that the developmental timings are extended corresponding to previous observations [143].

[1] All developmental stages here presented follow the definition found in M. Bownes [141] and the book from J. A. Campos-Ortega and V. Hartenstein [142], which also provides a very informative compendium on *Drosophila* development.

Summary of morphological events during *Drosophila* development

Stage [141, 142]	**Event**
2	Posterior gap appears
3	Pole bud formation
4	**Nuclei reach periphery of the yolk (mc10)**
5	Cellularization (mc14)
6	Ventral furrow, migration of pole cells dorsally
7	**Appearance of dorsal folds**
8	Anterior midgut primordial
9	Stomodeal plate forms
10	Stomodeum invagination
11	**Full germband extension**
12	Germband retraction onset
13	**Full germband retraction**
14	Midgut closure, unification
15	**Heart-shaped midgut, dorsal closure**
16	Convoluted gut
17	**Muscle contractions**

Table 3.2: The selected developmental stages shown in Figures 3.2 and 3.3 are highlighted in bold.

Another way of representing this kind of recording can be realized through selection of representative timepoints: this is illusrated in Figure 3.3, where the selected stages from Figure 3.2b are presented as maximum intensity stack projections from two different views, following the same color-code. In Figure 3.3a-c, developmental stages corresponding to cellularization, and ventral furrow (vf) with germband extension (gbe) are respectively shown (stages 5,7,11, respectively). Pole cells (pc) are clearly visible during stage 7, migrating dorsally as well as the cephalic and dorsal folds (cf, df). From stage 9 onwards the intensity of certain cells start to increase at a much faster rate than the rest of the embryo: this can be seen in Figure 3.3c, representing stage 11. Although an inattentive look might assume that these are the amnioserosa cells (amn), Figure 3.3d proves otherwise: the midgut (mg) precursor cells are clearly visible in stage 13, with the shorter midgut closure (mgc) presenting a more intense profile than the larger dorsal closure (dc) region covered by the amnioserosa cells. In addition, brighter cells closer to the ventral side can be observed in the lateral view: these could correspond to the midgut precursor (mgp) cells. In

fact, after dorsal closure is finalized during stage 15 these cells seem to make the ventral part of the midgut, now internalized and with its characteristic heart shape, which can be seen through all other tissue layers. Finally, around 21.5 hours after mitotic cycle 10, the convoluted gut (cg) is fully formed and the extension of the salivary glands can be seen.

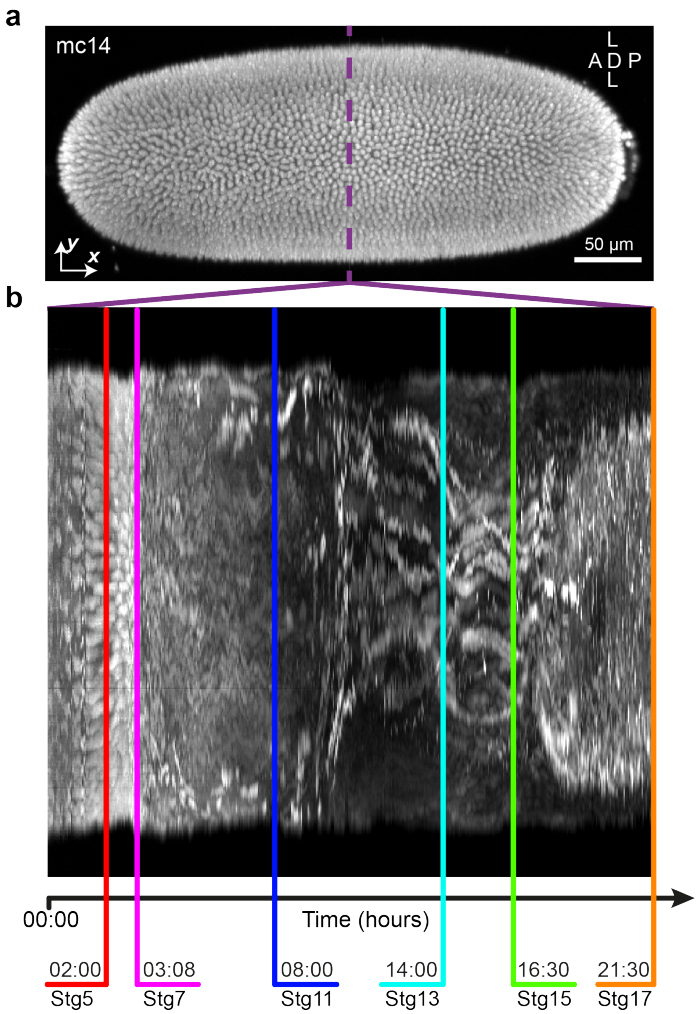

Figure 3.2: Kymograph of a 21.5 hours timelapse imaged with infrared fluorophores. Acquisition started at stage 4, when nuclei just reached the periphery of the yolk, during mitotic cycle 10, and this was considered time 0:00. **(a)** A representative maximum intensity stack projection during mc14 depicts the selected line for the subsequent kymograph in purple dashed line. **(b)** Kymograph from the timelapse in maximum intensity stack projection taken from the dashed line presented in (a). Time is shown in hours, and color-coded selected stages are depicted. Ventral furrow (between stages 5 and 7), germband extension (from stage 7 up to stage 10), retraction (from stage 10 up to stage 13), and dorsal closure (from stage 13 up to stage 15) are visible. After dorsal closure is completed, the gut is fully formed, muscle activity sets in, and no more large scale morphological events can be devised. The color-code is used as reference in Figure 3.3.

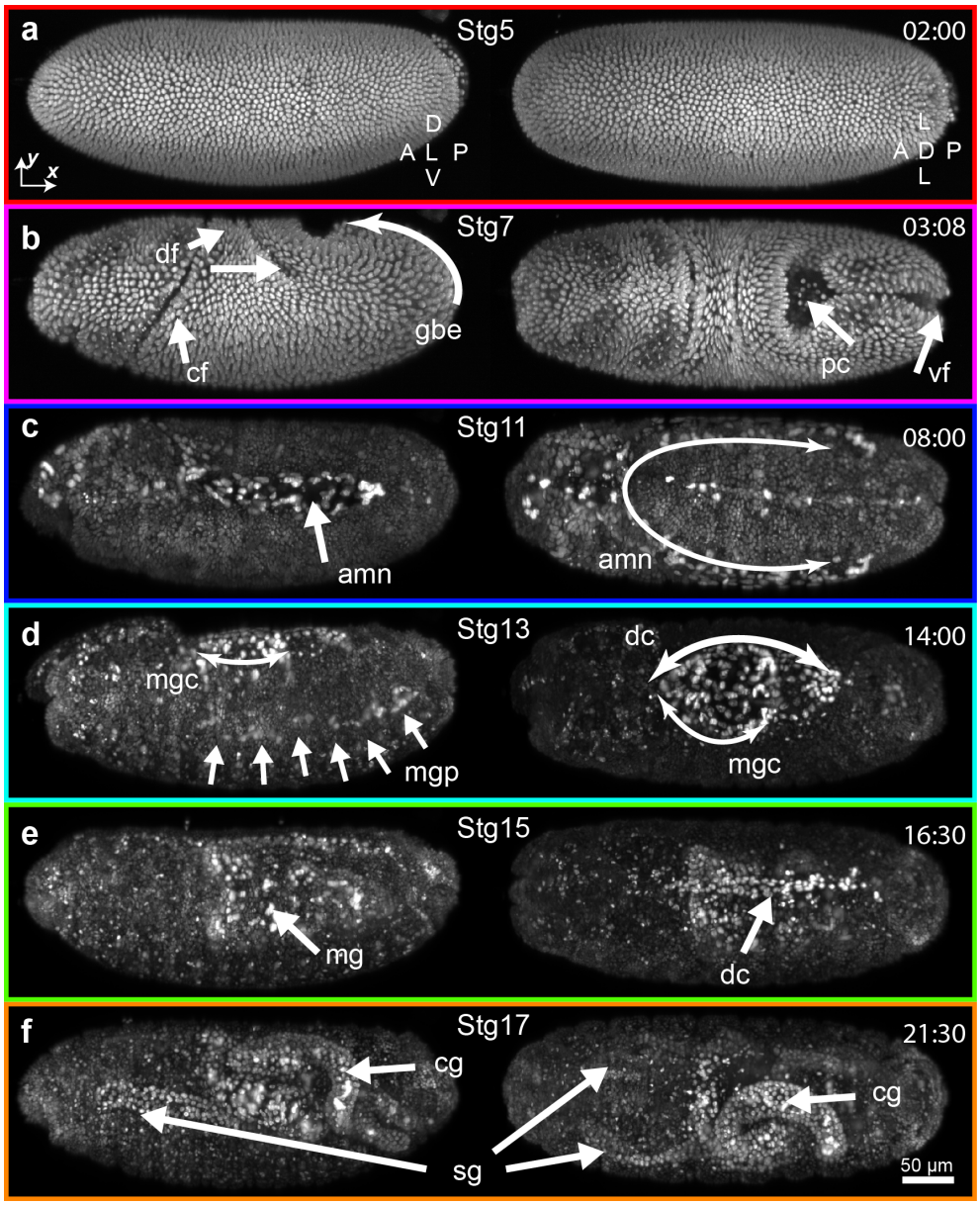

Figure 3.3: Dorsal and lateral views of particular developmental stages with infrared imaging. Lateral (right) and dorsal (left) maximum intensity stack projections of a *Drosophila* embryo with labelled H2Av-tdiRFP. Corresponding stage numbers are shown in the center, and white arrows depict selected visible features. Time (in hours) shown on upper right, related to the beginning of the recording, at mitotic cycle 10 (stage 4). All images have been normalized, each with 1% saturated pixels. Color code around each timepoint follows definition from Figure 3.2. **(a)** Two hours after mc10, cellularization occurs, and the nuclei become elongated. **(b)** After onset of ventral furrow (vf), pole cells (pc) become confined in a pocket which moves dorsally during germband extension (gbe), and dorsal folds (df) appear, characteristic of stage 7. **(c)** Stage 11 showing full germband extension. Amnioserosa (amn) cells are visible all around the extended germband. **(d)** After full retraction of the germband, dorsal closure begins (dc), along with the midgut dorsal closure (mgc). Laterally it is possible to see the cells which possibly form the midgut primordium (mgp), a characteristic of stage 13. **(e)** Stage 15: midgut closure completed, dorsal closure finalizing. The midgut (mg) is clearly seen through the tissue, internalized, and with its typical heart-shape. **(f)** At this late stage muscle activity has started, and the convolved gut (cg) is clearly seen. Additionally, the sallivary glands (sg) can be recognized, extending forward towards the head. Throughout the recording, the room temperature was kept at 21°C, reason why there is an extension on the developmental timings.

In order to provide a certain representative perspective on the entire recording, Figure 3.2b shows a kymograph of a single line, encompassing all timepoints. A representative timepoint at mitotic cycle 14 along with the corresponding region of interest for the kymograph are displayed in Figure 3.2a. The kymograph is taken from one camera view data, showing the dorsal side of the embryo; each timepoint has been projected along the stack direction (z), and further intensity normalization was enforced so that all timepoints can be clearly visible. Specific stages of development are depicted with color-coded lines. The same coding is used to show embryo projections of each selected stage in two different views in Figure 3.3.

3.2.3 EGFP-VS-mCherry-VS-tdiRFP: different markers comparison

Following the observation of organs deep into the tissue with tdiRFP, a qualitative comparison between our infrared data with recordings acquired with other well-established fluorophores was needed. We chose fly lines expressing histone labelled with either EGFP or mCherry, as these fluorophores do not spectrally overlap (EGFP has excitation and emission peak at 488 nm and 508 nm,respectively, whereas for mCherry these values are at 596 nm and 610 nm), are found to be monomeric and are widely used for *in vivo* imaging. In order to have a fair comparison between markers, same developmental timepoints needed to be selected for each embryo. This motivated us to perform long-timelapse recordings for each fly line, so that we could choose a certain stage of interest with more flexibility. Apart from different illumination laser intensity, all three timelapses were acquired with 25 ms effective exposure time per plane, a waiting time of 1 minute in between timepoints, and were comprised of datasets from two views, meaning that a 90° sample rotation was performed for each timepoint. All recordings utilized eCSD confocal detection [78]. Illumination laser powers for EGFP and mCherry excitation were chosen in order to keep high amount of detected signal, while at the same time maintaining laser powers just below embryonic phototoxic limits; this stems from empirical observations in the lab. For tdiRFP, intensity was likewise chosen so that detected fluorescence signal has similar intensity values to those from EGFP and mCherry emission. In laser power percentage values this corresponded to irradiance values of 74 μW at 488 nm for excitation of EEGFP, 30 μW at 591 nm for mCherry, and 275 μW at 685 nm for tdiRFP.

All three recordings start before gastrulation, at mc14, and end during muscle activity of the embryo, with recordings lasting in average more than 20 hours. It has to be noted that the sample chamber had a stable average temper-

ature of 21 °C, which implies that the entire development should take around 30 hours post cellularization phase [143]. After each recording was finalized, the embryos were left unperturbed inside the imaging chamber overnight, and on the following day it was noted that all embryos have hatched: this is an important control, which points at the direction that the chosen imaging parameters did not hinder embryonic development. Data fusion was performed following the direct sum of opposing stacks, along with direct sum of different views, after registration (*cf*. Section 2.2), regardless of the fluorescent protein used.

A couple of especially representative timepoints have been selected to be shown here. Stage 7, as presented in the section above, corresponds to the moment where ventral furrow has already started and the pole cells, which move forward during germband extension, are localized for the first time inside a pocket formed by the posterior midgut primordium. All three embryos are depicted at this stage in Figure 3.4a-b. Figure 3.4a shows fused data intensity projection of all three markers. Apart from different embryo sizes, no large differences between all three embryos can be observed. Nonetheless, if a projection of about the 50 µm encompassing the pole cells (as illustrated by the dashed lines) is performed, distinct differences between each dataset can be recognized. The detrimental effects of autofluorescence in the yolk are clearly visible for EGFP, also showing the vitelline membrane surrounding the embryo. As a result, the cells which make up the tissue just below the pole cells on the dorsal side, as well as the inner furrow cells on the ventral side are basically not distinguishable. For mCherry, the situation is much improved, as the autofluorescence background has basically vanished, and more of the inner structures can be seen. Also, the signal is more homogeneous due to the direct sum of opposing camera stacks. Still, only tdiRFP is able to provide a clearer image of the innermost furrow cells and other structures. Normalized signal to noise measurements (shown in Figure 3.4c) confirm this: only with infrared wavelengths it is possible to have a clear image of all the inner relevant structures at this developmental stage.

The situation is even more pronounced at slightly later stages, when germband extension has reached maximum length and pole cells are localized inside the cavity formed by the posterior midgut primordium, which in turn lies deep inside the yolk (stage 9). The three markers are compared to each other during this stage in Figure 3.5. Figure 3.5a shows maximum intensity projections of 25 µm thick slices encompassing the region where the pole cells are expected to be located (around the middle of the embryo) and present very

different results for the three different markers evaluated. Just as in Figure 3.4, the effects of autofluorescence and scattering in the EGFP case lead to dramatic decrease in signal. This is also exemplified in Figure 3.5b, which depicts a cross-section view of a maximum intensity projection volume (the volume extent, around 50 µm in length from anterior to posterior poles, is outlined in white in Figure 3.5a) encompassing the pole cells region. The EGFP fluorescent embryo shows, apart from faint nuances of the mesoderm layer, no inner structures, whereas with mCherry the situation is improved. Here, the region of the posterior midgut primordium can for instance be distinguished. tdiRFP flies exhibit, however, much more defined structures. There is a clear distinction of the posterior midgut primordium, and even the recognition of pole cells inside its volume. Details can be easier observed in Figure 3.5c, where inserts corresponding to the brown dashed boxes depicted in Figure 3.5a present a dramatic improvement in image quality deep inside the embryo. It is important to note that these structures are usually located at around 70 µm depth at this stage, and so far have not been visualized throughout development with fluorescent markers *in vivo*.

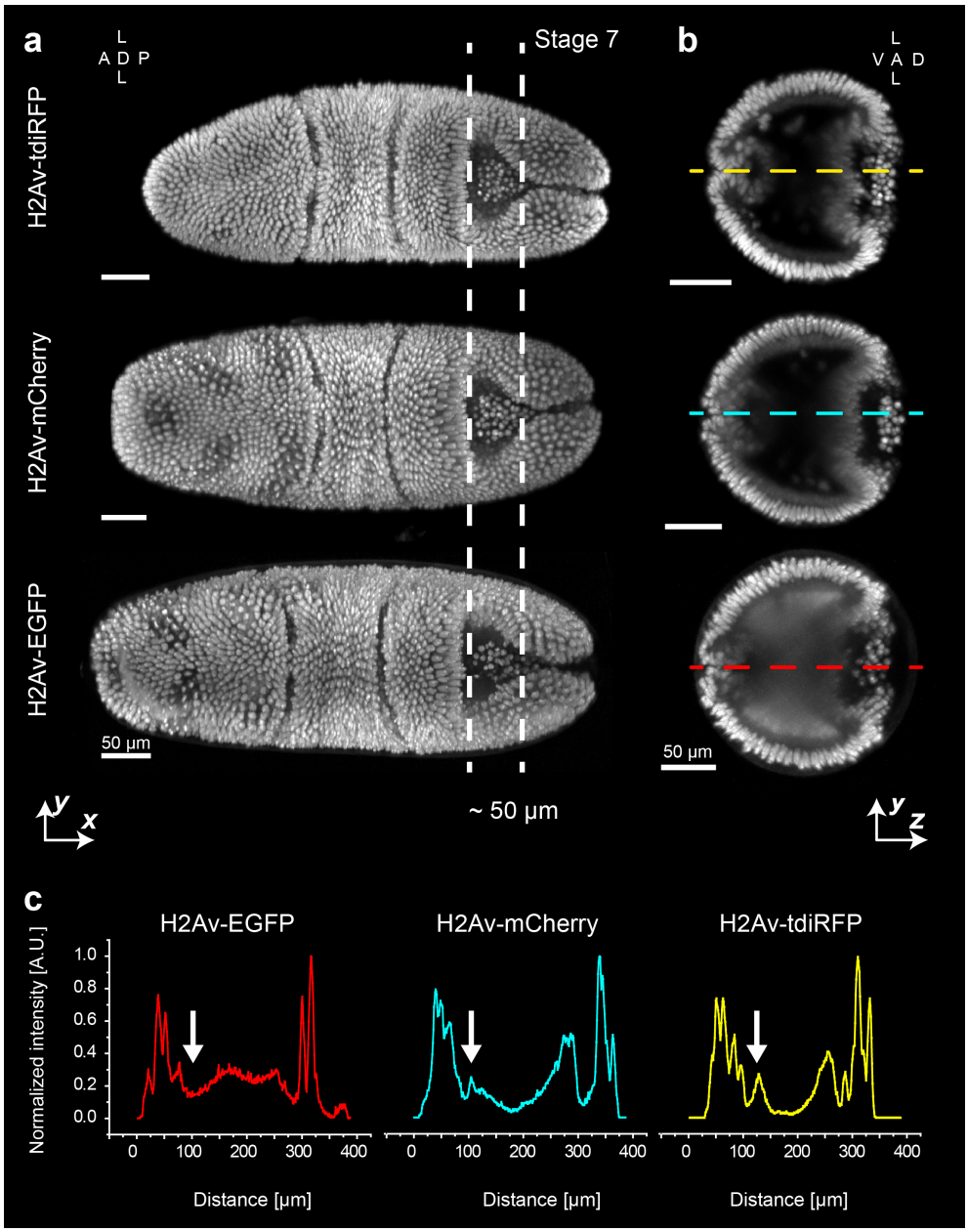

Figure 3.4: Different markers comparison using *Drosophila* embryos at stage 7. Images were produced using maximum intensity projections and appropriate histogram equalization so that all present around the same intensity profile. Embryo orientation is shown on the upper left and upper right regions of the figure. L,V,D correspond to lateral, ventral and dorsal regions; A and P correspond to anterior or posterior poles. **(a)** Dorsal view of three different embryos, each expressing a different histone marker. Apart from the different embryo sizes, all of them present a normal phenotype for an embryo at stage 7. **(b)** Maximum intensity projections of cross-sectional data for each embryo, retrieved from within the dashed lines marked in (a). For the EGFP embryo the signal originating from autofluorescence is clearly visible even from the yolk surrounding the embryo, and even the vitelline membrane is recognizable. The mCherry variant presents a much cleaner signal especially inside the yolk; the nuclei forming the innermost part of the ventral furrow are however not clearly visible. With infrared fluorophores not only the nuclei which form the germline cells pocket can be recognized, but also the innermost nuclei which form the furrow. **(c)** Additional line profiles, normalized to each maximum value, reinforce how signal is improved with tdiRFP in comparison to the other markers. All scale bars represent 50 µm.

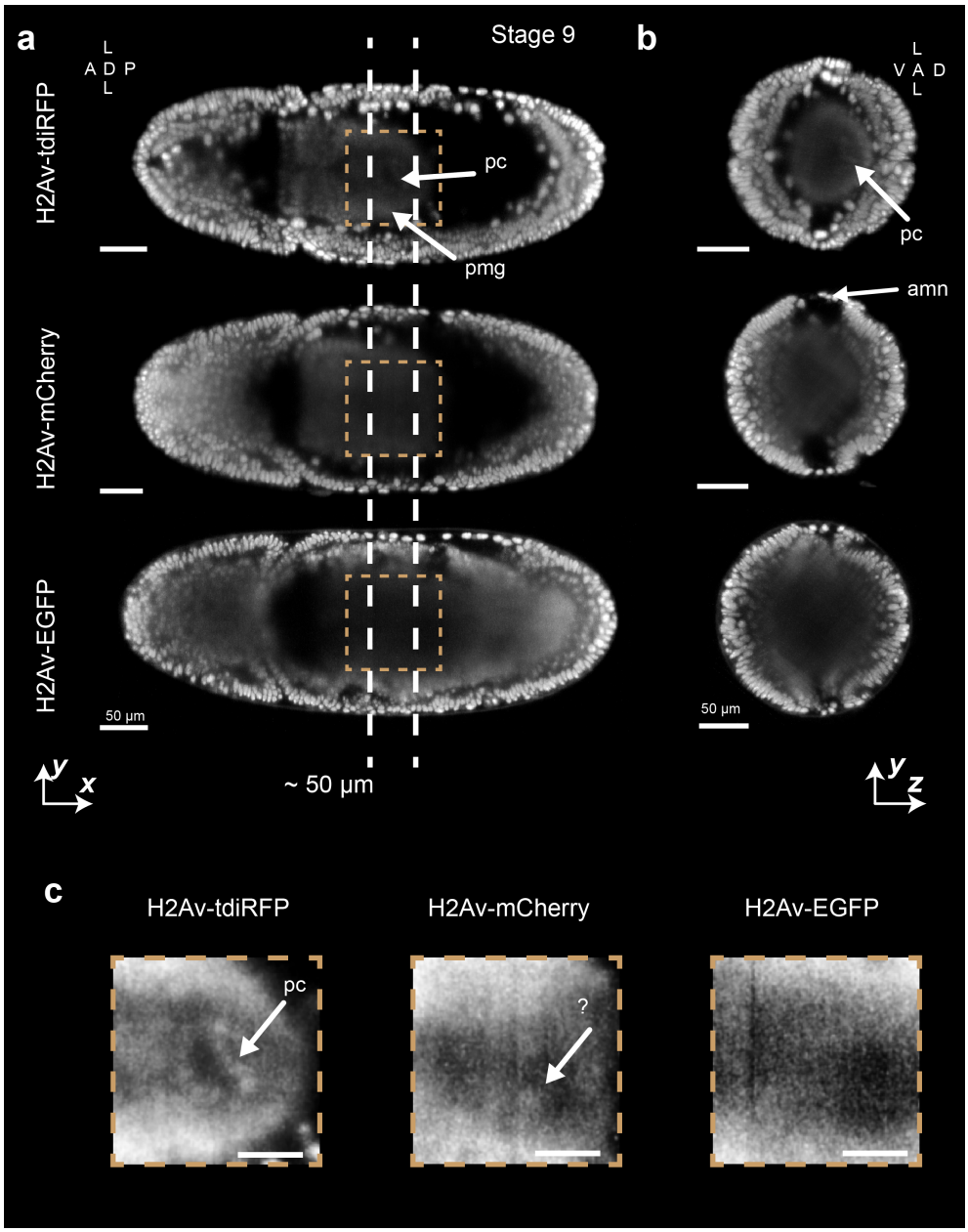

Figure 3.5: Different markers comparison using *Drosophila* embryos at stage 9. Images were produced with the same scheme as in Figure 3.4. Embryo orientation is shown on the upper left and upper right regions of the figure. L,V,D correspond to lateral, ventral and dorsal regions; A and P correspond to anterior or posterior poles. **(a)** in-plane sectional data around 25 µm thick depict the region encompassing the inner space of the posterior midgut primordium. From EGFP to tdiRFP, the amount of inner structures visible is increased, with the latter case presenting clearly a fully distinguishable outline of the posterior midgut primordium and even a faint signal of the pole cells (pc) located in its interior, shown with arrows. **(b)** Cross section of the ca. 50 µm thick region depicted whithin the dashed lines in (a). All scale bars represent 50 µm. **(c)** Insert on the region corresponding to the brown dashed boxes in (a), depicting the region where it is expected that the pole cells (pc) should be located. Only with tdiRFP are they clearly visible. These inserts have been blurred with a gaussian kernel and the histogram has been equalized with 1% of all pixels saturated. Scale bars represent 25 µm.

3.3 Discussion

Although the creation of new infrared fluorophores has opened new perspectives towards deep tissue single photon imaging of live samples, there is still a strong need for bright and photostable monomeric fluorophores. In particular, higher quantum yields would allow that even monomeric fluorophores can compete with the emission intensities obtained from the tandem dimeric tdiRFP, with comparatively less illumination laser powers needed. So far, no monomeric infrared fluorophore could be used for long-term *in vivo* imaging. From the illumination side, longer light-sheets could be beneficial for penetrating deeper into the tissue. In MuVi-SPIM [4], we utilize two illumination beams, each offset from the other by its Rayleigh range, so that the combined virtual beam has a longer depth of focus. Although other strategies exist utilizing different beam profiles, such as Bessel or Airy shapes [69, 70]. Gaussian beams, however, lack any multiple side lobes which could generate background signal, therefore being the preferred illumination profile.

The data shown in this chapter is only part of the first steps towards a broader study on the effects of infrared imaging in live tissue, in particular for developmental studies. The comparison of different markers throughout further timepoints in *Drosophila* is still ongoing work. It is clear from the first results, however, that imaging with tdiRFP can improve image quality at depths of at least 70 µm, allowing for the first time the observation of structures close to the center of the embryo during *in vivo* recordings with fluorescence microscopy.

That specific cells become increasingly more intense during development can also be observed with other labels, such as mCherry [4]. Although salivary glands and parts of the gut can also be recognized, the difference in signal to the average intensity coming from other cells in the embryo is not so pronounced as in the case with tdiRFP. One possible explanation could be related to the fact that different cells produce different amount of biliverdin. It has been shown, for example, that neurons should produce this protein only in very small quantitites [134]. Another argumentation could be that, due to transposonal insertion, the construct could be located in a region of the genome which is more highly active in cells with particular cell fate. Validation of this assumption could be done through genome sequencing. Despite this, further evaluation of the datasets obtained with infrared wavelengths needs to be performed so that a better understanding on the characteristics of the fluorophore, and of the fly line generated can be assessed.

Furthermore, constructs with the addition of heme oxygenase should be

tested and compared with the already obtained data from the F2 line: this way a more homogeneous signal could potentially be reached. Also, the high concentrations of the tandem dimeric fluorophores could potentially sequester large quantities of biliverdin, leading to low endogenous levels throughout development. As low levels of biliverding in *Drosophila* have been shown to lead to phenotypic eye malformation [144, 145]. Unfortunately, with the *FM7* balancer it is not clear to observe whether the flies show the same eye phenotype. Although most publications have focused on human heme oxygenases, we would favour for the insertion of the sequence of the heme oxygenase common to *Drosophila* (entry number Q9VGJ9 in `www.uniprot.org`) as it has been noticed that there is a low degree of conservation between that and the human HO1 (entry number P09601, only 30.2 % match): studies have shown that *Drosophila* heme oxygenase is distincly different from other HOs, as it seems to produces more isomers of biliverdin. This would point to a different overall structure [146, 147] than that of the known heme oxygenases found in nature.

We believe that improvements on existing fluorophores, or yet the creation of new sub-families with enhanced fluorescence properties will bring the usability of infrared fluorophores to a different level, enabling the possibility to visualize for the first time important morphogenetic events (e.g. vascularization, organ formation, etc) live.

Chapter 4

Deep tissue laser photomanipulations with light-sheet microscopy

Pulsed lasers offer the possibility of interacting with tissues in a very controlled manner, both in space and time. Together with light-sheet imaging of live specimens *in toto* and *in vivo* throughout long periods of time, the mechanical role of important agents or events throughout morphogenetic changes can be inferred, providing important complementary information to biochemical experiments.

The first implementation of an optical path dedicated for high power laser interactions with tissue in a light-sheet microscope was built in EMBL in 2007 [148]. The work utilized an ultraviolet (UV) laser coupled to the detection path with a dichroic mirror[1] to perform laser ablations on tissue. The authors presented precise cuts performed in a wide range of sizes, from single microtubules in the submicron scale to the caudal fin of Zebrafish - around 50 µm in size. The imaging microscope consisted of a two-lens light-sheet setup. The short wavelength of 355 nm, however, lead to strong chromatic aberrations - up to 26 µm axially - which could only be corrected through controlled movement of the specimen towards the detection objective. This made it impossible for the system to visualize the ablated region as ablation was performed. Furthermore, UV wavelengths are usually highly absorbed by biological tissue, as discussed in Section 1.5.1. This in turn meant that large penetration depths

[1] The change in nomenclature from dichroic filter to dichroic mirror reinforces the focus of this chapter on the ablation laser utilized, and will stay consistent until the end of the chapter.

with such lasers were not achievable, only allowing interactions near the surface.

This chapter presents the methods we established to perform simultaneous laser manipulation and 3D visualization of thick specimens by coupling a femtosecond infrared laser into our multi-view light-sheet microscope. The flexibility of the optical path allows it to be adjusted into any light-sheet setup, its usability spanning from precise diffraction limited ablation spots up to larger areas. Our customized control software combines the power of 3D imaging and laser manipulation in an automatic way, allowing the probe of entire living samples with a large range of different laser-tissue interactions. We present several examples of experiments which can be carried out with our setup: included here are deep tissue ablation and cauterisation experiments in *Drosophila melanogaser*, and specialized laser ablations inside the brain of Zebrafish embryos. This tool, allied with genetic and chemical perturbations, can aid in bringing biological events to a deeper level of understanding by bridging knowledge through controlled fast and localized mechanical tissue perturbations. Currently the work presented here is under preparation for a future publication.

4.1 Infrared pulsed laser system in multiview SPIM

4.1.1 Optical setup

In comparison to visible light wavelengths, the infrared spectrum around 1000 nm suffers from less scattering effects and is thus more suitable for deep penetration into the tissues (*cf*. the discussions presented in Section 1.5.2). However, laser-tissue interactions with infrared light require large photon densities so that there is high enough probability that multiphoton absorption can occur. This is best achieved if a beam with large diamter is tightly focused to a small volume. In parctice, this means expanding the infrared beam in order to fill the back aperture of one of the detection objectives of our MuVi-SPIM setup. The optical path is shown in Figure 4.1. The infrared laser source used is a Mikan laser from Amplitude Systèmes (MPL in the figure). Its main properties are shown in Table 4.1. Pulse trains originated from the Mikan go through a $\lambda/2$ waveplate with special coating for 1030 nm and a Glan Thompson prism (GLTP) (WPH05M-1030 and GL10-B, both from Thorlabs), the latter being attached to a motorized rotation stage (M116-DG stage with a C863-DC Mercury controller, from Physik Instrumente).

The $\lambda/2$ plate rotates the pulses' polarization, and the Glan Thompson

prism allows polarization components with one particular orientation to pass through as the extraordinary beam, all other components being redirected outside the optical path. A mechanical shutter (S, Uniblitz VS25 25 mm shutter and a VMMD-1 shutter driver, from Vincent Associates) is placed in front of the Mikan laser, at an angle so that when closed the reflected infrared beam can be directed into a beam dump. Together, these three parts control exposure time and the laser power used. All mirrors (M) are broadband dielectric (BB1-E03, coated for 750 - 1100 nm spectral range). Infrared laser pulses are then expanded spatially once, by a factor 5/3, with two (L1,L2) infrared-coated lenses (focal lengths 30 mm and 50 mm. LB1757-B and LB1471-B, from Thorlabs), and enter a specially designed cube which houses the 2D steering optics. The system is composed of a right angle dielectric mirror (MRA10-E03, Thorlabs) which guides the infrared pulses to a 2D galvanometric mirror set from Cambridge Technologies (each mirror associated to a VM500+ motor, with a 673 dual axis servo controller), the responsible mirrors for steering (translating) the focal spot of the focused beam in the FOV of the sample (y-GSM, x-GSM). Furthermore, the cube also houses the first lens of the second and last beam expansion (L3), and the whole cube can be built on top of optical rails. This promotes the flexibility for axial alignment of the focal spot, which can be especially important when a medium with different refractive index needs to be used in the sample chamber in order to ensure *in vivo* imaging, for example. The housing is depicted in Figure 4.2.

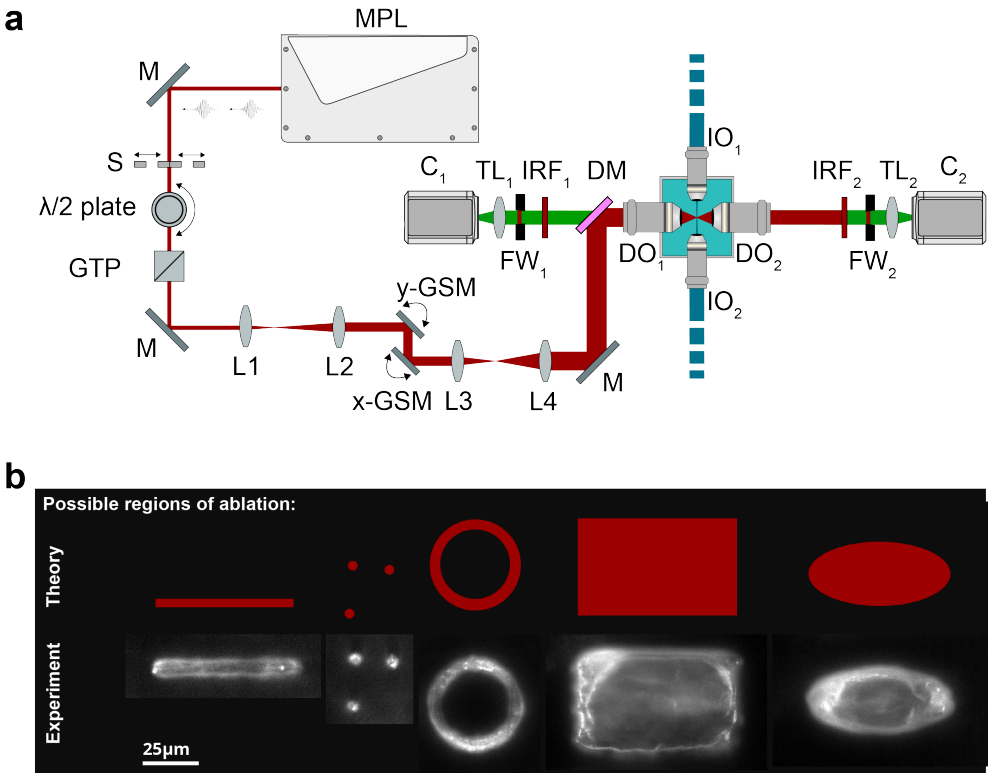

Figure 4.1: Scheme of the optical setup and possible ablation regions. (a) The multiphoton ablation unit is shown on the left part of the sketch while part of the the multiview light-sheet microscope is shown on the right. The multiphoton laser (MPL) produces ultrashort pulses that can be blocked or transmitted with the help of a shutter (S). A motorized $\lambda/2$ plate in combination with a Glan Thomson prism (GTP) is used to control the power of the laser. Following the power control unit the beam is expanded 2 times via a beam expander (L1, L2). The galvanometric scan mirrors (y-GSM, x-GSM) are located in the proximity of the conjugated plane of the detection objective's back aperture. Therefore their rotation corresponds to a rotation in the back aperture of the detection objective. Next, the beam is expanded 8 fold by a second beam expander (L3, L4) to fill the entire back aperture of the detection objective. A dichroic mirror (DM) finally redirects the infrared light towards the back aperture of the detection objective (DO_1) while still allowing fluorescent signal to be detected. Several mirrors (M, not all illustrated) are used to redirect the infrared laser towards the dichroic mirror. The multi-view light-sheet microscope has two illumination (IO_1 and IO_2) objectives and two detection (DO_1 and DO_2) objectives. Each detection path consists additionally of respective filter wheel (FW_i), tube lens (TL_i), and a camera (C_i), i=1,2. To prevent possible infrared light to reach the cameras two infrared filters (IRF) are added to the detection path. **(b)** The custom-made software allows to perform 5 different ablation patterns, each of which in variable sizes/ratios. From left to right are shown the theoretical regions of ablation (ROAs) with the resulting ablations below. The ablations were performed on a piece of nylon and imaged with 488 nm excitation.

Properties of the Mikan laser source

wavelength λ	1025	nm
pulse duration τ_{pulse}	200	fs
average power $\bar{P}$	1.1	W
repetition rate f_{rep}	54	MHz
pulse energy E_{pulse}	20.3	nJ

Table 4.1: Properties of the infrared pulsed laser source.

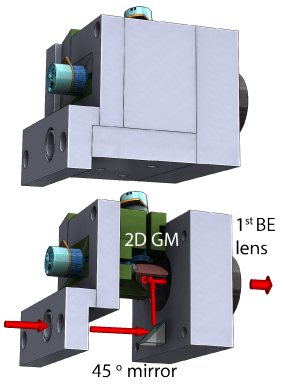

Figure 4.2: Closed scanner mount. Dedicated housing for the 2D scanners with a mounted mirror and first lens of the second beam expander. The infrared laser path is shown with red arrows: it enters the housing from the left, being reflected by a 45 degree angle mirror upwards to the set of galvanometric mirrors, being then redirected outwards through the first lens of the second beam expansion (black).

The second beam expansion (L3,L4; roughly 7.8 times expansion with 25.4 mm LB1761-B from Thorlabs and a 200 mm NIR coated 49-506 from Edmund Optics) also acts as relay optics, imaging the back focal plane of the objective to a plane located in between the two galvanometric mirros. This way each mirrors' angular movement control ensure proper translation of the focal spot on the field of view. The fully expanded beam with a diameter of roughly 13.4 mm – at $1/e^2$ is directed to one of the detection objectives of our multiview light-sheet setup (DO_1; 25X/1.1 numerical aperture (NA), water immersion, infrared corrected, CFI Apo LWD, Nikon) via a 5 mm thick Semrock dichroic filter (DM; FF01-680/SP-25). The thickness of the dichroic mirror was chosen in order to avoid changes in the profile of the focused spot thus maintaining its diffraction-limited properties: previous tests with thinner dichroic mirrors have have shown aberrations in the beam's profile, an effect which was minimized after exchange to thicker glass plates.

Due to the geometrical configuration of the four objectives in MuVi-SPIM both detection objectives share an overlaping focal plane. This can however be particularly dangerous when focusing high intensity pulsed laser with one of the objectives, as due to symmetry the infrared pulses are going to be focused on the opposing camera through the second objective. It is therefore crucial that opposing detection path is protected from transmission of infrared wavelengths. The same caution is also necessary for the detection path where the infrared laser is coupled to: also this camera has to be protected from any back reflections. For these reasons, extra 680 nm short-pass (SP) filters from Semrock (depicted as $IRF_{1,2}$; FF01-680/SP-25) has been added to each detection path, which blocks the Mikan's infrared light with an absorbance – usually termed as *optical density* – factor of around 10 (OD10). The dichroic mirror and the short pass filter is mounted in a dedicated turret with easy access, shown in Figure 4.3. Each optical element can be mounted separately, being also possible to leave the turret empty if necessary, sot that it can act solely as protection from outside light sources.

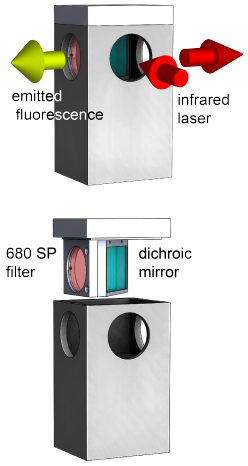

Figure 4.3: Dichroic and infrared clean-up filter turret. Cartoon depicting the especially designed turret which houses the independently removable dichroic mirror and 680SP filter. The kinematic mount allows the top part with both optics to be removed or reattached without need for realignment.

The maximum pulse energy in Table 4.1 can be calculated through the ratio between the average power and the repetition rate, P_{avg} and f_{rep}, with $E_{pulse} = P_{avg}/f_{rep} \approxeq 20.3\,\text{nJ}$. This is considering no losses: however, a decrease of around 10% of the average power has been measured at the back aperture of the objective. In fact, we consider a total energy loss of around 40% at the focus after the objective, due to the objective's optics.

If we take into account the radius at the focal spot according to the Rayleigh criterion, as discussed in Section 1.2.2:

$$r = 0.61\frac{\lambda}{NA} \approxeq 568\,\text{nm}. \tag{4.1}$$

we can then calculate to the upper limit for the energy density at the focus (taking into account that 60% of light is lost in the process):

$$\hat{E}^{max}_{pulse} = \frac{0.6 \cdot E_{pulse}}{\pi r^2} \approxeq 1.2\,\text{J}\,\text{cm}^{-2} \tag{4.2}$$

Calculating the peak power density of each pulse at the focal spot yields:

$$\hat{P}_{pulse} \approx \frac{\hat{E}^{max}_{pulse}}{\tau_{pulse}} = 6 \cdot 10^{12}\,\mathrm{W\,cm^{-2}} \tag{4.3}$$

The resulting peak power suggests that photodisruptive effects should be achievable with the system, as can be confirmed in Figure 1.13. No pulse broadening effects were considered in the calculations. Although this could lead to strong deviations in peak power values, the detection objective and all other optical elements are expected to work well in the spectral region and the laser powers considered, and so it is reasonable to consider that absorption is the most prominent effect, meaning that the assumption that the detection objective generates loss of power but rather small pulse broadening should still be valid.

4.1.2 Software

In order to be able to perform experiments in a reproducible way, careful control on infrared laser power and exposure time is indispensable. In addition to this, automatic positioning control of the infrared focus on the field-of-view is also necessary, so that different regions of ablation (ROA's) can be utilized reproducibly, as shown in Figure 4.1b. Laser intensity control is performed through a calibration procedure between voltages from the rotation stage to which the $\lambda/2$ plate is attached and measured laser intensity at the back aperture of the detection objective. After the calibration is performed, a custom-written LabView software provides the necessary laser intensity controls; digital signals sent to the Uniblitz shutter controls the exposure time of interaction. The 2D set of galvanometric mirrors is also calibrated and controlled automatically through LabView. Calibration follows an analogous procedure as for the electronic confocal slit (Section 2.1), extending it to a 2D space.

4.2 Examples

As discussed in Section 1.6, there are many different effects which can be caused through laser-tissue interactions, all of them depending only on the time of interaction for fixed power densities. Here we show four examples of different experiments which can be performed with the developed system. All of them rely on photoinduced damage at different scales of power density magnitudes, tissue depths and overall laser exposure times. Each example is shown as a proof of concept on a particular case scenario where the infrared

ablation setup coupled to MuVi-SPIM can be advantageous on providing new biological insights. As will be further demonstrated, the combination of multiview light-sheet microscopy and infrared ablation systems allow unprecedented *in toto* manipulation capabilities. Each example is presented within a framework of a brief motivation, methods and results sections. As may be expected, these are just representative experiments; the same settings can be applied for a range of other possible projects.

4.2.1 Tissue cauterisation

Throughout development, morphogenetic shape changes oftentimes affect the entire embryo, leading to massively coordinated tissue movements which are vital for the creation and further development of its organs. Studies on particular subunits of the whole tissue have been able to elucidate the morphogenesis of specific organs and other cell assemblies (such as the in the case of the gut, utilizing infrared single photon excitation microscopy, as described in Chapter 3). Although they reveal the underlying molecular mechanisms and genetic processes, little is known about how all these units coordinately behave in the context of an entire organism.

For example, the very first radical change in body plan happens during gastrulation, where the embryonic tissue folds into itself so that inner organs can be formed. In *Drosophila*, this event appears after the completion of cellularisation during the mitotic cycle 14, when a ventral furrow is created, which is eventually internalized. So far little is known about how different tissue subunits act towards furrow formation, and until recently the only work known had been performed in Ascidians [149] in the context of endoderm invagination. In the fruit fly, one way to probe the roles of different tissue regions on furrow formation could be through the creation of a localized perturbation which could hinder the normal cell movement during gastrulation by fixating the inflicted cells to a fixed tissue layer. In fact, this kind of perturbation is possible with pulsed lasers and has been known in the medical field for many years.

Cauterisation or *tissue stitching* - also known as *tissue welding* [150] -, is a tissue response which can take place when thermal interaction is the predominant effect during and after irradiation [90,92], requiring rather low laser powers and long exposure times (*cf*. Section 1.6). It has already been shown that using pulsed infrared laser sources it is possible to localize inflicted damage to small volumes even inside embryos such as *Drosophila* [151]. Cauterisation experiments are performed in the context of furrow formation by localizing the

infrared beam between the vitellin membrane and the newly formed cells during cycle 14. Since the vitellin membrane is a static tissue throughout development, cauterised cells are made immobile. The main goal of the experiment is to take advantage of the fact that the system can perform damage anywhere in 3D in order to better understand the underlying mechanical properties of the embryonic tissue, during the event of gastrulation, in a global level: is it possible to cauterise tissue at different depths? What are the effects observed at the region of cauterisation? How does the whole tissue behave if parts of it cannot participate in the coordinated movement?

Methods

Drosophila embryos with GAP43-mCherry membrane marker were provided by the lab of Maria Leptin at EMBL Heidelberg. Embryos were caged and regularly plated so that clear staging could be achieved. Mounting procedure was carried out following published methods [4]. Fluorescence imaging was performed right after cauterisation with MuVi-SPIM, using 591 nm with 160 µW on each illumination direction[2] and 40 ms exposure time, during time-lapses of ca. 15 minutes. Infrared laser powers used were kept around 400 mW - yielding a power density of around $23.5 \cdot 10^6$ W/cm^2 at the focus - and exposure times in the order of 40 ms. As discussed in sectio 1.6, a cumulative thermal effect of the infliction of many fs should lead to temperature increase and the corresponding stitching of the different tissues. All regions of ablation used consisted of pre-defined lines which were scanned automatically by the 2D steering galvanometric mirror system. Right after image acquisition was completed, the capillaries were removed from the microscope, the embryos removed from the embedding gel and prepared for cryo-electron-microscopy (cryo-EM) imaging through deep freezing. Cryo-EM imaging was performed at the electron microsopy facility at EMBL Heidelberg. The idea behind cryo-EM imaging was to be able o have detailed information of how the cauterised regions change in respect to the surrounding tissue.

[2] Here, and throughout all examples, the illumination laser powers were measured at the back aperture of the illumination objectives.

Results

Figure 4.4 shows two different cauterisation lines performed in the same embryo at different tissue depths, namely 4 µm and 12 µm, just three minutes after the onset of ventral furrow formation. Figure 4.4a presents and unrolled [4, 152] view of the embryo, where the entire three-dimensional surfaced is mapped onto two dimensions using cylindrical coordinates. Ventral (V), dorsal (D) and the lateral sides (lateral right and left, depicted as LR and LL) are correspondingly marked. A cross-section performed along the dashed white line is presented in Figure 4.4b. From this perspective, it seems that the cauterisation performed at 12 µm depth does not reach the most apical part of the cells, whereas at 4 µm depth the region between both membranes is clearly affected. Cryo-electron microscopy cross-sectional data reinforces this assumption: tissue welding at shallow depths creates a particular negative curvature on the outer part of the embryo's membrane, which is not observed on the other inflicted area. Additionally, in both cases darkening of the tissue is observed, an effect usually seen due to volumes with higher electron densities.

The effect of this perturbation is seen during gastrulation, as a natural furrow becomes difficult to be formed. Moreover, tissue cauterised further inside, away from direct contact to the vitelline membrane, is freely moving, as can be seen in Figure 4.5. With this tool it is possible to gain a dynamic understanding of the mechanics of furrow formation, since it is viable to use it in the context of probing e.g. the rigidity of a certain group of cells, or even their importance on the formation of the furrow itself [152]. This technique can also be extended for generating tissue responses during other developmental stages, such as germband extension. In this case, perturbation during the time when cells stretch and intercalate in order to enable the rapid extension movement can provide information on the importance of junction growth for the more global movement of convergence-extension [153].

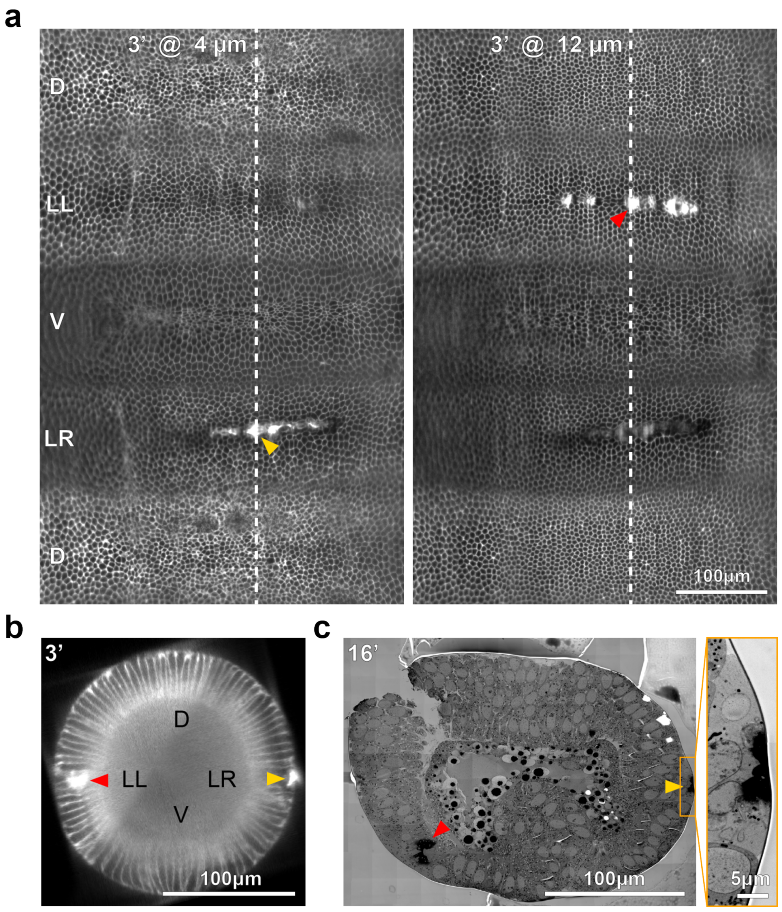

Figure 4.4: Tissue cauterisation. (a) Unrolled view at 4 µm depth (left panel) and at 12 µm depth (right panel) from the surface of a Drosophila embryo on which two cauterisation lines were performed, marked with yellow and red arrows. Timing of cauterisation corresponds to 3 minutes after ventral furrow onset. **(b)** Cross-section view of the embryo along the dashed line in (a). **(c)** Electron-microscopy images of the embryo in (a) deep frozen after 13 minutes from onset of gastrulation. The right panel shows a zoom-in of the cauterisation region performed on the right side of the embryo.

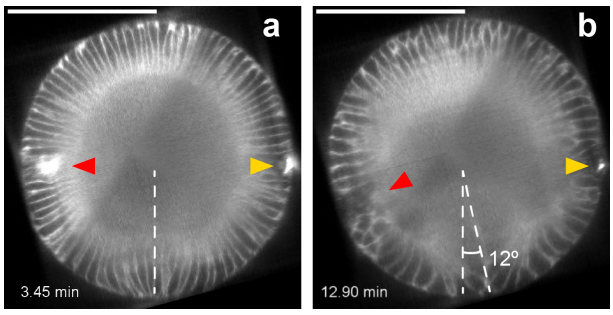

Figure 4.5: Gastrulation timelapse with double cauterised tissue. Cross-sectional view of the same *Drosophila* embryo as in Figure 4.4 with two cauterisation lines, with color code as previously defined. 13 minutes after onset of gastrulation, the ventral furrow line is shifted by roughly 12° towards the lateral side where cauterisation close to the vitelline membrane has been performed. Scale bar represents 100 µm.

4.2.2 Deep tissue photodamage

After fertilization and fusion of both the nuclei of the sperm and the egg cell (pronuclei), the *Drosophila* embryo undergoes a series of rapid and synchronous mitotic divisions, each of them termed *mitotic cycles*, or simply *mc*. These divisions follow a spreading of their positions along anterior-posterior axis, changing from a rather spherical to an ellipsoidal occupation of yolk space (up to mc4), and moving outwards towards the outer shell (from mc5 to mc9), with all nuclei having reached the cortex at mc10 [142].

Early pre-blastoderm studies of embryos have focused primarily on the role of cytoskeleton machinery, Bicoid and zygotic expression levels [154–158]. Although there is evidence that not all nuclei manage to make it to the cellular blastoderm stage right after gastrulation, little is known about the dynamics governing nuclei that stay behind. Experiments focusing on early nuclei damage can provide insight e.g. on the embryo's repair machinery, as the damaged nuclei should most likely not be able to participate further in the development. What are the dynamics involved in this process? What happens to them, are they removed, do they simply get degraded on site? Are there any characteristic dynamics involved? In order to take advantage of the increased penetration depth due to the longer wavelengths, we decided to test the performance of the new system by photodamaging nuclei deep inside the *Drosophila* embryo at early syncytial stages of development - i.e. before mc10.

Photodamage deep inside the tissue needs to be carefully tuned in order to avoid creation of large cavitation bubbles. Higher powers and shorter exposure times per ablation assured that only the selected nucleus is be damaged, with no direct effect on the first neighbours. The main goal was to be able to ablate a specific nuclei in a very localized fashion and observe their trajectory throughout the following division rounds. Multiview imaging was performed with a commercial fly line which expresses His2Av-GFP and mRFP-tagged nucleoporin (Nup) 107 (first published in [159]). Nups are proteins which make up the nuclear pore complex (NPC), a channel responsible for nucleocytoplasmatic transport, i.e. they promote transport from molecule in and out of the nucleus. Since the nuclear membrane has usually many NPCs, the fluorescent signal is distributed all over its surface so that a heavily faint and blurred broad signal can still be detected at large tissue depths. Other markers, such as histone tags, are spatially too localized and in much smaller numbers to provide enough fluorescent signal to overcome scattering.

Methods

NUP107-mRFP and His2Av-GFP *Drosophila* embryos were caged and agar plates collected every 30 minutes. In order to have proper embryo staging for each collection, only plates after 3 collections were utilized for imaging. The mounting procedure was carried out following published methods [4]. Two dual illumination and dual detection stacks at 0 and 90 degrees sample rotation were acquired in widefield mode every 90 seconds. Exposure time for each plane was 50 ms. In order to minimize phototoxicity and increase imaging speeds images were taken at 3 µm steps. Illumination laser powers were chosen such that further increase would only lead to stronger background signal, leading to 160 µW on each illumination path (measured at the back aperture ot the illumination objectives.). Nuclei ablation was performed punctually, by exposing each target an average of 4 times with 800 mW, each point ablation with an exposure of around 15 ms.

To test whether our imaging conditions would be toxic for normal embryonic development, we checked for the mitotic cycle timings, and found that all embryos underwent the first recorded round of division (mc7-mc8) in less than 10 minutes, with slow increase in division times, as expected from known literature [154, 155, 157].

Results

Figure 4.6 presents one example of a nuclei ablation experiment in a *Drosophila* embryo at mc7, i.e. when the embryo has 64 nuclei. In-plane (xy) projections allow better global visualization of the localization of these nuclei with respect to its neighbours, with all 4 ablated nuclei marked in red. As can be seen, two ablated nuclei show very strong fluorescence, with the other two presenting no visual alterations. This corresponds to a typical experiment scenario: the formation and subsequent recession of a small cavitation bubble after exposing a nucleus to the infrared pulses usually creates a small volume with higher fluorescence emission; other shot nuclei may not show such effects, even though ablation was performed with the same parameters and at basically the same tissue depth. One possible explanation for this is that for such punctual interactions with high laser powers the local molecular distribution plays a very strong role in the way absorption effects occur in the ablated volume, and leading to different reactions in varying regions of the embryo.

Another interesting aspect observed is an indirect effect of the abalted nucleus to its neighbours. Although no direct damage has been inflicted on the

neighbours, subsequent divisions show a different behaviour in respect to other healthy nuclei, with unusually fast and large movements of the daughter nuclei after division, ultimately leading them also to the inner part of the yolk. It is conceivable that damage to the cytoskeletal meshwork around the chosen nuclei could influence its neighbours, as suddenly they become less bound to the meshwork and may move more freely. This creates a rather larger hole in the system of nuclei-cytoskeleton, probably being recognized as a damaged zone by a possible regulatory machinery.

The average depth from the vitelline membrane at mc7 was observed to be 40 µm; at the end of mc7 nuclei have an average distance of 27 µm, which corresponds to previous works [157]. Out of the four ablated nuclei, two have been selected and followed throughout the specified timepoints, within 20 µm range cross-sectional projections (Figure 4.6a-b). In this kind of representation a clear retraction of the ablated nuclei to the center of the yolk can be noted, meaning that they never reach the surface to be part of the syncytium shell. In all 5 embryos tested, meaning a total of 19 ablated nuclei, only two reached the surface, corresponding to a 90 % effectiveness in ablation processes. All others behaved in similar manner, ultimately going to the center of the yolk. Comparative graphs showing absolute distance to the vitelline membrane of unperturbed and shot nuclei is given in Figure 4.7. This is an interesting result, as so far there has not been any insight on how damaged nuclei behave throughout blastoderm stages. Although it is known that at the time nuclei reach the surface some stay behind, whether there is a direct correlation to whether these nuclei are somehow damagedwas unknown. This is the first time that controlled localized nuclei damage infliction leads to an inward movement of these nuclei into the yolk. Also, it appears that even damaged nuclei can stay in the center of the yolk for long periods of time after ablation has been inflicted, and are not directly dissociated.

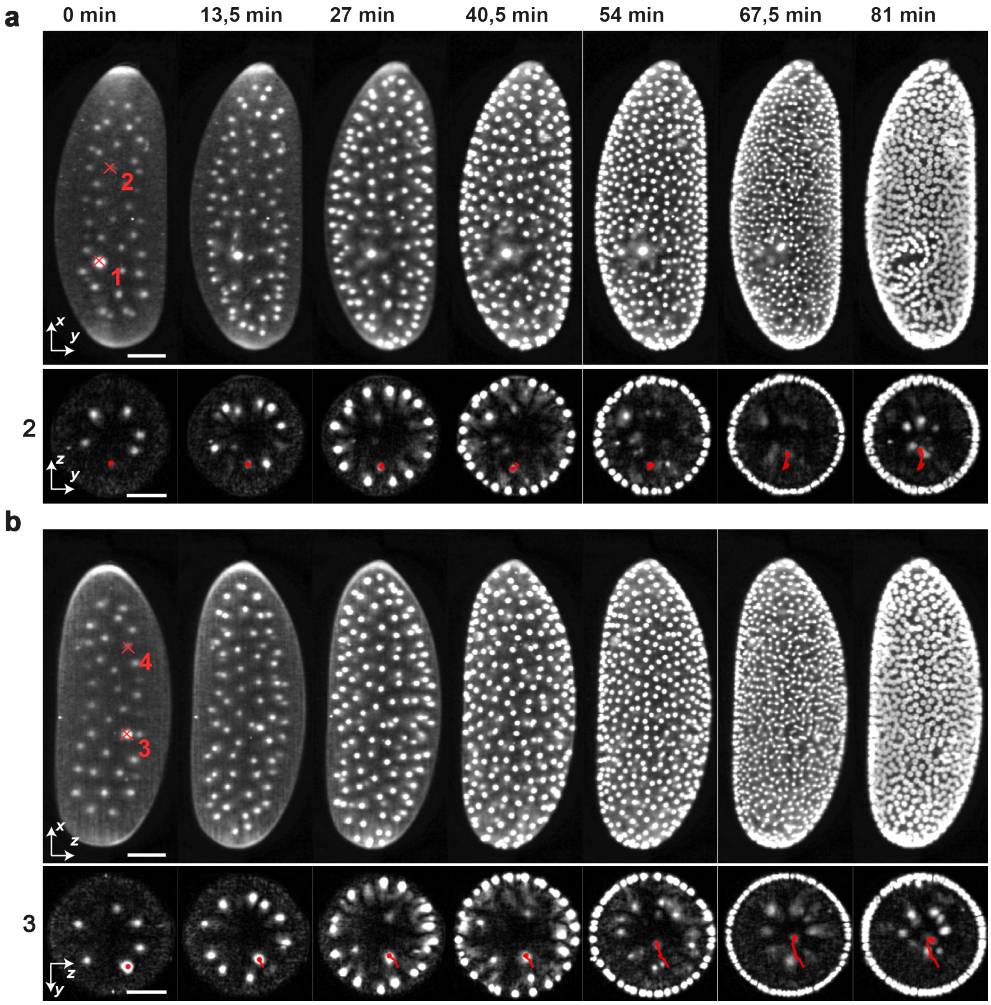

Figure 4.6: Deep tissue ablation of single nuclei in early *Drosophila* embryo. Embryo at mc7 (64 nuclei) expressing NUP107-mRFP. **(a)** 0 and **(b)** 90 degree views with in plane (xy, xz) projections which provide a more global view on the embryonic development throught the first 81 minutes after ablation. The lower rows show cross-sectional (zy) projections of a 20 µm slice range around the selected ablated nuclei for the same selected timepoints. Tracking of the positions in red show that ablated nuclei move inwards, close to the center of the embryo, never reaching the surface. Scale bars: 50 µm.

It is important to note that even with reduced scattering, interactions in such large penetration depths can only be achieved with strong increase in laser powers. Since our system can at maximum deliver 810 mW on the back aperture of the objective, we noticed great difficulty in being able to perform any damage in nuclei at mc6 and earlier.

With these experiments we show for the first time that it is possible to perform localized damage at an average depth of 35 µm deep inside the yolk of live developing *Drosophila* embryos, and to record the embryo's response *in toto*. Through this kind of perturbation and imaging it is possible to gain more

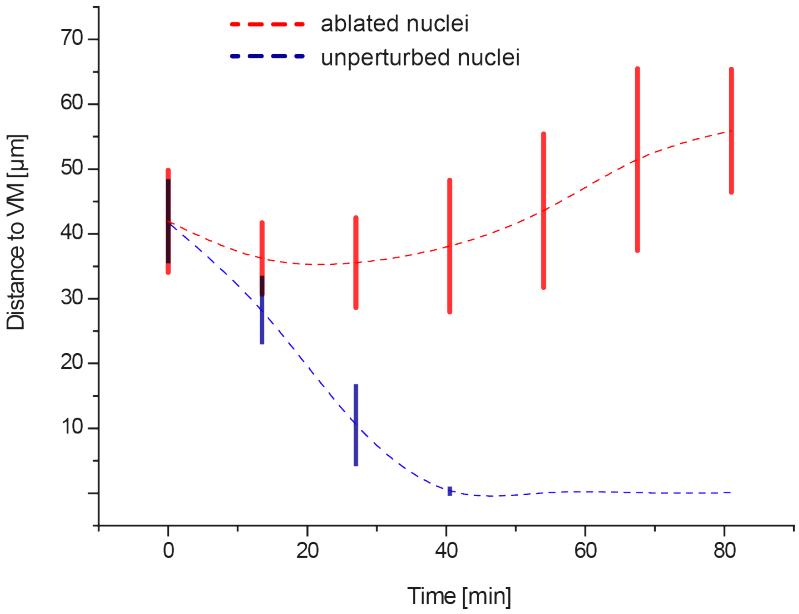

Figure 4.7: Average movement of ablated and healthy nuclei from different *Drosophila* embryos. Spline curves with standard deviation error bars of 17 ablated and healthy nuclei of 5 different embryos. Healthy nuclei were selected randomly. The rather large deviations on healthy nuclei reflect the observed variation on general initial offset distance to the vitteline membrane.

information on a new embryonic repair machinery, which functions via drag of damaged nuclei to the center of the yolk: this way they are not part of the syncytial blastoderm, which ultimately provides the embryo with important protection against gastrulation malfunction.

The data presented here is just one example. We believe that this can be an important tool not only for further experiments in early embryo scenarios, but also for probing specific tissue formations in post-gastrulation embryos, e.g. during midgut or muscle closure events (at around and 13 hours AEL, respectively), which mark important developmental milestones and should be tightly regulated. Localized photodamage with pulsed fs infrared laser light is capable of perturbing these highly controlled subsystems, and together with further biochemical tests and analysis may provide a more complete picture on the mechanisms behind the scences.

4.2.3 Towards single neuron ablation

In order to evaluate the ablation system's capabilities in other model organisms, we decided to perform experiments in the young Zebrafish brain, with focus on microglia response. Microglia are tissue-resident macrophages of the brain, and have many important roles in its development and maintenance in a healthy. They are known to have active contributions in phagocytosis

of apoptotic neuros, neurogenesis and axonal growth, synaptic refinement, vessel patterning, immune surveillance and injury response [3]. Our main interest was to perform highly localized photodamage experiments to induce microglia activation and observe its response. There have been many works performed with traditional confocal microscopy, where large area ablations have shed light on microglia dynamics upon brain injury (for example [161]). However, by performing single soma ablations and single axon cuts we generate perturbations which better mimic more natural situations, as microglia are also known to engulf apoptotic neurons and prune axons in natural circumstances. In addition, we tested the system for volumetric imaging of Ca^{2+} waves upon localized injury.

Methods

Zebrafish embryos were provided through a collaboration with the lab of Francesca Peri from EMBL Heidelberg. For the two first rounds of experiments, lines expressing synaptophysin in green (Synaptophysin-sfGFP)[4] with microglia marked with pu.1-RFP (which also marks other macrophages) were used, whereas for calcium imaging β-actinGCaMP6s-GFP was preferable. The average embryo age was of 4 days post fertilization (dpf). Different laser settings were utilized depending on the experiment, and are presented throughout the explanation of each experiment.

Results

Single soma photodamage. First we looked for two neighbouring soma, ablating one of them in order to check for any effects on its neighbour. Dashed lines in Figure 4.8a show the region of interest for the ablation experiment, localized near the right optic tectum, with the two neuronal bodies localized ca. 80 µm deep inside the brain. In their proximity was a microglial cell, at around 23 µm distance, shown in yellow. Figure 4.8b presents some selected timepoints of the entire recording: the first image is taken before ablation, with the ablation moment lying in between the first two frames, and is represented with a red vertical line.

Ablation settings utilized were 880 mW and 9 ms exposure time for each

[3] Readers interested in more detailed information about the origins and multitasking roles of microglia are invited to consult a recent review from A.M. Casano and F. Peri [160].

[4] This is called NBT::ΔLexPR:Syp-sfGFP - a neuronal beta tubulin promoter with an enhancer (lexPR-lexOP system) followed by the synaptic vesicle synaptophysin marked with super-folder GFP fluorophore.

point-like ablation. In total, 5 exposures were performed, until the effect of a small cavitation bubble inside the cell body could be observed. The near microglia is seen to arrive at the injury site around 20 minutes after ablation. The corresponding cell rear retraction velocity was of ca. 3 µm/ min. It is worth mentioning that throughout the entire timelapse, the neighbouring cell body remains fluorescent, with no apparent damage; the active microglia also shows no response to it; neither do other microglia reach for it. This corroborates with the assumption that only a single soma has been damaged.

Axon cut. As a second step, the ablation of single axons was performed, in order to qualitatively test the localization precision of the ablation regions. For this the synaptophysin line shows itself very useful, as its patch-like expression highlights particular axons with strong contrast. The region of ablation is depicted with dashed lines in Figure 4.8c, and in Figure 4.8d we present the timelapse recording in analogous fashion to the one described above. Infrared laser powers were 604 mW with 3 ms exposure time for a single ablation, with the spot of ablation located ca. 65 µm deep inside the tissue, near the right optic tectum. An interesting effect observed after ablation was the detection fluorescence signal at the ablation spot (where initial fluorescence was seen in the sfGFP emission spectrum) in longer wavelengths, namely through the 594 nm long-pass filter used for the microglia channel. This can be a related effect as the one observed during the deep tissue ablations in *Drosophila* presented before: the photon energy transfer to loosely bound electrons allows them to gain kinetic energy and to dissociate from the molecule, leaving open bonds which can be reformed in new ways with different surrounding molecules. It is conceivable that these new (and possibly larger) compounds may fluoresce in other parts of the spectrum, especially towards longer wavelengths. A total of four microglia were recruited to the damaged site. Taking into account their relative distances to the ablation point, and observing the rear cell retraction time, an average of 3.2 µm/ min was found. Together, both experiments yield an average of 3.18 µm/ min cell rear retraction velocity, which agrees with previous studies [161].

These examples can be of interest for better understanding of the way microglia engulf single damaged soma. Furthermore, it can shed light on the main behaviour behind axonal pruning and rearrangement, even regrowth, as the possibility to cut single axons allow an in-depth view of the behaviour of microglia under more natural conditions [162–164].

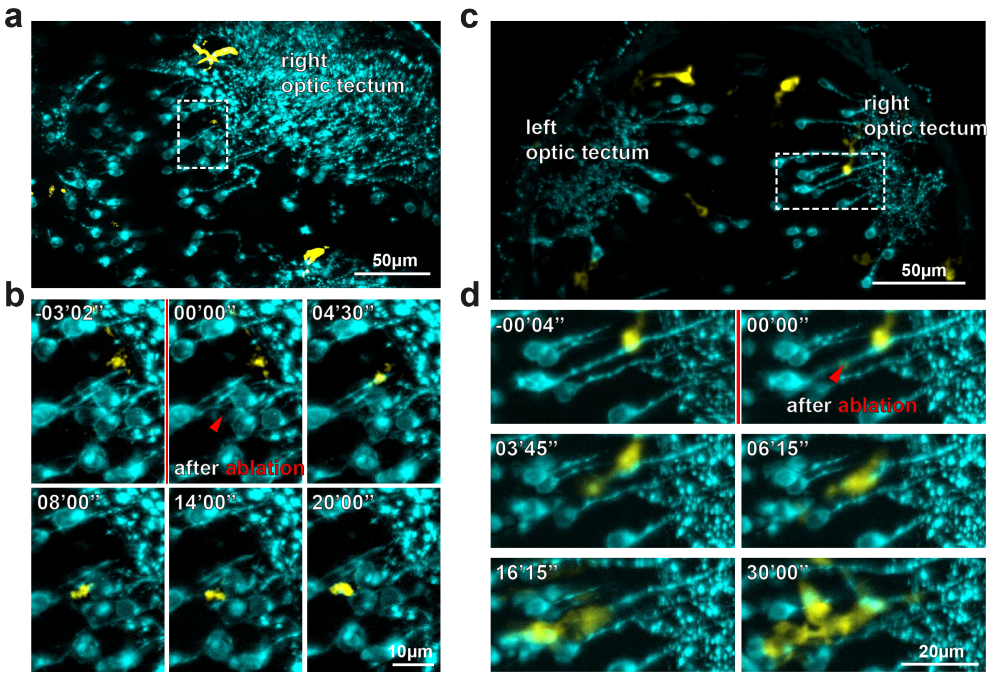

Figure 4.8: Single soma and axon cuts inside the Zebrafish brain expressing Synaptophysin-GFP. (a,c) Maximum intensity projection of a large field of view encompassing the ablation volume, depicted in dashed lines. **(b)** Timelapse of single soma ablation, where the neighbouring neuron remains intact. Not only the Synaptophysin signal is decreased, but also a microglia is seen to interact with the ablated soma, reaching the region from around 22 µm distance. **(d)** Timelapse of single axon cut, with four microglia arriving at the site from different distances. An average microglia body retraction velocity of 3.2 µm/ min corresponds well with other studies [161].

Calcium imaging. A last experiment in Zebrafish was devoted to producing recordings which can be fast enough to image the volumetric spread of calcium through single neuron damage. Calcium spread can also be observed in natural conditions, or under the influence of chemicals. There are also many works reporting calcium activity after tissue photodamage; these studies, however, heavily rely on large damaged volumes, which encompasses many different neurons [161]. With the ablation system in MuVi-SPIM, however, we aimed at minimizing the inflicted volume, in order to observe how calcium spreads from a single neuron after photodamage. The selected region for ablation, near the right optic tectum, is shown in Figure 4.9a. A sequence of fast in-plane acquired images depict the first 1.5 seconds of calcium spread during tissue response after ablation. More information can be accessed through volumetric imaging, presented in Figure 4.9b. Here a timelapse after ablation (symbolically shown as a vertical red line) presents the calcium spread in the tissue, reaching the division line between left and right brain hemispheres, and not propagating further. It is interesting to note how signal propagates in an almost stepwise manner, with neighbouring patches of neurons lighting

up at different moments. This effect could be related to the direct connections /connectome from the ablated neuron. Calcium signal spreads over the whole part of the field of view corresponding to the right brain hemisphere; no signal appears from the left side, with the midline highlited by a dashed line, as expected from previous studies [161]. The propagation of the calcium signal was measured to be around 10.6 µm s^{-1}, which is in good agreement with other known values [161].

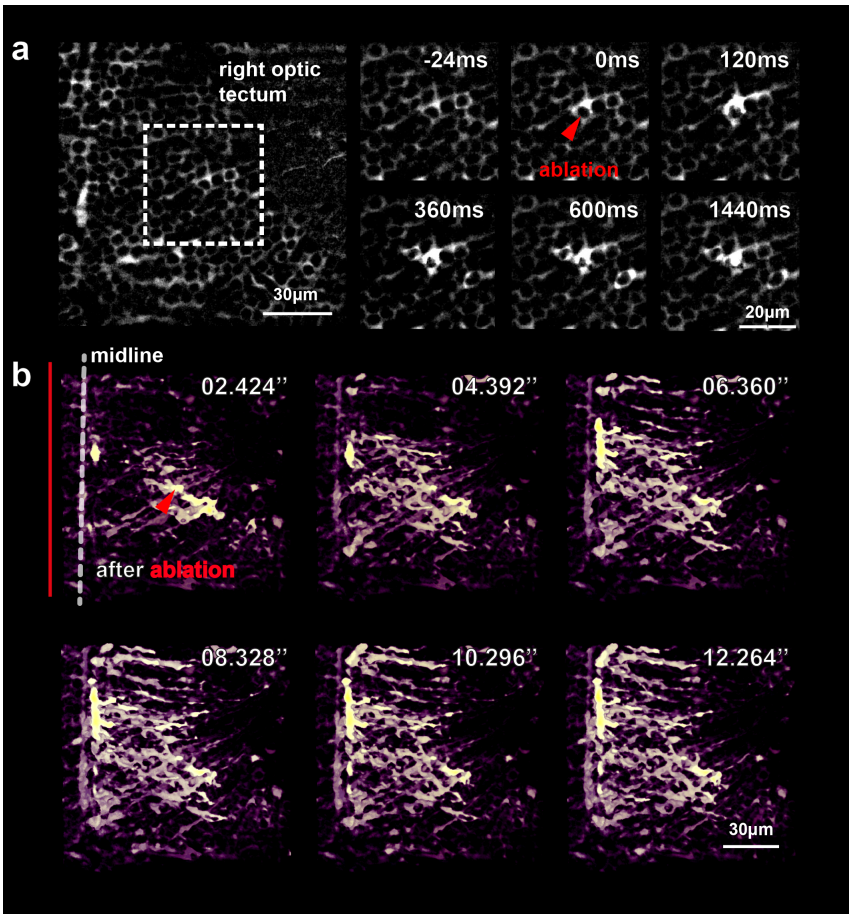

Figure 4.9: Fast calcium imaging of single neuron ablation in 4dpf Zebrafish brain. Embryo expressing $\beta - actinGCaMP6s$. **(a)** Large field of view of ablated region, depicted with dashed lines. A short timelapse is shown on the right, with 0 ms denoting the recorded image closest to the ablation experiment. **(b)** Longer timelapse of a 130x130x40 μm^3 volume around the ablation spot after ablation has been performed. The separation from left-right brain volumes is clearly seen, with the lack of calcium activity being noticed on the other side.

Overall, the young zebrafish brain is an interesting system for testing single neuron damage reactions inside the brain. The coupling of ablation experiments with drug treatment, for example, can be of particular interest, since the infliction of damage in such small scales allows the embryo to continue

normal development for the following days. Furthermore, small scale damage in areas known to be devoted to particular abilities, such as sight or fin locomotion may open new ways to study behaviour and the connection to particular brain subunits.

4.3 Discussion

Throughout the entire chapter we used fs pulse widths with MHz repetition rates. As we discussed in Section 1.6, thermal diffusion occurs in longer timescales than a couple of μs, which would correspond to the MHz repetition rates. This effectively means that each pulse arrives at a slightly hotter tissue, leading to an accumulative effect of thermal total deposited energy. This is the main reason why for the cauterisation experiments we utilized longer exposure times (around 40 ms), while maintaining higher powers and much shorter exposure times for all other examples. In fact, all other examples relied on single point ablation experiments which happened whithin seconds from each other. This ensures a much stronger thermal effect during cauterisation experiments whereas each ablation is more likely to deliver more confined interactions due to the shorter timescales.

On the hardware side, the infrared laser system is flexible and can be adjusted to fit any existing light-sheet setup with only small modifications required. Nonetheless, the fine control of the amount of pulses delivered into the tissue could be especially advantageous to cope with situations where the accumulation of thermal energy and the subsequent creation of bubbles needs to be tightly controlled. One way to achieve this is through the addition of an optical element to control the repetition rate of the Mikan laser (such as an optical chopper). Yet another approach would be the replacement of the rotation stage for rotation of the $\lambda/2$ waveplate with a *Pockels cell*, which can be driven with frequencies of up to MHz, matching the laser's specifications.

For the control software, the calibration of the 2D galvanometric mirror system still needs to be performed before each new experiment, in a semi-automatic way. This is a repetitive task, which takes time and can be prone to simple errors. Full automation of this procedure in a future version of the control software can not only improve the systems' performance, but also allow the entire focus of the user towards the experiment itself. The same applies for the rotation stage calibration of the $\lambda/2$ positions for laser power control.

Infrared pulsed lasers can be used for a wide range of photomanipulation experiments. The long wavelength, along with the short pulses and high power densities allow the infliction of damage deep inside highly scattering

tissues in a controlled spatial and temporal way. Close to the surface, it is possible to tune the system's parameters in order to have lower powers and generate other effects in the tissue, such as cauterisation. Together with multiview light-sheet microscopy, the whole system is capable of recording fast biological responses such as the calcium wave spread due to minimal damage infliction. Furthermore, it permits the imaging of tissue responses over larger time scales, encompassing both *in toto* and *in vivo* imaging pre-requisites towards a highly controlled minimally invasive laser-tissue manipulation and imaging method.

Conclusions and perspectives

This thesis focused on presenting three different techniques which aim at the reduction of light scattering and absorption during image acquisition and photomanipulation in light-sheet microscopy.

The combination of multiview light-sheet microscopy with especially developed electronic confocal slit detection (eCSD) for multiview light-sheet imaging allows microscope setup to have a similar degree of confocal imaging capabilities as that of a confocal epifluorescence microscope. We have shown that the combination of confocal slit detection with multiview imaging enables the possibility to perform direct fusion methods, resulting in less amount of necessary acquired data and easier post-procesing steps such as deconvolution of multiview datasets. As in any microscope setup, different detection magnifications can adapt the FOV of the microscope to better fit different specimen sizes (*cf*. Section 1.2.2). One interesting improvement to MuVi-SPIM with eCSD would be the inclusion of zooming optics which could be motorized and controlled via the microscope software. Upon change of magnification, the microscope software could automatically recalibrate the electronic confocal slits either according to pre-defined calibration tables or by performing the full calibration procedure again. This would save time and increase the flexibility of the imaging setup one step further.

After improving the ability to shift light detection towards photons with primarily ballistic character, increased penetration depth for imaging of live samples was presented utilizing infrared fluorophores. With these wavelengths, light emission is shifted towards the ballistic regime, as less scattering can be expected with longer wavelengths. Gut organogenesis and other deep tissue processes could be observed with clear signal during development of *Drosophila melanogaster*. Although more experiments are required for an in-depth study of particular timepoints, the comparison with fly lines expressing different fluorescent markers shows promising trend, with e.g. the pole cells being recognized after yolk internalization for the first time only using with infrared wavelengths. One interesting analysis would be to compare flu-

orescence data with known high resolution images of fixed samples (with e.g. electron microscopy) [142], and generate a map which relates the known data with specific timepoints of the long-term recording. In addition, crossing the created histone-labelled fly mutant with other fly lines which have fluorescent markers for specific cell fates (such as for the germline) will further ease the recognition of certain cells of interest inside development, as the histone signal becomes very crowded especially at later stages. Another further step is to utilize the infrared marker with other model organisms, such as *c.Elegans* or zebrafish for other the observation of specificly challenging morphogenetic events (e.g. gastrulation, organogenesis), following specific migrating cells through development (e.g. microglia) or for studying the difference in organ function in mutants.

Along with imaging the entire embryonic development at greater depths, photomanipulation using infrared lasers allow localized damage infliction deep into the tissuet. The ability to perform such laser-tissue interactions was presented in the last chapter, with the development of a stable infrared laser ablation setup which has the potential to be be fully incorporated in any light sheet setup. In our implementation in MuVi-SPIM, through three examples we showed three different photoablation experiments that could be performed with the system, each of them motivating a particular characteristic of the setup: its depth penetrance, speed, and high photodamage localization. Nonetheless, although all the experiments shown could be reproduced, the usage of high power lasers implies on the formation of non-linear effects which, due to the high photon densities, can lead to unstable results if the system is not properly calibrated or if some of the optical properties of the sample of study cannot be estimated. One way to minimize this is through an overall automated calibration procedure which can more reliably optimize the creation of a diffraction limited on the focal plane.

Light-sheet fluorescence microscopy has already completely changed the way living samples can be observed, by combining very good optical sectioning with dedicated sample mounting, which dramatically decreases phototoxic levels thereby increasing specimen survival rates. Modern light-sheet microscopes are fast and have full *in toto* imaging capabilities. This is however not enough: the combination of novel techniques, such as the ones here presented, are vital towards achieving a more global view of entire living tissues, even at great tissue depths, while preserving the basic characteristics of SPIM imaging.

Nature hides itself with an entire toolbox of effects; the biggest challenge is to use the same set of tools to unravel more of it.

Appendix A

the Beam-slit unit

In traditional confocal microscopy, the degree of confocality is measured in Airy units. It stems from the observation that an infinitesimal point source imaged through a lens will produce a particular diffraction pattern, also known as Airy pattern. Airy units are useful in order to choose the size of the confocal pinhole used for discriminating scattered light: one Airy unit corresponds to the radius of the first dark ring of the Airy function, i.e. the distance from the center of the major peak to the first minimum (*cf.Section*1.2.2).

Likewise, it is useful to define an analogous length scale for confocal light-sheet microscopy. Due to the differentiated light paths for illumination and detection in light-sheet setups, a slit, rather than a pinhole, is the necessary geometry for achieving a certain amount of confocality into the imaging system. Here, the only variable is the number of pixel lines which make up the active slit part of the camera sensor, instead of the pinhole radius. This number, which can be translated from pixels to µm by multiplication with the real pixel size of the detection camera, has to be related to a specific aspect of the illumination or detection optics. In MuVi-SPIM setups the illumination scanning beams have overlapping optical axes, and are offset from each other by a Rayleigh range: this way a virtually longer scanned light-sheet is created. We have thus defined a slit width corresponding to the width of each beam ($1/e^2$) at the Rayleigh range as a *Beam-slit* unit.

We have observed that slit sizes smaller than this value usually lead to a loss in signal, without necessarily an increase in contrast; values much above allow the confocal slit to detect significant higher amount of scattered light, decreasing overall image contrast as well. A comparison of contrast values for different slit sizes is presented in Section 2.1.

Appendix B

eCSD calibration calculations

Calibration of the positions of the electronic slit in order to properly follow the image of the scanned beam is a crucial step towards appropriate eCSD aquisition. It has to be done for each camera separately, so that slight optical misalignments can be compensated for. As presented in Section 2.1, calibration follows the mapping of voltage traces given to the galvanometric mirror (galvo) into pixel line positions on the camera sensor, as presented in the calibration paragraph of Section 2.1. These pixel lines should best represent the maximum of the gaussian profile of the illumination beam at a certain position. The voltage traces given to the galvo on the other hand represent all the different stages for a full cycle movement, as depicted in Figure 2.5. In order to calculate the transformation function M_b which maps voltages to pixels, it is important to first solve the equations of motion for the galvo, in order to express the voltage values corresponding to the linear part ot the motion in terms of the given amplitude V_{amp} and the turn time percentage α, which corresponds to the percentage (usually 10%) of the full exposure time τ_{exp}, given to the accelerating/decelerating motions combined. here we will go in more detail about the main calculation steps needed for calculating ν_{act}, τ_{line} and τ_{camera}.

The galvo starts at a certain maximum voltage $V_{max} = V_{off} + V_{amp}$ and accelerates until reaching a constant velocity regime, following Figure 2.5. The acceleration contributions is given by:

$$V_{acc} = \frac{1}{2}\nu_{lin} \cdot \tau_{\alpha}\,,$$

and the linear part by

$$V_{lin} = \frac{1}{2}\nu_{lin} \cdot \tau_{exp}(1-\alpha).$$

Here, $\tau_\alpha = 1/2\,\alpha\,\tau_{exp}$. If we sum all the voltage contributions we have $V_{amp} = V_{acc} + V_{lin}$, and solve it for ν_{lin} we arrive at:

$$\nu_{lin} = \frac{4|\kappa_1 \cdot V_{amp}|}{\tau_{exp}(2-\alpha)},$$

with $\nu_{lin} = \nu_{act}$, the activation front velocity presented in Chapter 2. Also, $\tau_{line} \cdot \nu_{act} = b$ is the slit width. Therefore, since b is given by the user, τ_{line} is directly known.

To calculate the delay time τ_{camera}, we need to take into consideration the waiting time for acceleration τ_{alpha} plus the time needed for linear movement outside the field of view of the sensor. Furthermore, in order to ensure that the beam is in the center of the electronic slit from the beginning, subtraction of the time corresponding to the movement of half a slit width is also needed. Taking all these contributions together we arrive at:

$$\tau_{camera} = \left(0.5\alpha \cdot \tau_{exp} - \frac{l_{lin}}{\nu_{act}}\right) - \frac{1}{2}\tau_{line}, \quad \text{with} \quad l_{lin} = \kappa_0 + \kappa_1 \cdot V_{lin}.$$

Simultaneous dual illumination is achieved by taking one galvanometric mirror as reference and performing a linear adjustment on the voltages for the second mirror through a constant γ. The adjustment constant is calculated through the ratio of a known displacement δV_{ref} on the reference mirror and manually adjusting the corresponding voltages for the second (δV_{map}):

$$\gamma = \frac{\delta V_{ref}}{\delta V_{map}}.$$

Appendix C

Scattering effects and eCSD

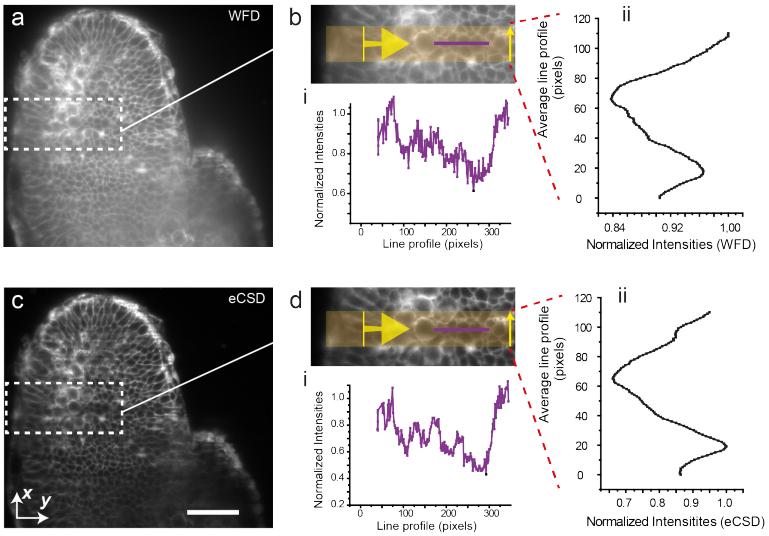

Figure 4.10: Scattering effects: stripes. Due to the optical geometrical arrangement for illumination and detection paths, light sheet microscopy suffers from artifacts produced by scattering effects on the sample. Some of these effects can generate areas of shadow creating striped patterns of uneven illumination8. In general, scattering of the emitted light tends to mask striping artifacts. As confocal detection removes the scattered light, stripes can become more apparent. However, they are also present in the widefield image. Here we analyze the data displayed Figure 4c. Reproduction of WFD (**a**) and eCSD (**c**) acquired images from Figure 4 with the same region highlighting a stripe artifact. The stripe artifacts can be noted from the marked dip in the average projection shown in (**b,d ii**) (from yellow box region, big yellow arrow represents the direction of the average projection on all columns. The average column is then plotted upwards, as indicated by smaller yellow arrow). Please note, that the dip is deeper in the confocal case, however, the signal-to-noise along the stripe (purple line) is still higher (**b,d i**). Scale bar is 50 μm.

Scattering in tissues often lead to inhomogeneous distribution of illumination photons, as larger structures generate shadows through illumination direction. In traditional confocal and widefield microscopy this is not particularly visible, as illumination and detection share same optical axis. In light-sheet microscopy it is possible to see full extent of these effects as the illumination direction stands oftentimes perpendicular to detection. Furthermore, since eCSD blocks the majority of scattered photons, shadowing effects be-

come more clearly visible. An example using dual illumination can be seen in Figure 4.10. Depending on the case of study, such effects can make recognition of tissue features a more demanding task, since the enhanced intensity inhomogeneities with overall signal reduction can create confusion on discerning structures from background.

Publications

Various aspects of the work presented in this thesis, and performed between the years of 2012 and 2016, are now part of the following publications:

Gustavo de Medeiros, Nils Norlin, Stefan Gunther, Marvin Albert, Laura Panavaite, Ulla-Maj Fiuza, Francesca Peri, Takashi Hiiragi, Uros Krzic, and Lars Hufnagel. "Confocal multiview light-sheet microscopy." *Nature communications*, 2015. [78]

Petr Strnad, Stefan Gunther, Judith Reichmann, Uros Krzic, Bálint Balázs, Gustavo de Medeiros, Nils Norlin, Takashi Hiiragi, Lars Hufnagel, and Jan Ellenberg. "Inverted light-sheet microscope for imaging mouse pre-implantation development." *Nature methods* 13, 2016. [56]

Patrick Hoyer, Gustavo de Medeiros, Bálint Balázs, Nils Norlin, Christina Besir, Janina Hanne, Hans-Georg Kräusslich , Johann Engelhardt, Steffen Sahl, Stefan W Hell and Lars Hufnagel. "Breaking the diffraction limit of light-sheet fluorescence microscopy by RESOLFT." *Proceedings of the National Academy of Sciences* 113, no. 13, 2016. [61]

Gustavo de Medeiros, Bálint Balázs, and Lars Hufnagel. "Light-sheet imaging of mammalian development." *In Seminars in cell & developmental biology*, vol. 55, pp. 148-155. Academic Press, 2016. [48]

Bibliography

[1] Galileo Galilei and Stillman Drake. *Dialogue concerning the two chief world systems, Ptolemaic and Copernican*. Random House Digital, Inc., 1953.

[2] Terry F Hoad. *The concise Oxford dictionary of English etymology*. Oxford University Press Oxford, 1993.

[3] Robert Hooke. 1665 micrographia. *London: Martyn and Allestry*, 2003.

[4] Uros Krzic, Stefan Gunther, Timothy E. Saunders, Sebastian J. Streichan, and Lars Hufnagel. Multiview light-sheet microscope for rapid in toto imaging. *Nature Methods*, 9(7):730–733, 2012.

[5] Martin Chalfie. Green fluorescent protein as a marker for gene expression. *Trends in Genetics*, 10(5):151, 1994.

[6] Mikhail V Matz, Arkady F Fradkov, Yulii A Labas, Aleksandr P Savitsky, Andrey G Zaraisky, Mikhail L Markelov, and Sergey A Lukyanov. Fluorescent proteins from nonbioluminescent anthozoa species. *Nature biotechnology*, 17(10):969–973, 1999.

[7] Xiaokun Shu, Antoine Royant, Michael Z. Lin, Todd A. Aguilera, Varda Lev-Ram, Paul A. Steinbach, and Roger Y. Tsien. Mammalian Expression of Infrared Fluorescent Proteins Engineered from a Bacterial Phytochrome. *Science*, 324(5928):804–807, May 2009.

[8] Hiroshi Morise, Osamu Shimomura, Frank H Johnson, and John Winant. Intermolecular energy transfer in the bioluminescent system of aequorea. *Biochemistry*, 13(12):2656–2662, 1974.

[9] Yu A Labas, NG Gurskaya, Yu G Yanushevich, AF Fradkov, KA Lukyanov, SA Lukyanov, and MV Matz. Diversity and evolution of the green fluorescent protein family. *Proceedings of the National Academy of Sciences*, 99(7):4256–4261, 2002.

[10] Marvin Minsky. Microscopy Apparatus, December 1961. U.S. Classification: 356/432; 250/215; 348/79; 359/389.

[11] Jan Huisken, Jim Swoger, Filippo Del Bene, Joachim Wittbrodt, and Ernst H. K. Stelzer. Optical Sectioning Deep Inside Live Embryos by Selective Plane Illumination Microscopy. *Science*, 305(5686):1007–1009, August 2004.

[12] Winfried Denk, James H Strickler, Watt W Webb, et al. Two-photon laser scanning fluorescence microscopy. *Science*, 248(4951):73–76, 1990.

[13] Stella M Hurtley and Laura Helmuth. The future looks bright... *Science*, 300(5616):75–75, 2003.

[14] George Gabriel Stokes. On the change of refrangibility of light. *Philosophical Transactions of the Royal Society of London*, 142:463–562, 1852.

[15] Nathan C Shaner, Paul A Steinbach, and Roger Y Tsien. A guide to choosing fluorescent proteins. *Nature methods*, 2(12):905–909, 2005.

[16] Aleksander Jabłoński. Über den mechanismus der photolumineszenz von farbstoffphosphoren. *Zeitschrift für Physik*, 94(1-2):38–46, 1935.

[17] Richard P Haugland. *The handbook: a guide to fluorescent probes and labeling technologies*. Molecular probes, 2005.

[18] JOHN BOULTON. William henry perkin. *Journal of the Society of Dyers and Colourists*, 73(3):81–84, 1957.

[19] P Gutman and P Ehrich. Über die wirkung des methyleneblau bei malaria, berliner klin. *Wochenschr*, 28:953–956, 1891.

[20] James C Alwine, David J Kemp, and George R Stark. Method for detection of specific rnas in agarose gels by transfer to diazobenzyloxymethyl-paper and hybridization with dna probes. *Proceedings of the National Academy of Sciences*, 74(12):5350–5354, 1977.

[21] *Ueber eine neue Klasse von Farbstoffen*. Berichte der Deutschen chemischen Gesellschaft zu Berlin, 1871.

[22] Adolf Baeyer. Zur geschichte des eosins. *Berichte der deutschen chemischen Gesellschaft*, 8(1):146–148, 1875.

[23] Ben NG Giepmans, Stephen R Adams, Mark H Ellisman, and Roger Y Tsien. The fluorescent toolbox for assessing protein location and function. *science*, 312(5771):217–224, 2006.

[24] JW Uhr. The 1984 nobel prize in medicine. *Science*, 226(4678):1025–1028, 1984.

[25] Osamu Shimomura, Frank H Johnson, and Yo Saiga. Extraction, purification and properties of aequorin, a bioluminescent protein from the luminous hydromedusan, aequorea. *Journal of cellular and comparative physiology*, 59(3):223–239, 1962.

[26] Roger Heim and Roger Y Tsien. Engineering green fluorescent protein for improved brightness, longer wavelengths and fluorescence resonance energy transfer. *Current biology*, 6(2):178–182, 1996.

[27] Roger Heim, Douglas C Prasher, and Roger Y Tsien. Wavelength mutations and posttranslational autoxidation of green fluorescent protein. *Proceedings of the National Academy of Sciences*, 91(26):12501–12504, 1994.

[28] Brendan P Cormack, Raphael H Valdivia, and Stanley Falkow. Facs-optimized mutants of the green fluorescent protein (gfp). *Gene*, 173(1):33–38, 1996.

[29] Robert F Service. Nobel prize in chemistry. three scientists bask in prize's fluorescent glow. *Science (New York, NY)*, 322(5900):361, 2008.

[30] Nathan C Shaner, Robert E Campbell, Paul A Steinbach, Ben NG Giepmans, Amy E Palmer, and Roger Y Tsien. Improved monomeric red, orange and yellow fluorescent proteins derived from discosoma sp. red fluorescent protein. *Nature biotechnology*, 22(12):1567–1572, 2004.

[31] Daria M. Shcherbakova and Vladislav V. Verkhusha. Near-infrared fluorescent proteins for multicolor in vivo imaging. *Nature Methods*, advance online publication, June 2013.

[32] Atsushi Miyawaki, Daria M Shcherbakova, and Vladislav V Verkhusha. Red fluorescent proteins: chromophore formation and cellular applications. *Current opinion in structural biology*, 22(5):679–688, 2012.

[33] Chroma spectra viewer. `https://www.chroma.com/spectra-viewer?fluorochromes=10392,10424`, 2016.

[34] Grigory S. Filonov, Kiryl D. Piatkevich, Li-Min Ting, Jinghang Zhang, Kami Kim, and Vladislav V. Verkhusha. Bright and stable near-infrared fluorescent protein for in vivo imaging. *Nature Biotechnology*, 29(8):757–761, August 2011.

[35] Emil Wolf Max Born. *Principles of optics: electromagnetic theory of propagation, interference and diffraction of light*. Cambridge University Press, 7th expanded ed edition, 2005.

[36] CJR Sheppard and HJ Matthews. Imaging in high-aperture optical systems. *JOSA A*, 4(8):1354–1360, 1987.

[37] Lord Rayleigh. Wave theory of light. *Scientific Papers by John William Strutt, Baron Rayleigh*, 3:47–189, 1902.

[38] S Grill and EHK Stelzer. Method to calculate lateral and axial gain factors of optical setups with a large solid angle. *JOSA A*, 16(11):2658–2665, 1999.

[39] Ernst HK Stelzer. Contrast, resolution, pixelation, dynamic range and signal-to-noise ratio: fundamental limits to resolution in fluorescence light microscopy. *Journal of Microscopy*, 189(1):15–24, 1998.

[40] José-Angel Conchello and Jeff W Lichtman. Optical sectioning microscopy. *Nature methods*, 2(12):920–931, 2005.

[41] JB Pawley and Barry R Masters. Handbook of biological confocal microscopy. *Optical Engineering*, 35(9):2765–2766, 1996.

[42] Uros Krzic. Multiple-view microscopy with light-sheet based fluorescence microscope, 2009.

[43] Henry Siedentopf and Richard Zsigmondy. Uber sichtbarmachung und größenbestimmung ultramikoskopischer teilchen, mit besonderer anwendung auf goldrubingläser. *Annalen der Physik*, 315(1):1–39, 1902.

[44] Catherine Louis and Olivier Pluchery. *Gold nanoparticles for physics, chemistry and biology*. World Scientific, 2012.

[45] AH Voie, DH Burns, and FA Spelman. Orthogonal-plane fluorescence optical sectioning: Three-dimensional imaging of macroscopic biological specimens. *Journal of microscopy*, 170(3):229–236, 1993.

[46] Arne H Voie and Francis A Spelman. Three-dimensional reconstruction of the cochlea from two-dimensional images of optical sections. *Computerized medical imaging and graphics*, 19(5):377–384, 1995.

[47] Jan Huisken and Didier YR Stainier. Selective plane illumination microscopy techniques in developmental biology. *Development*, 136(12):1963–1975, 2009.

[48] Gustavo de Medeiros, Bálint Balázs, and Lars Hufnagel. Light-sheet imaging of mammalian development. In *Seminars in cell & developmental biology*, volume 55, pages 148–155. Elsevier, 2016.

[49] Philipp J Keller, Francesco Pampaloni, Gianluca Lattanzi, and Ernst HK Stelzer. Three-dimensional microtubule behavior in xenopus egg extracts reveals four dynamic states and state-dependent elastic properties. *Biophysical journal*, 95(3):1474–1486, 2008.

[50] Philipp J Keller. In vivo imaging of zebrafish embryogenesis. *Methods*, 62(3):268–278, 2013.

[51] Philipp J Keller, Annette D Schmidt, Joachim Wittbrodt, and Ernst HK Stelzer. Reconstruction of zebrafish early embryonic development by scanned light sheet microscopy. *science*, 322(5904):1065–1069, 2008.

[52] Paul J Scherz, Jan Huisken, Pankaj Sahai-Hernandez, and Didier YR Stainier. High-speed imaging of developing heart valves reveals interplay of morphogenesis and function. *Development*, 135(6):1179–1187, 2008.

[53] Benjamin Schmid, Gopi Shah, Nico Scherf, Michael Weber, Konstantin Thierbach, Citlali PÃĺrez Campos, Ingo Roeder, Pia Aanstad, and Jan Huisken. High-speed panoramic light-sheet microscopy reveals global endodermal cell dynamics. *Nature Communications*, 4, July 2013.

[54] Misha B Ahrens, Michael B Orger, Drew N Robson, Jennifer M Li, and Philipp J Keller. Whole-brain functional imaging at cellular resolution using light-sheet microscopy. *Nature methods*, 10(5):413–420, 2013.

[55] Raju Tomer, Khaled Khairy, Fernando Amat, and Philipp J. Keller. Quantitative high-speed imaging of entire developing embryos with simultaneous multiview light-sheet microscopy. *Nature Methods*, 9(7):755–763, July 2012.

[56] Petr Strnad, Stefan Gunther, Judith Reichmann, Uros Krzic, Balint Balazs, Gustavo de Medeiros, Nils Norlin, Takashi Hiiragi, Lars Hufnagel, and Jan Ellenberg. Inverted light-sheet microscope for imaging mouse pre-implantation development. *Nature methods*, 13(2):139–142, 2016.

[57] Nina Jährling, Klaus Becker, and Hans-Ulrich Dodt. 3d-reconstruction of blood vessels by ultramicroscopy. *Organogenesis*, 5(4):227–230, 2009.

[58] Klaus Becker, Nina Jährling, ER Kramer, Frank Schnorrer, and H-U Dodt. Ultramicroscopy: 3d reconstruction of large microscopical specimens. *Journal of biophotonics*, 1(1):36–42, 2008.

[59] Jérémie Capoulade, Malte Wachsmuth, Lars Hufnagel, and Michael Knop. Quantitative fluorescence imaging of protein diffusion and interaction in living cells. *Nature biotechnology*, 29(9):835–839, 2011.

[60] Yicong Wu, Alireza Ghitani, Ryan Christensen, Anthony Santella, Zhuo Du, Gary Rondeau, Zhirong Bao, Daniel Colón-Ramos, and Hari Shroff. Inverted selective plane illumination microscopy (ispim) enables coupled cell identity lineaging and neurodevelopmental imaging in caenorhabditis elegans. *Proceedings of the National Academy of Sciences*, 108(43):17708–17713, 2011.

[61] Patrick Hoyer, Gustavo de Medeiros, Bálint Balázs, Nils Norlin, Christina Besir, Janina Hanne, Hans-Georg Kräusslich, Johann Engelhardt, Steffen J Sahl, Stefan W Hell, et al. Breaking the diffraction limit of light-sheet fluorescence microscopy by resolft. *Proceedings of the National Academy of Sciences*, 113(13):3442–3446, 2016.

[62] Bi-Chang Chen, Wesley R Legant, Kai Wang, Lin Shao, Daniel E Milkie, Michael W Davidson, Chris Janetopoulos, Xufeng S Wu, John A Hammer, Zhe Liu, et al. Lattice light-sheet microscopy: Imaging molecules to embryos at high spatiotemporal resolution. *Science*, 346(6208):1257998, 2014.

[63] Jan Huisken and Didier Y. R. Stainier. Even fluorescence excitation by multidirectional selective plane illumination microscopy (mSPIM). *Optics Letters*, 32(17):2608–2610, September 2007.

[64] Peter G. Pitrone, Johannes Schindelin, Luke Stuyvenberg, Stephan Preibisch, Michael Weber, Kevin W. Eliceiri, Jan Huisken, and Pavel Tomancak. OpenSPIM: an open-access light-sheet microscopy platform. *Nature Methods*, 10(7):598–599, July 2013.

[65] Raghav K Chhetri, Fernando Amat, Yinan Wan, Burkhard Höckendorf, William C Lemon, and Philipp J Keller. Whole-animal functional and developmental imaging with isotropic spatial resolution. *Nature methods*, 2015.

[66] K Greger, J Swoger, and EHK Stelzer. Basic building units and properties of a fluorescence single plane illumination microscope. *Review of Scientific Instruments*, 78(2):023705, 2007.

[67] Philipp J. Keller, Annette D. Schmidt, Anthony Santella, Khaled Khairy, Zhirong Bao, Joachim Wittbrodt, and Ernst H. K. Stelzer. Fast, high-contrast imaging of animal development with scanned light sheet-based structured-illumination microscopy. *Nature Methods*, 7(8):637–642, August 2010.

[68] Kevin M Dean, Philippe Roudot, Erik S Welf, Gaudenz Danuser, and Reto Fiolka. Deconvolution-free subcellular imaging with axially swept light sheet microscopy. *Biophysical journal*, 108(12):2807–2815, 2015.

[69] Thomas A Planchon, Liang Gao, Daniel E Milkie, Michael W Davidson, James A Galbraith, Catherine G Galbraith, and Eric Betzig. Rapid three-dimensional isotropic imaging of living cells using bessel beam plane illumination. *Nature methods*, 8(5):417–423, 2011.

[70] Tom Vettenburg, Heather IC Dalgarno, Jonathan Nylk, Clara Coll-Lladó, David EK Ferrier, Tomáš Čižmár, Frank J Gunn-Moore, and Kishan Dholakia. Light-sheet microscopy using an airy beam. *Nature methods*, 11(5):541–544, 2014.

[71] Florian O. Fahrbach and Alexander Rohrbach. Propagation stability of self-reconstructing Bessel beams enables contrast-enhanced imaging in thick media. *Nature Communications*, 3:632, January 2012.

[72] Florian O. Fahrbach, Vasily Gurchenkov, Kevin Alessandri, Pierre Nassoy, and Alexander Rohrbach. Light-sheet microscopy in thick media using scanned Bessel beams and two-photon fluorescence excitation. *Optics Express*, 21(11):13824–13839, June 2013.

[73] Francesca Cella Zanacchi, Zeno Lavagnino, Mario Faretta, Laura Furia, and Alberto Diaspro. Light-sheet confined super-resolution using two-photon photoactivation. *PloS one*, 8(7):e67667, 2013.

[74] Thai V. Truong, Willy Supatto, David S. Koos, John M. Choi, and Scott E. Fraser. Deep and fast live imaging with two-photon scanned light-sheet microscopy. *Nature Methods*, 8(9):757–760, September 2011.

[75] Pierre Mahou, Julien Vermot, Emmanuel Beaurepaire, and Willy Supatto. Multicolor two-photon light-sheet microscopy. *Nature methods*, 11(6):600–601, 2014.

[76] L. Silvestri, A. Bria, L. Sacconi, G. Iannello, and F. S. Pavone. Confocal light sheet microscopy: micron-scale neuroanatomy of the entire mouse brain. *Optics Express*, 20(18):20582–20598, August 2012.

[77] Eugen Baumgart and Ulrich Kubitscheck. Scanned light sheet microscopy with confocal slit detection. *Optics Express*, 20(19):21805–21814, September 2012.

[78] Gustavo de Medeiros, Nils Norlin, Stefan Gunther, Marvin Albert, Laura Panavaite, Ulla-Maj Fiuza, Francesca Peri, Takashi Hiiragi, Uros Krzic, and Lars Hufnagel. Confocal multiview light-sheet microscopy. *Nature Communications*, 6:8881, November 2015.

[79] Christoph J Engelbrecht and Ernst H Stelzer. Resolution enhancement in a light-sheet-based microscope (spim). *Optics letters*, 31(10):1477–1479, 2006.

[80] Mike Friedrich, Qiang Gan, Vladimir Ermolayev, and Gregory S Harms. Sted-spim: stimulated emission depletion improves sheet illumination microscopy resolution. *Biophysical journal*, 100(8):L43–L45, 2011.

[81] Bahaa EA Saleh, Malvin Carl Teich, and Bahaa E Saleh. *Fundamentals of photonics*, volume 22. Wiley New York, 1991.

[82] Ashley J. Welch and Martin J.C. van Gemert. *Optical-Thermal Response of Laser-Irradiated Tissue*. Springer Netherlands, 2 edition, 2011.

[83] Peter J Verveer, Jim Swoger, Francesco Pampaloni, Klaus Greger, Marco Marcello, and Ernst HK Stelzer. High-resolution three-dimensional imaging of large specimens with light sheet–based microscopy. *Nature methods*, 4(4):311–313, 2007.

[84] Stephan Preibisch, Stephan Saalfeld, Johannes Schindelin, and Pavel Tomancak. Software for bead-based registration of selective plane illumination microscopy data. *Nature Methods*, 7(6):418–419, 2010.

[85] Johannes Schindelin, Ignacio Arganda-Carreras, Erwin Frise, Verena Kaynig, Mark Longair, Tobias Pietzsch, Stephan Preibisch, Curtis Rueden, Stephan Saalfeld, Benjamin Schmid, et al. Fiji: an open-source platform for biological-image analysis. *Nature methods*, 9(7):676–682, 2012.

[86] Eric F Pettersen, Thomas D Goddard, Conrad C Huang, Gregory S Couch, Daniel M Greenblatt, Elaine C Meng, and Thomas E Ferrin. Ucsf

chimeraâĂŤa visualization system for exploratory research and analysis. *Journal of computational chemistry*, 25(13):1605–1612, 2004.

[87] Gustavo de Medeiros, Stefan Gunther, Manuela Beck, Giorgia Guglielmi, and Joran Deschamps. Life in Perspective. `http://arts.embl.de`, 2016. [Online; accessed 19-July-2016].

[88] Vasilis Ntziachristos. Going deeper than microscopy: the optical imaging frontier in biology. *Nature Methods*, 7(8):603–614, August 2010.

[89] Steven L Jacques. Optical properties of biological tissues: a review. *Physics in medicine and biology*, 58(11):R37, 2013.

[90] Alfred Vogel and Vasan Venugopalan. Mechanisms of pulsed laser ablation of biological tissues. *Chemical reviews*, 103(2):577–644, 2003.

[91] Ralph Weissleder and Vasilis Ntziachristos. Shedding light onto live molecular targets. *Nature Medicine*, 9(1):123–128, January 2003.

[92] Markolf H Niemz. *Laser-tissue interactions: fundamentals and applications*. Springer Science & Business Media, 2013.

[93] Lihong V Wang and Hsin-i Wu. *Biomedical optics: principles and imaging*. John Wiley & Sons, 2012.

[94] Rudolf Steiner. Laser-tissue interactions. In *Laser and IPL Technology in Dermatology and Aesthetic Medicine*, pages 23–36. Springer, 2011.

[95] Jean-Luc Boulnois. Photophysical processes in recent medical laser developments: a review. *Lasers in Medical Science*, 1(1):47–66, 1986.

[96] Akira Ishimaru. *Wave Propagation and Scattering in Random Media.* Academic Press, 1978.

[97] Fritjof Helmchen and Winfried Denk. Deep tissue two-photon microscopy. *Nat Meth*, 2(12):932–940, 2005.

[98] A. N. Bashkatov, E. A. Genina, V. I. Kochubey, and V. V. Tuchin. Optical properties of human skin, subcutaneous and mucous tissues in the wavelength range from 400 to 2000 nm. *Journal of Physics D: Applied Physics*, 38(15):2543, 2005.

[99] Zeno Lavagnino, Francesca Cella Zanacchi, Emiliano Ronzitti, and Alberto Diaspro. Two-photon excitation selective plane illumination microscopy (2pe-spim) of highly scattering samples: characterization and application. *Optics express*, 21(5):5998–6008, 2013.

[100] Ludovico Silvestri, Anna Letizia Allegra Mascaro, Irene Costantini, Leonardo Sacconi, and Francesco Saverio Pavone. Correlative two-photon and light sheet microscopy. *Methods*, 66(2):268–272, 2014.

[101] Le Cong, F Ann Ran, David Cox, Shuailiang Lin, Robert Barretto, Naomi Habib, Patrick D Hsu, Xuebing Wu, Wenyan Jiang, Luciano A Marraffini, et al. Multiplex genome engineering using crispr/cas systems. *Science*, 339(6121):819–823, 2013.

[102] Helena M Thorpe and Margaret CM Smith. In vitro site-specific integration of bacteriophage dna catalyzed by a recombinase of the resolvase/invertase family. *Proceedings of the National Academy of Sciences*, 95(10):5505–5510, 1998.

[103] Karl Deisseroth. Optogenetics. *Nature methods*, 8(1):26–29, 2011.

[104] Giorgia Guglielmi, Joseph D Barry, Wolfgang Huber, and Stefano De Renzis. An optogenetic method to modulate cell contractility during tissue morphogenesis. *Developmental cell*, 35(5):646–660, 2015.

[105] R Srinivasan and WJ Leigh. Ablative photodecomposition: action of far-ultraviolet (193 nm) laser radiation on poly (ethylene terephthalate) films. *Journal of the American chemical Society*, 104(24):6784–6785, 1982.

[106] A Vogel, J Noack, G Hüttman, and G Paltauf. Mechanisms of femtosecond laser nanosurgery of cells and tissues. *Applied Physics B*, 81(8):1015–1047, 2005.

[107] CA Sacchi. Laser-induced electric breakdown in water. *JOSA B*, 8(2):337–345, 1991.

[108] L. D. Landau and E. M. Lifshitz. *Quantum Mechanics. Non-Relativistic Theory*. Pergamon Press, 3 edition, 1977.

[109] Samuel H Chung and Eric Mazur. Femtosecond laser ablation of neurons in c. elegans for behavioral studies. *Applied Physics A*, 96(2):335–341, 2009.

[110] Matteo Rauzi and Pierre-François Lenne. Chapter 4 cortical forces in cell shape changes and tissue morphogenesis. *Current topics in developmental biology*, 95:93, 2011.

[111] Stephan Preibisch, Fernando Amat, Evangelia Stamataki, Mihail Sarov, Robert H. Singer, Eugene Myers, and Pavel Tomancak. Efficient

Bayesian-based multiview deconvolution. *Nature Methods*, 11(6):645–648, June 2014.

[112] Jim Swoger, Peter Verveer, Klaus Greger, Jan Huisken, and Ernst HK Stelzer. Multi-view image fusion improves resolution in three-dimensional microscopy. *Optics express*, 15(13):8029–8042, 2007.

[113] Benjamin Schmid and Jan Huisken. Real-time multi-view deconvolution. *Bioinformatics*, page btv387, 2015.

[114] E. Mei, P.a. Fomitchov, R. Graves, and M. Campion. A line scanning confocal fluorescent microscope using a CMOS rolling shutter as an adjustable aperture. *Journal of Microscopy*, 247(3):269–276, 2012.

[115] Raju Tomer, Li Ye, Brian Hsueh, and Karl Deisseroth. Advanced CLARITY for rapid and high-resolution imaging of intact tissues. *Nature Protocols*, 9(7):1682–1697, July 2014.

[116] Eli Peli. Contrast in complex images. *JOSA A*, 7(10):2032–2040, October 1990.

[117] M. Temerinac-Ott, O. Ronneberger, R. Nitschke, W. Driever, and H. Burkhardt. Spatially-variant Lucy-Richardson deconvolution for multiview fusion of microscopical 3d images. In *2011 IEEE International Symposium on Biomedical Imaging: From Nano to Macro*, pages 899 –904, April 2011.

[118] Takaya Abe, Hiroshi Kiyonari, Go Shioi, Ken-Ichi Inoue, Kazuki Nakao, Shinichi Aizawa, and Toshihiko Fujimori. Establishment of conditional reporter mouse lines at ROSA26 locus for live cell imaging. *Genesis (New York, N.Y.: 2000)*, 49(7):579–590, July 2011.

[119] Mandar Deepak Muzumdar, Bosiljka Tasic, Kazunari Miyamichi, Ling Li, and Liqun Luo. A global double-fluorescent Cre reporter mouse. *Genesis (New York, N.Y.: 2000)*, 45(9):593–605, September 2007.

[120] Christian Sardet, Alex McDougall, Hitoyoshi Yasuo, Janet Chenevert, Gérard Pruliere, Rémi Dumollard, Clare Hudson, Celine Hebras, Ngan Le Nguyen, and Alexandre Paix. Embryological methods in ascidians: the villefranche-sur-mer protocols. *Vertebrate Embryogenesis: Embryological, Cellular, and Genetic Methods*, pages 365–400, 2011.

[121] Werner Spalteholz et al. *Über das Durchsichtigmachen von menschlichen und tierischen Präparaten und seine theoretischen Bedingungen, nebst Anhang*. S. Hirzel, 1914.

[122] JOSEPH A Dent, ANDREW G Polson, and MICHAEL W Klymkowsky. A whole-mount immunocytochemical analysis of the expression of the intermediate filament protein vimentin in xenopus. *Development*, 105(1):61–74, 1989.

[123] Hans-Ulrich Dodt, Ulrich Leischner, Anja Schierloh, Nina Jährling, Christoph Peter Mauch, Katrin Deininger, Jan Michael Deussing, Matthias Eder, Walter Zieglgänsberger, and Klaus Becker. Ultramicroscopy: three-dimensional visualization of neuronal networks in the whole mouse brain. *Nature methods*, 4(4):331–336, 2007.

[124] Kwanghun Chung, Jenelle Wallace, Sung-Yon Kim, Sandhiya Kalyanasundaram, Aaron S Andalman, Thomas J Davidson, Julie J Mirzabekov, Kelly A Zalocusky, Joanna Mattis, Aleksandra K Denisin, et al. Structural and molecular interrogation of intact biological systems. *Nature*, 497(7449):332–337, 2013.

[125] Etsuo A Susaki, Kazuki Tainaka, Dimitri Perrin, Fumiaki Kishino, Takehiro Tawara, Tomonobu M Watanabe, Chihiro Yokoyama, Hirotaka Onoe, Megumi Eguchi, Shun Yamaguchi, et al. Whole-brain imaging with single-cell resolution using chemical cocktails and computational analysis. *Cell*, 157(3):726–739, 2014.

[126] Meng-Tsen Ke, Satoshi Fujimoto, and Takeshi Imai. Seedb: a simple and morphology-preserving optical clearing agent for neuronal circuit reconstruction. *Nature neuroscience*, 16(8):1154–1161, 2013.

[127] Ali Ertürk, Klaus Becker, Nina Jährling, Christoph P Mauch, Caroline D Hojer, Jackson G Egen, Farida Hellal, Frank Bradke, Morgan Sheng, and Hans-Ulrich Dodt. Three-dimensional imaging of solvent-cleared organs using 3disco. *Nature protocols*, 7(11):1983–1995, 2012.

[128] Nicholas G Horton, Ke Wang, Demirhan Kobat, Catharine G Clark, Frank W Wise, Chris B Schaffer, and Chris Xu. In vivo three-photon microscopy of subcortical structures within an intact mouse brain. *Nature photonics*, 7(3):205–209, 2013.

[129] Ralph Weissleder. A clearer vision for in vivo imaging. *Nature biotechnology*, 19(4):316–317, 2001.

[130] Glória RC Braz, Leonardo Abreu, Hatisaburo Masuda, and Pedro L Oliveira. Heme biosynthesis and oogenesis in the blood-sucking bug, rhodnius prolixus. *Insect biochemistry and molecular biology*, 31(4):359–364, 2001.

[131] Eric Giraud, Joël Fardoux, Nicolas Fourrier, Laure Hannibal, Bernard Genty, Pierre Bouyer, Bernard Dreyfus, and André Verméglio. Bacteriophytochrome controls photosystem synthesis in anoxygenic bacteria. *Nature*, 417(6885):202–205, 2002.

[132] CH Gray, A Lichtarowicz-Kulczycka, DC Nicholson, and Z Petryka. 440. the chemistry of the bile pigments. part ii. the preparation and spectral properties of biliverdin. *Journal of the Chemical Society (Resumed)*, pages 2264–2268, 1961.

[133] Ping Liu, Thankiah Sudhaharan, Rosita ML Koh, Ling C Hwang, Sohail Ahmed, Ichiro N Maruyama, and Thorsten Wohland. Investigation of the dimerization of proteins from the epidermal growth factor receptor family by single wavelength fluorescence cross-correlation spectroscopy. *Biophysical journal*, 93(2):684–698, 2007.

[134] Dan Yu, William Clay Gustafson, Chun Han, CÃľline Lafaye, Marjolaine Noirclerc-Savoye, Woo-Ping Ge, Desiree A. Thayer, Hai Huang, Thomas B. Kornberg, Antoine Royant, Lily Yeh Jan, Yuh Nung Jan, William A. Weiss, and Xiaokun Shu. An improved monomeric infrared fluorescent protein for neuronal and tumour brain imaging. *Nature Communications*, 5, 2014.

[135] Dan Yu, Michelle A. Baird, John R. Allen, Elizabeth S. Howe, Matthew P. Klassen, Anna Reade, Kalpana Makhijani, Yuanquan Song, Songmei Liu, Zehra Murthy, Shao-Qing Zhang, Orion D. Weiner, Thomas B. Kornberg, Yuh-Nung Jan, Michael W. Davidson, and Xiaokun Shu. A naturally monomeric infrared fluorescent protein for protein labeling in vivo. *Nature Methods*, 12(8):763–765, August 2015.

[136] Yusuke Miyanari, Céline Ziegler-Birling, and Maria-Elena Torres-Padilla. Live visualization of chromatin dynamics with fluorescent tales. *Nature structural & molecular biology*, 20(11):1321–1324, 2013.

[137] Johannes Bischof, Robert K Maeda, Monika Hediger, François Karch, and Konrad Basler. An optimized transgenesis system for drosophila using germ-line-specific φc31 integrases. *Proceedings of the National Academy of Sciences*, 104(9):3312–3317, 2007.

[138] Koen JT Venken, Yuchun He, Roger A Hoskins, and Hugo J Bellen. P [acman]: a bac transgenic platform for targeted insertion of large dna fragments in d. melanogaster. *Science*, 314(5806):1747–1751, 2006.

[139] Allan C Spradling and Gerald M Rubin. Transposition of cloned p elements into drosophila germ line chromosomes. *Science*, 218(4570):341–347, 1982.

[140] William R Engels. P elements in drosophila. In *Transposable elements*, pages 103–123. Springer, 1996.

[141] Mary Bownes. A photographic study of development in the living embryo of drosophila melanogaster. *Development*, 33(3):789–801, 1975.

[142] José A Campos-Ortega and Volker Hartenstein. *The embryonic development of Drosophila melanogaster*. Springer Science & Business Media, 2013.

[143] Steven G Kuntz and Michael B Eisen. Drosophila embryogenesis scales uniformly across temperature in developmentally diverse species. *PLoS Genet*, 10(4):e1004293, 2014.

[144] Lihua Cui, Yasuhide Yoshioka, Osamu Suyari, Yusuke Kohno, Xuhong Zhang, Yasushi Adachi, Susumu Ikehara, Tadashi Yoshida, Masamitsu Yamaguchi, and Shigeru Taketani. Relevant expression of Drosophila heme oxygenase is necessary for the normal development of insect tissues. *Biochemical and Biophysical Research Communications*, 377(4):1156–1161, December 2008.

[145] Hiroyuki Ida, Osamu Suyari, Mai Shimamura, Tran Tien Tai, Masamitsu Yamaguchi, and Shigeru Taketani. Genetic link between heme oxygenase and the signaling pathway of dna damage in drosophila melanogaster. *The Tohoku journal of experimental medicine*, 231(2):117–125, 2013.

[146] Goro Kikuchi, Tadashi Yoshida, and Masato Noguchi. Heme oxygenase and heme degradation. *Biochemical and biophysical research communications*, 338(1):558–567, 2005.

[147] Xuhong Zhang, Michihiko Sato, Masanao Sasahara, Catharina T Migita, and Tadashi Yoshida. Unique features of recombinant heme oxygenase of drosophila melanogaster compared with those of other heme oxygenases studied. *European Journal of Biochemistry*, 271(9):1713–1724, 2004.

[148] Christoph J. Engelbrecht, Klaus Greger, Emmanuel G. Reynaud, UroÅą KrÅ"ic, Julien Colombelli, and Ernst H. K. Stelzer. Three-dimensional laser microsurgery in light-sheet based microscopy (SPIM). *Optics Express*, 15(10):6420, May 2007.

[149] Kristin Sherrard, François Robin, Patrick Lemaire, and Edwin Munro. Sequential activation of apical and basolateral contractility drives ascidian endoderm invagination. *Current Biology*, 20(17):1499–1510, 2010.

[150] Lawrence S Bass and Michael R Treat. Laser tissue welding: A comprehensive review of current and future. *Lasers in surgery and medicine*, 17(4):315–349, 1995.

[151] Willy Supatto, Delphine Débarre, Bruno Moulia, Eric Brouzés, Jean-Louis Martin, Emmanuel Farge, and Emmanuel Beaurepaire. In vivo modulation of morphogenetic movements in drosophila embryos with femtosecond laser pulses. *Proceedings of the National Academy of Sciences of the United States of America*, 102(4):1047–1052, 2005.

[152] Matteo Rauzi, Uros Krzic, Timothy E. Saunders, Matej Krajnc, PrimoÅ" Ziherl, Lars Hufnagel, and Maria Leptin. Embryo-scale tissue mechanics during Drosophila gastrulation movements. *Nature Communications*, 6:8677, October 2015.

[153] Claudio Collinet, Matteo Rauzi, Pierre-François Lenne, and Thomas Lecuit. Local and tissue-scale forces drive oriented junction growth during tissue extension. *Nature cell biology*, 2015.

[154] Zehra Ali-Murthy, Susan E Lott, Michael B Eisen, and Thomas B Kornberg. An essential role for zygotic expression in the pre-cellular drosophila embryo. *PLoS Genet*, 9(4):e1003428, 2013.

[155] Zehra Ali-Murthy and Thomas B Kornberg. Bicoid gradient formation and function in the drosophila pre-syncytial blastoderm. *eLife*, 5:e13222, 2016.

[156] Shawn C Little, Gašper Tkačik, Thomas B Kneeland, Eric F Wieschaus, and Thomas Gregor. The formation of the bicoid morphogen gradient requires protein movement from anteriorly localized mrna. *PLoS Biol*, 9(3):e1000596, 2011.

[157] ED Schejter and E Wieschaus. Functional elements of the cytoskeleton in the early drosophila embryo. *Annual review of cell biology*, 9(1):67–99, 1993.

[158] William Sullivan and William E Theurkauf. The cytoskeleton and morphogenesis of the early drosophila embryo. *Current opinion in cell biology*, 7(1):18–22, 1995.

[159] Katerina R Katsani, Roger E Karess, Nathalie Dostatni, and Valérie Doye. In vivo dynamics of drosophila nuclear envelope components. *Molecular biology of the cell*, 19(9):3652–3666, 2008.

[160] Alessandra Maria Casano and Francesca Peri. Microglia: multitasking specialists of the brain. *Developmental cell*, 32(4):469–477, 2015.

[161] Dirk Sieger, Christian Moritz, Thomas Ziegenhals, Sergey Prykhozhij, and Francesca Peri. Long-range ca 2+ waves transmit brain-damage signals to microglia. *Developmental cell*, 22(6):1138–1148, 2012.

[162] Allison F Rosenberg, Marc A Wolman, Clara Franzini-Armstrong, and Michael Granato. In vivo nerve–macrophage interactions following peripheral nerve injury. *The Journal of Neuroscience*, 32(11):3898–3909, 2012.

[163] Allison F Rosenberg, Jesse Isaacman-Beck, Clara Franzini-Armstrong, and Michael Granato. Schwann cells and deleted in colorectal carcinoma direct regenerating motor axons towards their original path. *The Journal of Neuroscience*, 34(44):14668–14681, 2014.

[164] Yan Xiao, Adèle Faucherre, Laura Pola-Morell, John M Heddleston, Tsung-Li Liu, Teng-Leong Chew, Fuminori Sato, Atsuko Sehara-Fujisawa, Koichi Kawakami, and Hernán López-Schier. High-resolution live imaging reveals axon-glia interactions during peripheral nerve injury and repair in zebrafish. *Disease Models and Mechanisms*, 8(6):553–564, 2015.

Acknowledgements

The work presented in this thesis has been carried out in the group of Lars Hufnagel at the European molecular Biology Laboratory (EMBL) in Heidelberg, Germany. I am grateful to Lars Hufnagel for giving me a chance to work in the world of microscopy, always providing new exciting ideas and supporting me during my time in the lab, when necessary.

Many thanks also go to Uros Krzic, who introduced me to the world of SPIM, as well as to Tatjana Schneidt, who presented me to the world of cells and flies and... ...m u t a n t s. Matteo Rauzi, thank you for introducing me to the world of photoablation processes and the amazing things you can do with them.

I am very grateful to have spent these years along the company of such great people: Nils Norlin, for the inumerous SPIM adventures, mysteries, along with some memorable 2am Kicker and the much good music; Stefan GÃijnther, for sharing all the swearing in the lab and allowing me to participate in the creation of exciting new visualization approaches of scientific data, putting life in perspective (along with Manuela Beck, Joran Deschamps and Giorgia Giuglielmi. Also thank you for getting me nice small and fat embryos for ablation experiments.); Bálint Bálazs, for sharing all those precious soldering and 9gagging (ops) experiences, among all the very helpful discussion in the world of programming; Sebastian Streichan and Marvin Albert, for the memorable organization of Oktoberfest and all the fun that came with it; Ulla-Maj Fiuza, for all the nice discussions on fly genetics, ascidian development, and showing me your passion about biology and science; Patrick Hoyer, for sharing the anxiety when his microscope software presented a bug, as well as for living with me the usual PhD ups and downs; Dimitri Kromm, for protecting us from harm with greased objectives; Aldona Nowicka and Christina Besir, for all the help with the biochemistry and fly caretaking; LucÃŋa Durrieu, for all the important advices which somehow I just couldn't fully realise at the time; Justus Fuesers, for all the musical ideas, and Christian Hoerner, for sharing nice stories about EMBL PhD life. Additionally, I would also like

to acknowledge Henry Werner, Helmut Schaar, Tim Hettinger and Leo Burger from the mechanical workshop for all the help in making the necessary mechanical parts for putting the optics together. In particular, I would like to thank Sascha BlÃďttel for all the serious and funny moments when designing new mechanical pieces, and sharing broken ligamental stories.

Special thanks go to Alba Alfonso Garcia, who inspired me to change research fields after my masters, and first showed me that such a place as EMBL actually existed.

From 2012 to now, I have met many people who have brightened my time at EMBL. Serge, Aastha, Deepika, George, Thibaut, Philippe, Joana, Alessandra, Konrad, Johanna, Natalia, Petr, Iana, Hernando, Vaso, Joran, Laura, Aleksandra, Doris, Leo, Andrea, Simone, Paul,Birgit, Markus... I am sure I am forgetting many names, but time is getting really short! You know who you are: my time at EMBL without you would definitely not have been the same.

Paola, Nik, Sean, Wieslaw, and Dan: we rocked!

For my last remaining minutes before printing this Thesis, I would like to thank my parents, Darlan Glasner de Medeiros and Maria Guilhermina Quintas de Medeiros and my sisters Paula and Carla for the all the love and support throughout all this time, I am trulu lucky to have you.

Last but certainly not least: Isabela and Oana, thank you for bringing light and color into my life.